

~~AD 301039~~

DTIC FILE COPY

AD

(4)

DTIC FILE COPY

CONTRACT REPORT BRL-CR-584

AD-A193 196

COMPUTATIONAL MODEL FOR
ARMOR PENETRATION
1ST ANNUAL REPORT

SRI INTERNATIONAL
333 RAVENSWOOD AVENUE
MENLO PARK, CA 94025

OCTOBER 1987

DTIC
SELECTE
MAR 14 1988
S H D

APPROVED FOR PUBLIC RELEASE; DISTRIBUTION UNLIMITED.

US ARMY BALLISTIC RESEARCH LABORATORY
ABERDEEN PROVING GROUND, MARYLAND

88 3 10 038

DESTRUCTION NOTICE

Destroy this report when it is no longer needed. DO NOT return it to the originator.

Additional copies of this report may be obtained from the National Technical Information Service, U.S. Department of Commerce, Springfield, VA 22161.

The findings of this report are not to be construed as an official Department of the Army position, unless so designated by other authorized documents.

The use of trade names or manufacturers' names in this report does not constitute indorsement of any commercial product.

REPORT DOCUMENTATION PAGE

Firm Approved
OMB No. 0704-0188
Exp. Date: Jun 30, 1986

1a. REPORT SECURITY CLASSIFICATION Unclassified		1b. RESTRICTIVE MARKINGS	
2a. SECURITY CLASSIFICATION AUTHORITY		3. DISTRIBUTION/AVAILABILITY OF REPORT	
2b. DECLASSIFICATION/DOWNGRADING SCHEDULE			
4. PERFORMING ORGANIZATION REPORT NUMBER(S) FYU 7893		5. MONITORING ORGANIZATION REPORT NUMBER(S) BRL-CR-584	
6a. NAME OF PERFORMING ORGANIZATION SRI International	6b. OFFICE SYMBOL (if applicable)	7a. NAME OF MONITORING ORGANIZATION Ballistic Research Laboratory ATTN: SLCBR-TB	
6c. ADDRESS (City, State, and ZIP Code) 333 Fawnswood Avenue Menlo Park, CA 94025		7b. ADDRESS (City, State, and ZIP Code) Aberdeen Proving Ground, MD 21005-5066	
8a. NAME OF FUNDING/SPONSORING ORGANIZATION	8b. OFFICE SYMBOL (if applicable)	9. PROCUREMENT INSTRUMENT IDENTIFICATION NUMBER DAAK11-78-C-0115	
8c. ADDRESS (City, State, and ZIP Code)		10. SOURCE OF FUNDING NUMBERS	
		PROGRAM ELEMENT NO.	PROJECT NO.
		TASK NO.	WORK UNIT ACCESSION NO.
11. TITLE (Include Security Classification) COMPUTATIONAL MODEL FOR ARMOR PENETRATION, 1st Annual Report			
12. PERSONAL AUTHOR(S) D.K. CURTIS (SUPERVISOR), R. BIRBAER, R.D. CALIGNI, M. COWPERTHWILLE, D.C. ERLICH, L. SEAMAN and D.A. SHOCKEY			
13a. TYPE OF REPORT Contract Report	13b. TIME COVERED FROM Oct 78 TO Oct 79	14. DATE OF REPORT (Year, Month, Day)	15. PAGE COUNT
16. SUPPLEMENTARY NOTATION			
17. COSATI CODES		18. SUBJECT TERMS (Continue on reverse if necessary and identify by block number)	
FIELD	GROUP	SUB-GROUP	Computational Model, Depleted Uranium, Ductile Fracture, Fracture, Fragmentation, Microstructural Damage, Penetrator, Shear Band, Tank Armor, Tungsten
11	06		
10	04		
19. ABSTRACT (Continue on reverse if necessary and identify by block number) → Results are reported from the first year of a three-year joint BRL/AMRC/SRI program to develop a computational capability to predict the behind-the-armor fragment environment for spaced armor attacked by long rod penetrators. The materials chosen for study were depleted uranium- and tungsten-alloy penetrators, rolled homogeneous armor, and an electroslag-remelt-treated steel armor. Phenomenology experiments indicated that adiabatic shear banding is the dominant microstructural failure mode underlying target plugging and fragmentation as well as penetrator nose erosion. A previously developed computational model for shear banding was improved, calibrated with dynamic material property experimental data, and applied to preliminary computational simulations of normal impact experiments. In addition, an approximate formula was developed to estimate the critical strain for onset of shear banding. Promising agreement between these preliminary computations and experimental observations was obtained. Information was also obtained on tensile failure of rolled homogeneous armor by ductile void activity, and a method			
20. DISTRIBUTION/AVAILABILITY OF ABSTRACT <input checked="" type="checkbox"/> UNCLASSIFIED/UNLIMITED <input type="checkbox"/> SAME AS RPT. <input type="checkbox"/> DTIC USERS		21. ABSTRACT SECURITY CLASSIFICATION Unclassified	
22a. NAME OF RESPONSIBLE INDIVIDUAL Michael Scheidler		22b. TELEPHONE (Include Area Code) 301/278-6836	22c. OFFICE SYMBOL SLCBR-TB-W

19. ABSTRACT (con't)

for generating high strain rate plastic yield information was developed. Future work will extend this approach to oblique impacts, multiple plates, and, if the results of ongoing phenomenology experiments establish their importance, to other microstructural damage modes.



ACKNOWLEDGMENTS

The SRI portion of this joint BRL/AMTRC/SRI program has benefited greatly from discussions and technical support from Drs. Gerald Moss and John Mescall, the BRL and AMTRC project monitors, respectively, as well as from many other BRL and AMTRC personnel. The program has also benefited from the interest and encouragement shown by Dr. Richard Vitali of BRL and Dr. Edward Wright of AMTRC.

Excellent computational and experimental support at SRI was provided by Bonita Law, Robert Gates, Lee Hall, Dante Petro, and Margaret Menting.

Thanks are due to Dr. Michael Cowperthwaite for assistance in modelling the detonation process.



Accession For	
NTIS GRA&I	<input checked="" type="checkbox"/>
DTIC TAB	<input type="checkbox"/>
Unannounced	<input type="checkbox"/>
Justification _____	
By _____	
Distribution/	
Availability Codes	
Dist	Avail and/or Special
A-1	

CONTENTS

ACKNOWLEDGMENTS	iii
LIST OF ILLUSTRATIONS	vii
LIST OF TABLES	xi
I INTRODUCTION AND SUMMARY	1
II EXPERIMENTS	5
A. Material Selection, Procurement, and Metallurgical Analysis.	5
B. Phenomenology Experiments	18
C. Material Characterization Experiments	26
III ANALYSIS	41
A. Computational Model Adaptation	41
B. Generation and Testing of Shear Banding Model Parameters	49
C. Adaptation of HEMP Code for Use with NAG Material Models	66
D. Computational Simulations	68
IV CONCLUSIONS AND FUTURE PLANS	81
A. Materials Selection and Phenomenology Experiments.	82
B. Material Characterization Experiments	84
C. Computational Model Adaptation	85
D. Generation and Testing Model Parameters.	86
E. Adaptation of HEMP Code for Use with NAG Material Models	86
F. Computational Simulations.	86
REFERENCES.	87
APPENDICES.	91
A The SHEAR3 SUBROUTINE FOR ADIABATIC SHEAR BANDING.	91
B THRESHOLD INITIATION CRITERIA FOR ADIABATIC SHEAR BANDING.	121
DISTRIBUTION LIST	139

ILLUSTRATIONS

1.	True Stress-True Strain Curves for RHA Specimens Tested in the Three Principal Directions	10
2.	SEM of the Fracture Surface of Specimen R-1 (Rolling Direction) Showing the Conventional Cup-and-Cone Type of Fracture . . .	12
3.	Details of the Void Structure in the Center of the Fracture Surfaces of Specimens R-1 and L-2	13
4.	SEM of the Fracture Surface of Specimen S-2 (short transverse direction)	15
5.	Details of the Fracture Surface of Specimen S-2 (short transverse direction)	16
6.	Polished Cross Sections of Tensile Specimens in the Three Principal Orientations Comparing Relative Internal Void Activity in the Vicinity of the Neck	17
7.	Polished and Etched Cross Section through Center of RHA Target Impacted by a Blunt-Nosed 4340 Steel Projectile at 2150 ft/sec (655 m/sec)	19
8.	Impact Side of (a) and Polished and Etched Cross Section (b) through Center of RHA Target Impacted by Blunt-nosed 4340 Steel Projectile at 2330 ft/sec (710 m/sec)	20
9.	Blunt-Nosed 4340 Steel Projectile Within Plug on Rear Surface of Target Plate (a) and Etched Cross Section Through RHA Target and Plug Following Impact at 2600 ft/sec (792 m/sec) .	21
10.	Recovered Uranium-3/4 wt% Titanium After Perforation of Scaled Triple Armor	24
11.	Steel Target Plate No. 4 Impacted at an Oblique Angle by a Uranium-3/4 wt% Titanium Alloy Penetrator	25
12.	Equivalent Plastic Strain Determined from Measurements of RHA Specimen Tubes Recovered from CFC Experiments	26

13.	Two Views of Half the RHA Specimen Tube L4 Recovered from CFC Experiment	29
14.	Polished and Etched Section through RHA Specimen Tube L4, Showing Preponderance of Shear Banding Damage in Rolling Direction	31
15.	CFC Specimens Machined from RHA Slab, Showing Mode 1 Shear Bands in Planes Perpendicular to Rolling Plane	32
16.	Geometry and Nomenclature for Shear Bands in Contained-Fragmenting-Cylinder Experiments	33
17.	Schematic Diagram of Symmetric Taylor Test	36
18.	Framing Camera Records of Mushrooming Aluminum Rods in Symmetric Taylor Test	38
19.	Photographs of Recovered Aluminum Rod Showing that the Permanent Deformation Was Due Entirely to Homogeneous Plastic Flow	39
20.	Cross Section of Contained-Fragmenting-Cylinder Experiments .	51
21.	Shear Band Distribution for Shot 2 in 4340 Steel	52
22.	Measured Numbers of Shear Bands/cm ² Versus Plastic Strain Based on Wall Thickness Measurements for Six Contained-Fragmenting-Cylinder Experiments in 4340 Steel	53
23.	Size Parameter R ₁ from Measured Shear Band Size Distributions versus Plastic Strain based on Wall Thickness Measurements for Six Contained-Fragmenting-Cylinder Experiments in 4340 Steel	57
24.	Measured Damage Versus Plastic Strain based on Wall Thickness Measurements for Six Contained-Fragmenting-Cylinder Experiments in 4340 Steel	59
25.	Analytical and Computational Pressure-Volume Paths Followed in a Detonation Process in Low Density ($\rho = 1.2$ g/cc) PETN .	64
26.	Comparison of Analytical and Computational Pressure Histories in Low Density ($\rho = 1.2$ g/cc) PETN	65
27.	A Slide Line that Contains Zipped and Unzipped Nodal Points .	70
28.	Initial Conditions for Calculation of a Steel Projectile of Velocity 0.75 km/sec Impacting a Steel Target	72

29.	Cross Section (a) Through Target Recovered from Shot 68C2-4 (0.79 km/sec impact velocity) with Details (b) and (c) of Incipient Shear Bands	73
30.	Unzipping Slide-Line Calculation with Threshold Plastic Strain of 10%	76
31.	Unzipping Slide-Line Calculation with Threshold Shear Band Damage Parameter of 2 (a) 7.98 sec After Impact (b) Comparison of Computed with Observed Penetration Behavior	78
A-1	Shear(S) and Normal(σ) Stress Orientation on a Block Containing a Shear Band	A-13
A-2	Relative Locations of the X-Y Directions, Principal Directions (not necessarily in order), and Initial Orientation of the Shear Band Damage Groups	A-15
A-3	Mohr Diagram for Stresses. Insets show Orientation of Stresses at a Point	A-18
A-4	Mohr Circle for Stress States with a Yieldline for Yielding on the 1-2 Plane	A-20
A-5	Mohr Diagram Illustrating Simultaneous Yield on Three Planes	A-23
A-6	Deviator Stress Diagram Illustrating Three Yield Lines, the Mises Yield Ellipse, and Yield Solutions for Several Stress States ($\xi = \tau = 0$)	A-24
B-1	Static Temperature-Dependent Yield Surface for 4340 Steel R _c 43	B-2
B-2	Static Adiabatic Yield Curves for 4340 Steel	B-3
B-3	One-Dimensional Shear Wave Loading	B-5

TABLES

1.	Composition of an RHA Plate 10 cm (4 in.) Thick	6
2.	Summary of Quasi-Static Tensile Tests on RHA	9
3.	Experimental Parameters for RHA Contained-Fragmenting-Cylinder Experiments	27
4.	SHEAR2 Material Properties Used in Computational Simulations of 4340 Steel Rod Impacting Normally a 4340 Steel Target	74
A-1	Parameters in the CALL to SHEAR3	A-3
A-2	Input Data for SHEAR3	A-7
A-3	Weighting Factors $\sin^2 \psi$ for Relating Damage to Principal Planes	A-17
B-1	Critical Strains for Shear Band Initiation in Various Materials as Calculated from Equation (B-32)	B-15

I INTRODUCTION AND SUMMARY

The objective of this three-year joint BRL/AMMRC/SRI program is to develop improved material models for computationally simulating long rod penetration of spaced armor, thereby providing the capability to predict the behind-the-armor fragment environment for given penetrator attacks as well as to aid in armor and penetrator design.

Our approach to meet this objective has six main parts. First, materials were selected for study, and penetration phenomenology experiments are being performed in which rods are fired at various angles of incidence against target plates. The rod and target specimens are recovered, sectioned, and metallographically examined to reveal the key microstructural damage mechanisms that govern failure of both penetrator and target.

The baseline materials chosen for study are depleted uranium (DU)-3/4 wt% titanium alloy rods fired against rolled homogeneous armor (RHA) targets. Additional materials to be studied are tungsten alloy rods and electroslag-remelt (ESR) steel armor.

In the second part of the program, laboratory material property characterization experiments are being performed, where necessary, to measure the properties that govern the damage mechanisms.

Third, previously developed computational models of the various damage processes are being modified and adapted to describe the observed failure mechanisms.

Fourth, these models are calibrated against the experimental data with computational simulations of the material characterization experiments.

In the fifth part of the approach, the calibrated material models are being incorporated in a two dimensional wave propagation code, HEMP, developed by Dr. Mark Wilkins and coworkers at Lawrence Livermore Laboratory (LLL). This code must be modified somewhat to accommodate the material models.

Finally, in the sixth part of the program the ability of the models to correctly predict the main features of long rod penetration of spaced armor is being assessed and, if the results are promising, the models will then be used to predict behind-the-armor fragment environments and to aid in armor and penetrator design.

The progress made on the program during the first year is summarized below. RHA material was obtained from BRL early in the program, and the metallurgical characterization has been completed (see Tables 1 and 2, and Figures 1-6). Quasi-static tensile tests and dynamic expanding cylinder tests have also been performed by SRI on this material, and plate slap experiments have been performed by BRL personnel. Phenomenology experiments involving single, monolithic RHA targets impacted normally by 4340 steel rods have been completed and analyzed (see Figures 7-9), and in addition, metallurgical examinations have been completed on DU fragments from rods that have impacted spaced RHA targets at oblique angles of incidence (Figures 10 and 11).

The phenomenology experiments performed to date indicate that the primary microstructural damage mode for erosion of the penetrator nose and for plugging of the target is adiabatic shear banding. The primary microstructural damage mode for rear surface armor damage (spall and/or petalling) is probably ductile void nucleation, growth, and coalescence. The primary damage mode for failure of the rear portion of the DU rod is as yet undetermined, although flash x-ray pictures suggest brittle fracture.

Significant progress was made this year on adapting a previously developed ductile void growth model to the armor penetration problem. However, because of the observed importance of adiabatic shear banding in the failure of both penetrators and armor, we have concentrated on

shear band model modification and adaptation during the first year and are withholding judgement on the importance of ductile void kinetics until all the phenomenology results are in.

From available data on expanding cylinders of 4340 steel (Figures 12-16), we confirmed that the onset of adiabatic shear banding can be treated as a simple plastic instability, in agreement with suggestions made by many previous workers. The instability is triggered when the decrease in yield strength caused by adiabatic thermal softening in the prelocalization material exceeds the increase caused by the work hardening (Figures B.1 and B.2). The material becomes globally constitutively unstable at the equivalent plastic strain at which the true effective stress begins to decrease with increasing strain. Thereafter, any perturbation will localize and grow. We derived a simple formula for roughly estimating this critical threshold strain based on the yield stress, work hardening exponent, and the thermal softening coefficient. This formula was found to correctly rank the propensity of various materials to form adiabatic shear bands (see Table B.1), and we expect the formula to be useful for back-of-the-envelope assessment of armor and penetrator materials.

Once the threshold conditions for shear band nucleation are fulfilled, the computational model must describe the shear band numbers, sizes, and degree of coalescence to predict the fragmentation. The associated nucleation, growth, and coalescence models have been calibrated by analysis of available data from contained fragmenting cylinder (CFC) tests on 4340 steels of several hardnesses (see Figures 20-24). The resulting models will be applied during the next year to similar data now being generated for RHA steel and to be generated for DU.

Finally, preliminary computational simulations for normal impacts of long rods on single target plates have been performed with a simple HEMP-like wave propagation code (called TROTT). In these calculations the improved adiabatic shear band model (SHEAR3) was tested, and the feasibility of using SHEAR3 to activate preexisting slide lines was examined. These runs were successful (see Figures 29-31). Furthermore,

penetration mechanisms such as penetrator bulging and impact of the bulge shoulder with the target surface were studied. The results showed that double slide lines will be required in HEMP to handle the case of extreme bulging of the penetrator nose in normal impact, as is expected at impacts near the ballistic limit, and to handle the case of oblique impact when the side of the rod impacts the target surface. Fortunately, Mark Wilkins and coworkers at LLL have recently inserted a double slide line algorithm in one version of HEMP. We have requested this version of HEMP, and we will implement the double slide line algorithm during the next year.

In the remainder of this report we discuss the above topics in some detail, although frequent reference will be made to References 1 through 11, the relevant monthly progress reports. In some cases, for convenience of access, key portions of these references will be - repeated almost verbatim. In Section II we describe both the phenomenology and material characterization experiments. Section III covers the computational model development, the calibration of the models with experimental data (in particular, the calibration of SHEAR3 with 4340 steel data), and the preliminary computational simulations of penetration experiments. In Section IV we discuss our conclusions and outline plans for the coming year.

II EXPERIMENTS

A. Material Selection, Procurement, and Metallurgical Analysis

The baseline materials selected for study in cooperation with BRL and AMPRC personnel were a rolled homogeneous armor steel (RHA) and a depleted uranium alloy (DU). In addition, tungsten alloy penetrator material and ESR steel armor material will be studied.

Early in the program, three 18 inch x 19 inch x 4 inch thick plates of RHA material were shipped to SRI by BRL. The mechanical property and metallurgical characterizations of this RHA material are described in detail in References 5 and 8. The composition was assumed to be the same as that measured from a 4-inch-thick plate of the same heat of RHA by Benck¹² and Hauver¹³, and is given in Table 1.

To our knowledge, the thermal properties of the RHA have not been measured. However, its thermal properties should be similar to those of steels alloyed in the same manner. The Metals Reference Book¹⁴ reports a thermal conductivity of 0.082 cal/hr cm °C and a specific heat of 0.118 cal/g°C for a 3% Ni-Cr low alloy steel.

The alpha phase Hugoniot of this heat of RHA has been measured by Hauver¹³. In plotting the wave velocity (v) versus the particle velocity (u), the Hugoniot is given by: $v = 4.51 + 1.43 u$. The Hugoniot of RHA is very similar to the Hugoniots of pure iron and AISI steel.

Metallographic analysis⁵ showed that the RHA from the 4-inch plate is quite clean for a commercial heat of such dimensions. It should be rated at no more than Field No. 1 on the ASTM inclusion content scale. In general, the physical and microstructural characteristics of this RHA appear reasonably uniform and isotropic within a 7.5-cm (3-inch) central core.

Table 1
COMPOSITION OF AN RHA PLATE 10 CM (4 IN.) THICK*

Element	Wt%
Carbon	0.27
Manganese	0.27
Phosphorous	0.001
Sulfur	0.008
Silicon	3.15
Nickel	3.47
Copper	0.05
Chromium	1.37
Vanadium	0.01
Molybdenum	0.10/0.25
Aluminum	0.03
Iron	Balance

* Taken from reports by Benck¹² and Hauver.¹³

Nevertheless, the mechanical properties exhibit significant anisotropy that is related to the inclusion orientations. To investigate this anisotropy, as well as to study microstructural fracture mechanisms and to confirm that our material is essentially identical to that studied by Benck¹² and Hauver¹³, we performed several smooth round-bar tensile tests on specimens machined in different orientations. These experiments and the results are discussed in detail in Reference 8; in the following paragraphs we summarized the procedures and the key results.

The round-bar tensile specimens were 0.250 inch (6.35 mm) in diameter, 3.750 inches (9.52 cm) in length, and with a 1.0-inch (25.4 mm) gage length. They were machined from the RHA plate in the three principal orientations: in the plane of rolling and parallel to the rolling direction ("rolling" direction), in the plane of rolling and perpendicular to the rolling direction ("long transverse" direction), and the through-the-thickness direction ("short transverse" direction). The rolling direction was identified during the previous metallurgical analysis. The specimens were machined from the plate starting 1 inch (25.4 mm) in from any surface to eliminate edge effects such as hardening from the cutting torch or surface hardening from the rolling process.

Quasi-static uniaxial tensile tests were performed on the specimens in accordance with ASTM Specification E-8. In all cases the specimens were pulled to failure at a crosshead speed of 0.02 inch/min (0.51 mm/min) using a standard Instron testing machine. This gave a nominal strain rate of 10^{-4} sec⁻¹. All tests were performed at room temperature. For one specimen in each orientation, the plastic strain to failure was measured with a calibrated, 1-inch (25.4-mm) gage length extensometer. On the remaining specimens, axial and lateral plastic strain in the neck region was measured using single-frame photography. From these data, we obtained load-deflection curves and true stress-true strain curves for each orientation.

One fractured specimen in each orientation was sectioned along its axis to study the void growth characteristics in the neck region and beyond. In addition, the fracture surface of one specimen in each orientation was examined using scanning electron microscopy (SEM).

Table 2 summarizes the test results for each specimen. The true fracture stress (TFS) was determined by dividing the load at failure by the minimum cross-sectional area of the neck at failure. It is apparent that the rolling and long traverse directions exhibit similar properties but that the short transverse direction exhibits significantly degraded properties, particularly in the ductility-dependent properties (true fracture stress, elongation to failure, and reduction in area). This type of anisotropy between the rolling plane and the through-the-thickness plane is characteristic of thick, as-rolled plates.

Figure 1 shows the true stress-true strain behavior of specimens R-1 (rolling direction), L-2 (long transverse direction), and S-2 (short transverse direction) as measured from the photographs of the neck. The loading path in true stress-true strain space is same in all three directions. The only significant discrepancy between the rolling and long transverse directions and short transverse direction is in true strain to failure. Hence, the deformation in all three directions should be describable by the same flow equation. These data (at least up to a true strain of 0.8) are describable by a power law hardening equation of the form:

$$\sigma = K\epsilon^N$$

where σ = true stress, $K = 200$ ksi (1.38 GPa), ϵ = true strain, and $N = 0.19$.

Also plotted in Figure 1 are the true stress-true strain quasi-static tensile data on 4-inch-thick (10.16-cm) RHA plate reported by Benck¹² at BRL.* Although there is some scatter, the SRI data and the

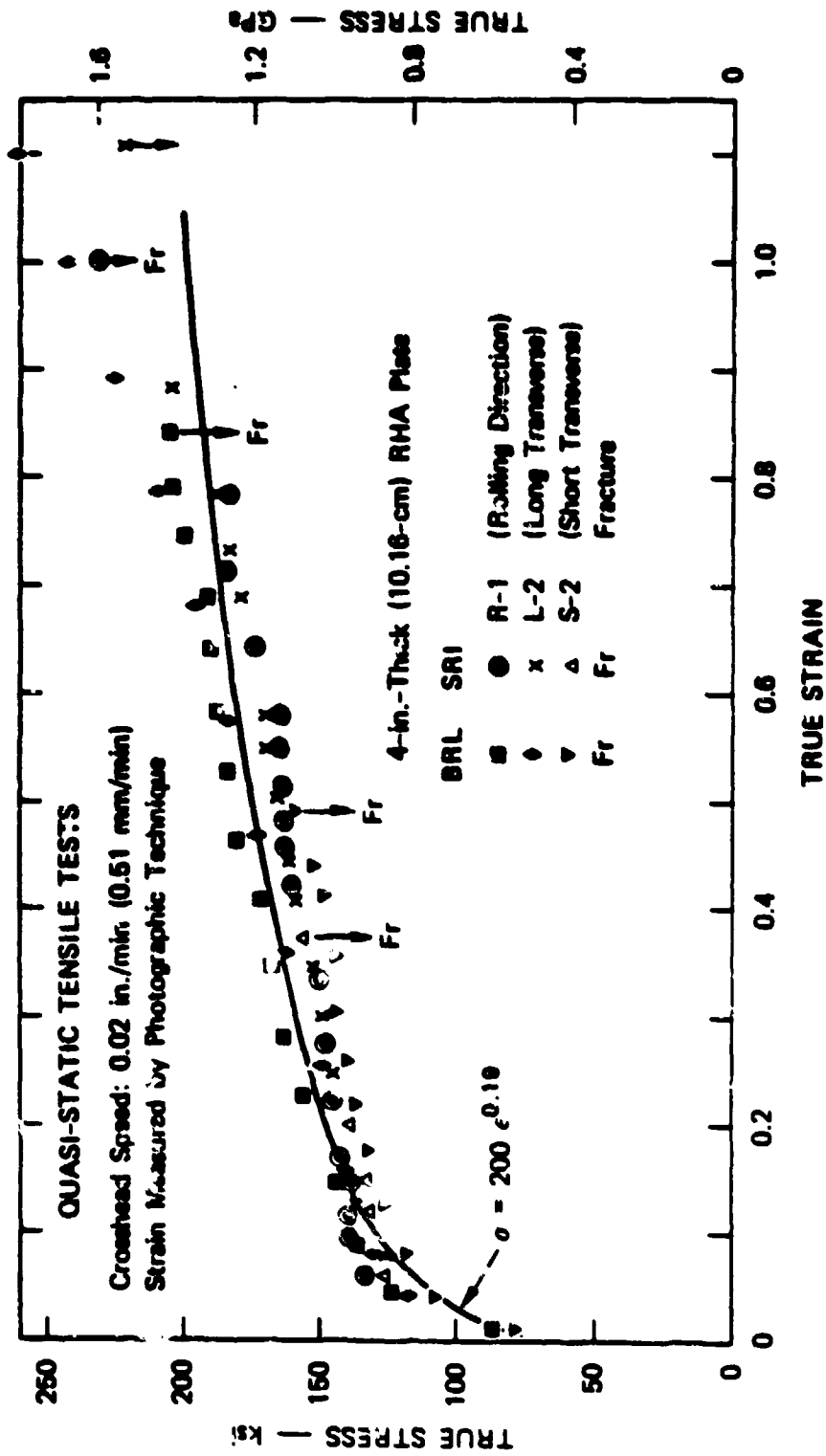
*The values of K and N in Equation (II-1) were calculated using both the SRI data and the BRL data.

Table 2

SUMMARY OF QUASI-STATIC TENSILE TESTS ON BHA

Specimen Orientation	E, 10 ³ ksi (GPa)	Y, ksi (MPa)	UTS, ksi (MPa)	TFS, ksi (GPa)	e, %	R.A., %
Rolling direction (R)						
R ₁	28 (190)	101 (696)	126 (869)	230 (1.59)	32	64
R ₂	28 (190)	100 (690)	124 (855)	204 (1.41)	25	50
R ₃	28 (190)	102 (703)	122 (841)	225 (1.55)	25	62
Long transverse (L)						
L ₁	31 (210)	103 (710)	121 (834)	230 (1.59)	26	66
L ₂	31 (210)	100 (690)	122 (841)	225 (1.55)	30	67
L ₃	31 (210)	99 (683)	120 (827)	222 (1.53)	28	66
Short transverse (S)						
S ₁	31 (210)	95 (655)	117 (807)	147 (1.01)	16	29
S ₂	31 (210)	95 (655)	116 (800)	154 (1.06)	14	29
S ₃	31 (210)	96 (662)	115 (793)	122 (0.84)	12	20

E: Young's modulus
 Y: 0.2% offset yield strength
 UTS: ultimate tensile strength
 TFS: true fracture stress
 e: elongation to failure
 R.A.: reduction in area



MA-7883-25

FIGURE 1 TRUE STRESS-TRUE STRAIN CURVES FOR RHA SPECIMENS TESTED IN THE THREE PRINCIPAL DIRECTIONS

data collected at BRL in the three plate orientations agree reasonably well (compare also Table II in Benck¹² with Table 2 in this report). The data of BRL also indicate anisotropic behavior in the through-the-thickness direction. It thus appears probable that the RHA plate tested by SRI is from the same 4-inch-thick (10.16-cm) plate of RHA tested by Benck and that spot-to-spot variations in this plate do not appear to be excessive. Therefore, the results of dynamic and static failure mode experiments conducted by SRI on RHA can be fairly compared with the results of the experiments conducted at BRL.

These tensile test results indicate that this 4-inch-thick (10.16 cm) plate of RHA exhibits significantly reduced ductility in the through-the-thickness direction relative to the rolling plane directions. Moreover, microstructural characterization indicated that this RHA plate was reasonably isotropic with respect to grain size, grain shape, and constituent phases; hence, these microstructural characteristics cannot be the cause of the ductility anisotropy. However, the microstructure was observed to contain large, nonuniformly distributed MnS inclusions. The inclusions were either roughly spherical or oblong, 10 to 20 μm in diameter, and concentrated in clusters that were elongated in the direction of rolling.

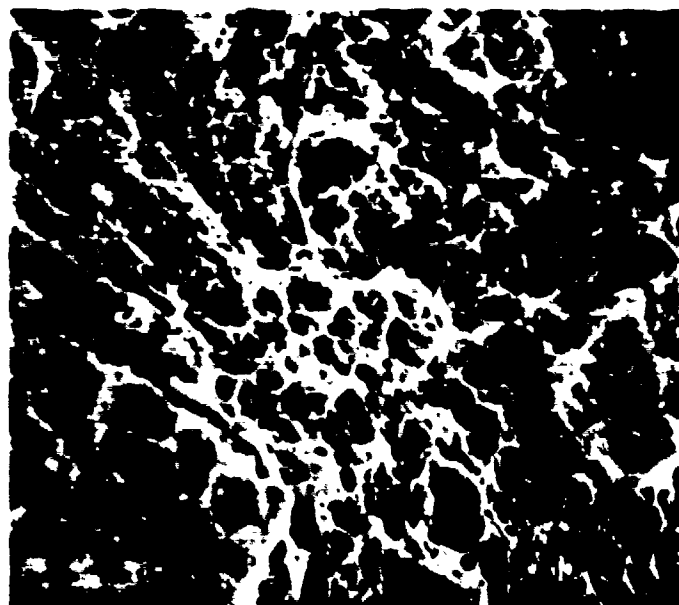
Figure 2 is a scanning electron micrograph of the fracture surface of specimen R-1 (rolling direction). The fracture surface exhibits a cup-and-cone type of fracture, that is, tensile void nucleation, growth, and shearing of the remaining ligaments between the voids in the center of the specimen, followed by shearing around the periphery. Specimen L-2 (long transverse direction) exhibited a similar fracture surface. Figure 3 details the void structure in the center of specimens R-1 and L-2. The voids in both specimens are in general small ($\sim 1 \mu\text{m}$), spherical, and quite deep. The particles that nucleated these voids could not be identified, but their small size suggests that they were nucleated around the fine ($\sim 1 \mu\text{m}$), uniformly dispersed iron carbide (Fe_3C) particles characteristic of a bainitic microstructure.¹⁵ It thus appears that the fracture process in the rolling and long transverse specimens is controlled by the nucleation and growth of voids



1 mm

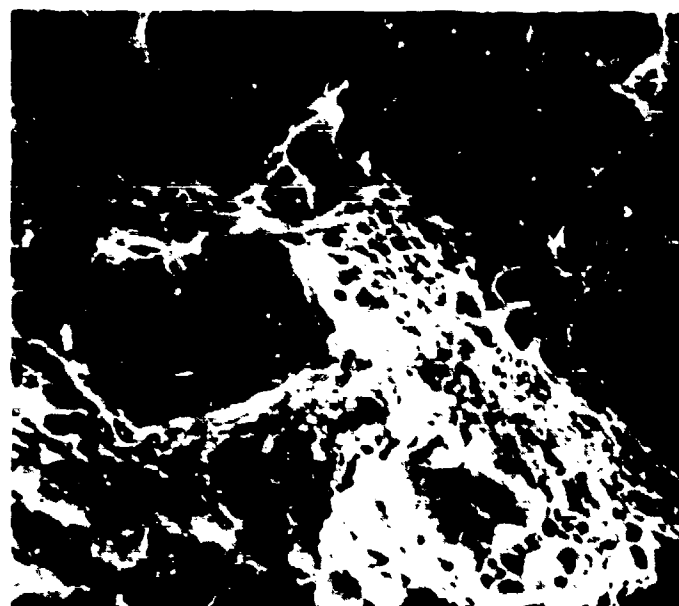
MP-7993-27

FIGURE 2 SEM OF THE FRACTURE SURFACE OF SPECIMEN R-1 (Rolling Direction)
SHOWING THE CONVENTIONAL CUP-AND-CONE TYPE OF FRACTURE



2 μm

(a) SPECIMEN R-1 (Rolling Direction)



2 μm

(b) SPECIMEN L-2 (Long Transverse Direction)

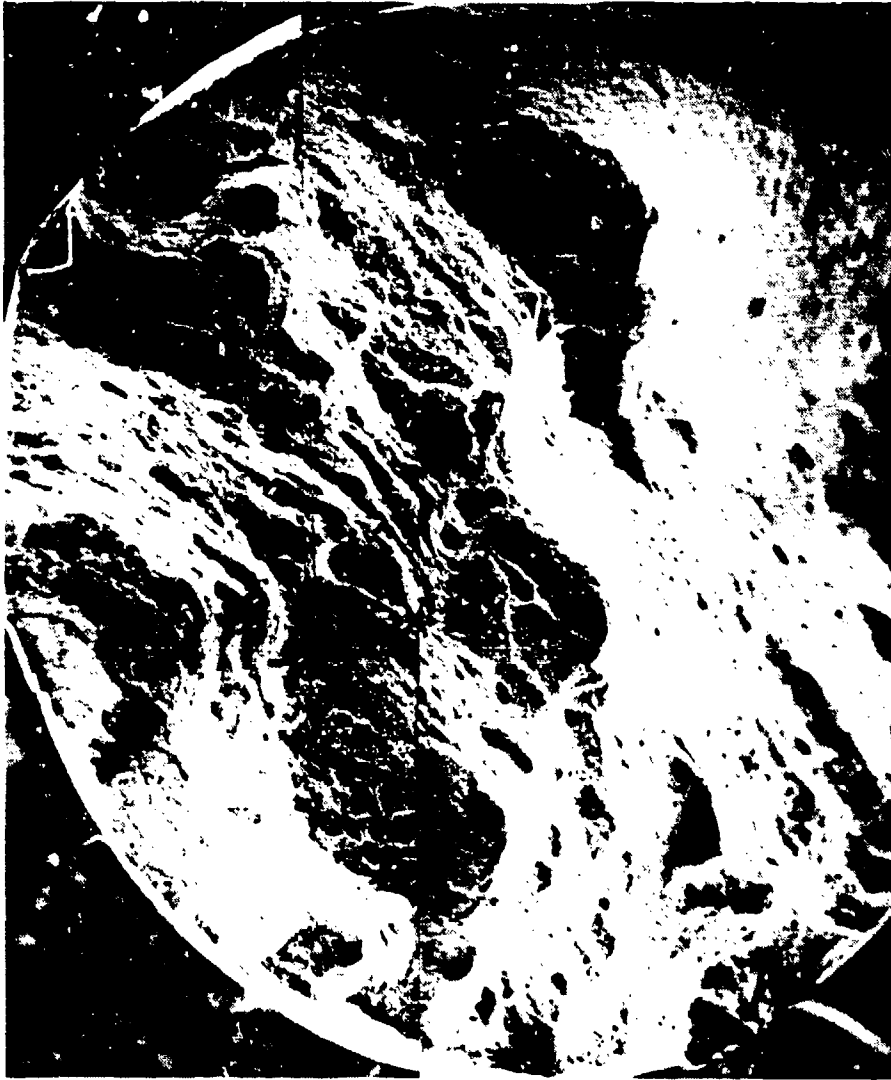
MP-7893-28

FIGURE 3 DETAILS OF THE VOID STRUCTURE IN THE CENTER OF THE FRACTURE SURFACES OF SPECIMENS R-1 AND L-2

around the small, uniformly dispersed Fe_3C particles. The larger MnS inclusions that are concentrated along planes parallel to the rolling direction do not appear to significantly affect the fracture process of the rolling and long transverse specimens.

Figure 4 is a scanning electron micrograph of the fracture surface of specimen S-2 (short transverse direction). Approximately 60% of the fracture surface exhibits a ductile dimple characteristic, and approximately 40% exhibits a shear lip. The asymmetric appearance of the fracture surface suggests that the ductile dimple fracture process was controlled by the nucleation and growth of voids around a nonuniform distribution of large inclusions. Figure 5(a) shows some of the large, elongated dimples found on the flat part of the fracture surface. The particles visible at the bottom of the voids were identified as MnS by nondispersive x-ray analysis. The large dimples visible in Figure 8(a) are larger than any found on the fracture surfaces of the rolling plane specimens (Figure 3). However, the fracture surface of the shear lip, Figure 5(b), is very similar in appearance to the fracture surfaces of the shear lips on the rolling plane specimens (R-1 and L-2). It thus appears that the lower ductility observed in the short transverse specimens can be attributed to the nucleation and growth of large voids across at least part of the neck region, followed by plastic tearing of any remaining ligament. It also appears that these large voids were nucleated around large MnS particles observed to be concentrated in clusters elongated in the direction of rolling.

Figure 6 shows the polished cross sections of one fracture specimen in each of the three principal directions. The size and distribution of voids in the vicinity of the neck in specimens R-1 [Figure 6(a)] and L-2 [Figure 6(b)] are quite similar. As expected, the void size and distribution are much different in specimen S-2 [Figure 6(c)] in which a number of large voids are concentrated primarily under the flat portion of the fracture surface. It is these voids that reduce the ductility of the short transverse specimens relative to the rolling and long transverse specimens. Note also that the voids in specimens R-1 and L-2 are elongated in a direction parallel to the load, while

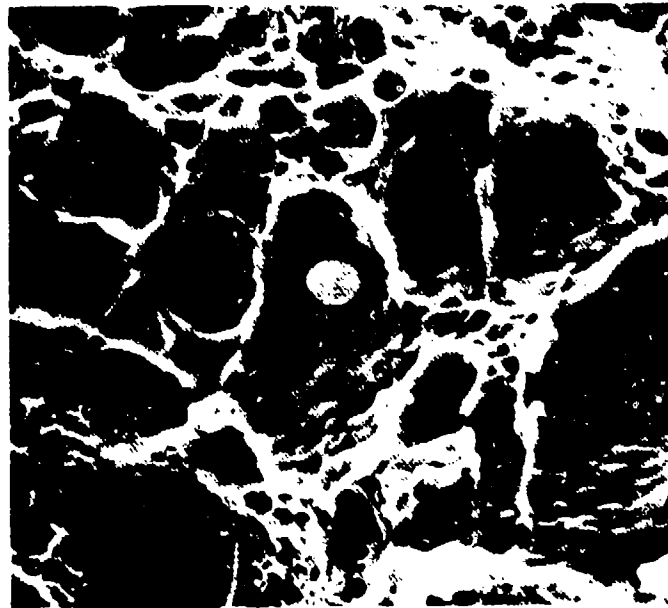


1 mm

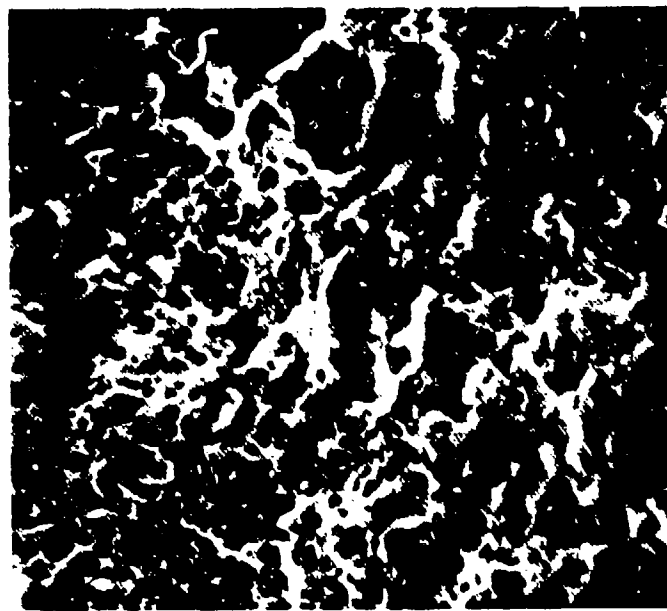
MP-7893-29

FIGURE 4 SEM OF THE FRACTURE SURFACE OF SPECIMEN S-2 (Short Transverse Direction)

Approximately 60% of the fracture surface exhibits a ductile dimple characteristic, and approximately 40% is covered by a shear lip (compare with Figure 2).



(a)



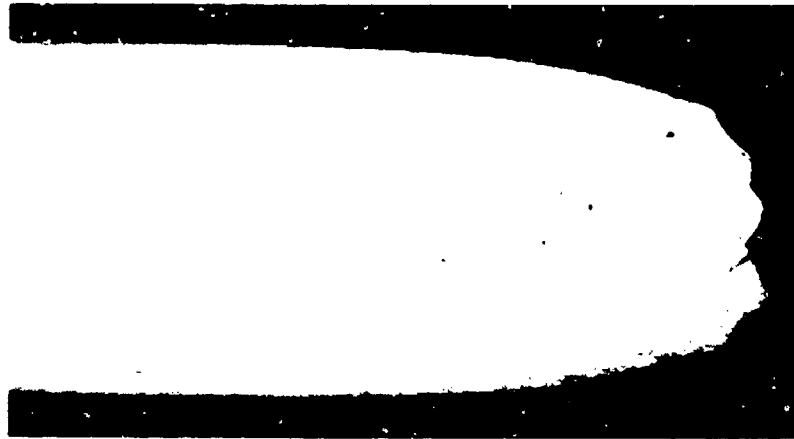
(b)

MP-7893-30

FIGURE 5 DETAILS OF THE FRACTURE SURFACE OF SPECIMEN S-2 (Short Transverse Direction)

(a) Shows the large elongated ductile dimples characteristic of 60% of the fracture surface.

(b) Shows that the shear lip is covered by small shallow dimples distorted by shear.



(a) SPECIMEN R-1 (Rolling Direction)



(b) SPECIMEN L-2 (Long Transverse Direction)



(c) SPECIMEN S-2 (Short Transvers Direction)

MP-7893-31

FIGURE 6 POLISHED CROSS SECTIONS OF TENSILE SPECIMENS IN THE THREE PRINCIPAL ORIENTATIONS COMPARING RELATIVE INTERNAL VOID ACTIVITY IN THE VICINITY OF THE NECK

the voids in specimen S-2 are elongated in a direction perpendicular to the load. This indicates that the large MnS inclusions in the short transverse specimens are elongated in a direction perpendicular to the load axis (parallel to the rolling direction) and that the voids nucleated by such inclusions had not grown much by plastic flow (had not elongated in the loading direction) at the time of fracture.

We conclude that the observed mechanical anisotropy is due to clusters of large MnS inclusions elongated in the rolling direction. The fracture process in the rolling and long transverse directions is controlled by the nucleation and growth of voids around the fine ($< 1 \mu\text{m}$) uniformly dispersed Fe_3C particles characteristic of bainitic microstructures, followed by shearing of the remaining ligaments. The fracture process in the short transverse direction is controlled by the nucleation and growth of voids around the large MnS inclusions elongated in the direction of rolling, followed by shearing of the remaining ligaments.

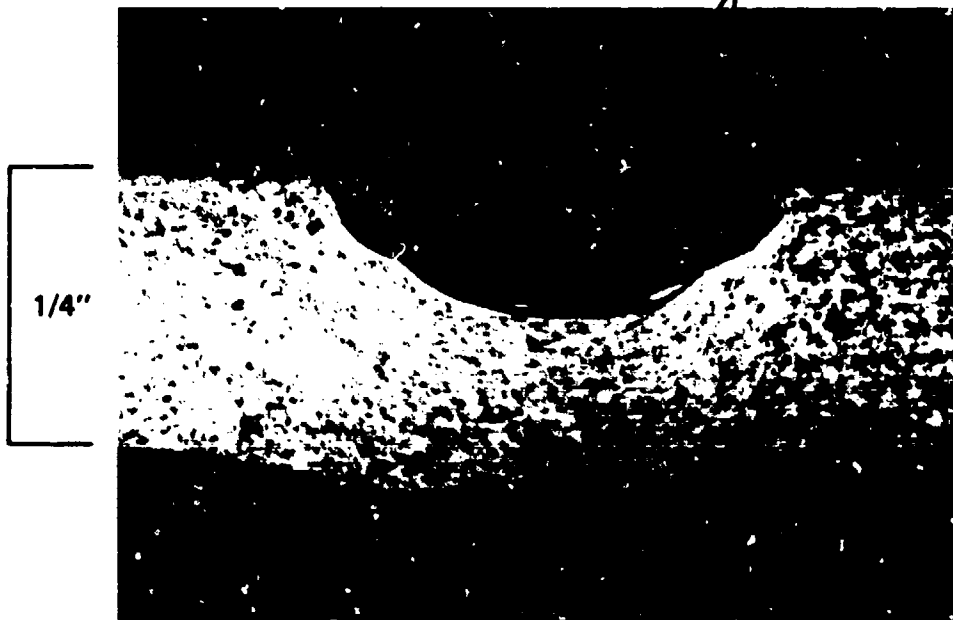
B. Phenomenology Experiments

1. Response of RHA to Normal Impacts of Long Steel Rods

We performed a series of experiments in which flat-nosed 4340 rods ($R_c 50$) were fired at normal incidence into RHA plates. The rods were 1/4 inch (0.635 cm) thick and 1/2 inch (1.27 cm) long. The RHA target plates were machined from the plate discussed above and were 3 inches (1.18 cm) square and 1/4 inch (0.635 cm) thick. The impact velocities were chosen to range from just below to just above the ballistic limit, and the targets were recovered and sectioned after the shots for metallographic examination.

The results are shown in Figures 7 through 9. Several observations can be made immediately. First, the RHA material is fairly resistant to shear banding. Nevertheless, the target failure mechanism is shear banding and resultant plugging. Second, shear banding is the erosion mechanism for the nose of the 4340 steel

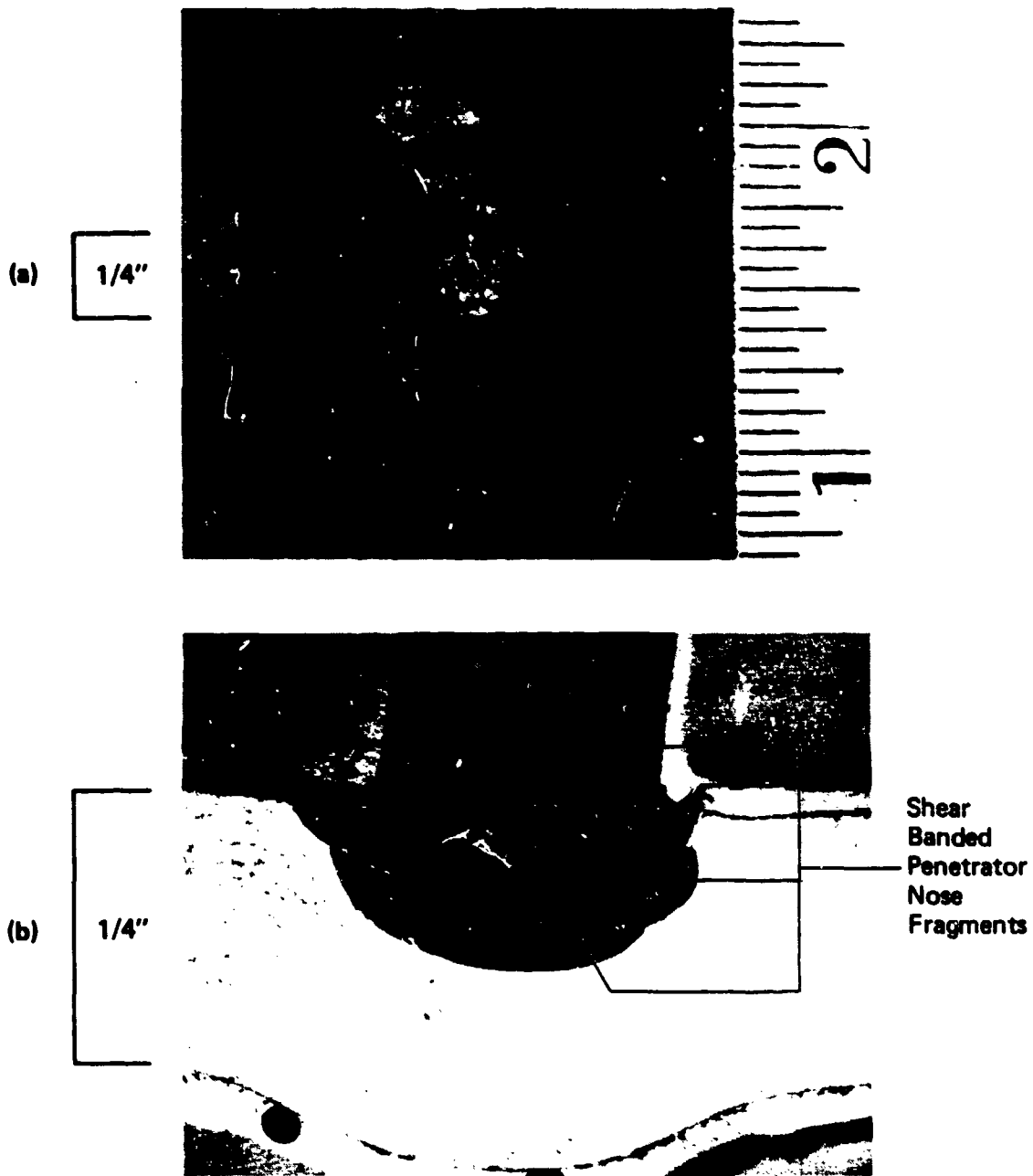
Shear Banded
Projectile Nose
Fragments



MP-7983-32A

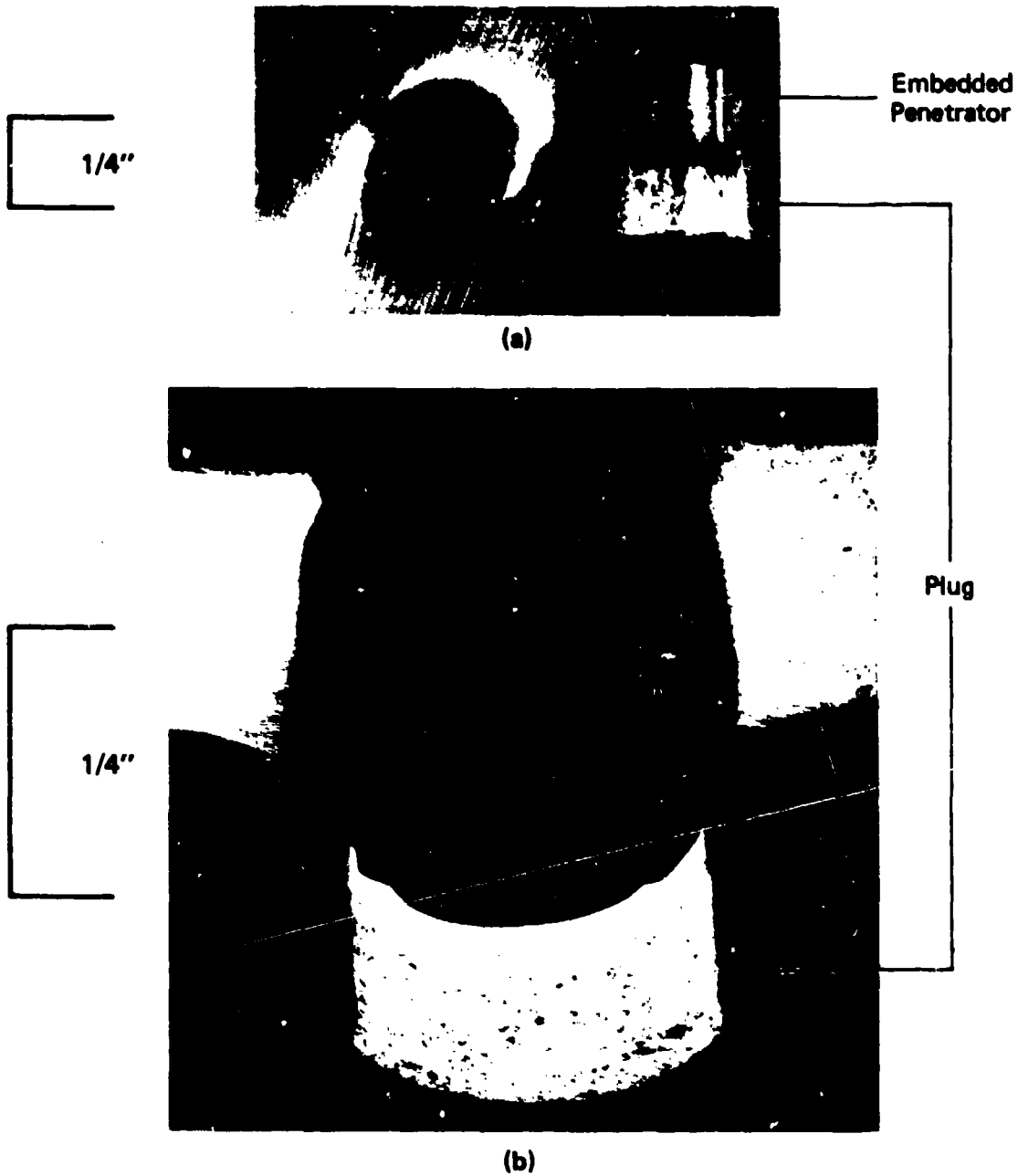
FIGURE 7 POLISHED AND ETCHED CROSS SECTION THROUGH CENTER OF RHA TARGET IMPACTED BY A BLUNT-NOSED 4340 STEEL PROJECTILE AT 2150 FT/SEC (655 m/sec)

Note absence of shear banding in target material.



MP-7893-41A

FIGURE 8 IMPACT SIDE OF (a) AND POLISHED AND ETCHED CROSS SECTION (b) THROUGH CENTER OF RHA TARGET IMPACTED BY BLUNT-NOSED 4340 STEEL PROJECTILE AT 2330 FT/SEC (710 m/sec)



MP-7893-42A

FIGURE 9 BLUNT-NOSED 4340 STEEL PROJECTILE WITHIN PLUG ON REAR SURFACE OF TARGET PLATE (a) AND POLISHED AND ETCHED CROSS SECTION THROUGH RHA TARGET AND PLUG FOLLOWING IMPACT AT 2600 FT/SEC (792 m/sec) (b)

penetrators. Notice that the mushrooming nose fragments cause a discontinuous or scalloped crater in the target. Finally, the mushrooming effect of the fragmenting penetrator nose combined with the resistance of the RHA to shear banding and plugging has caused the onset of shear banding in the RHA to occur first at a radius around the impact center that is significantly greater than the original radius of the penetrator. (Figure 9 shows a case where the plug radius is about 33% larger than the original penetrator radius.)

2. Response of RHA to Oblique Impacts of Long DU Rods

In cooperation with BRL and AMRC personnel, we have procured DU penetrator rods for use in penetration phenomenology experiments involving impacts at various velocities and angles of incidence against single and multiple RHA target plates. These DU rods are described in Section V. Posttest recovery and metallographic examination of sectioned target and penetrator fragments will be made to study the microstructural failure modes. A key consideration is the influence of the failure mechanisms on scaling. For example, brittle fracture of the rear portion of the penetrator using bending stresses is expected to be sensitive to the plastic zone size,

$$\delta_c = A(K_{1c}/\sigma_y)^2, \quad (\text{II-2})$$

where A is a geometry-dependent coefficient, K_{1c} is the fracture toughness, and σ_y is the yield stress.¹⁶

At the date of this writing, these phenomenology experiments have not yet been completed. However, preliminary information has been obtained from metallographic examination of samples from experiments performed at BRL in which DU penetrators were fired obliquely at RHA targets. Figure 10 shows polished sections of the rear portion of a 65-g DU rod that had penetrated scaled triple armor with an impact velocity of 985 m/sec and a residual velocity of 562 m/sec. (The angle of incidence is unknown). Figure 11 shows a section through a RHA

target in which a DU fragment is embedded. (The impact velocity and the angle of incidence are unknown.)

It is clear from Figures 10 and 11 that adiabatic shear banding was the key failure mechanism of the penetrator nose in both cases. Of particular interest is the band shown in Figure 11. Here the martensitic platelets are seen to bend sharply as they enter the band, showing clearly the localization of plastic strain.

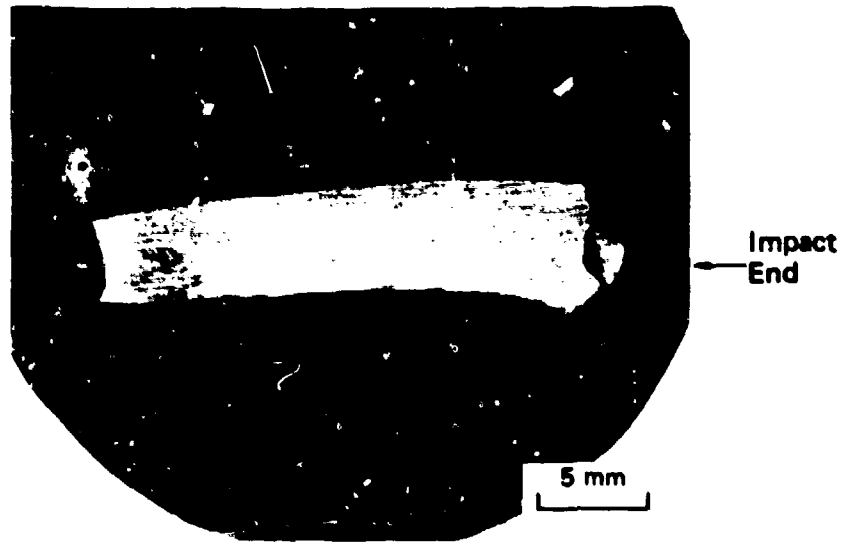
The shear bands in Figures 10 and 11 were also seen to contain voids, in agreement with observations reported by Rogers.¹⁷

In summary, although definite conclusions must await completion of the phenomenology experiments, it appears that shear banding is the key damage mechanism for both the RHA target and the nose of the DU penetrator. However, we expect that ductile void growth will also be important for high impact velocity cases for which back surface spall occur.

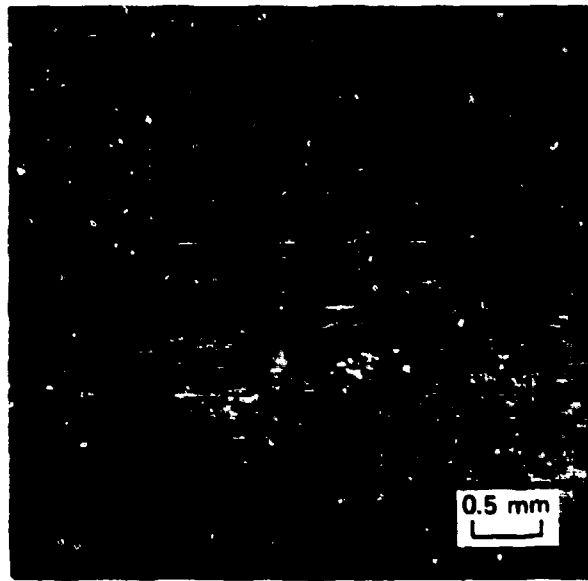
3. Response of RHA to Impacts of Long Tungsten Alloy Rods

AMTRC personnel are planning to perform a series of oblique impact experiments with long tungsten alloy rods. Discussions have been held with John Mescall of AMTRC to determine if posttest recovery of fragments will be possible to examine failure phenomenology. In addition, BRL personnel plan to perform normal impact experiments with tungsten alloy rods ($L/D = 10$) fired against 2-inch-thick RHA target plates that are instrumented with stress gages. Discussions with George Hauver of BRL have been held to plan for posttest recovery of penetrator and target fragments for failure phenomenology examinations at SRI.

Thus, tungsten alloy penetrator failure phenomenology data should be forthcoming during the next year.



(a) Overall view of the recovered penetrator showing how the impact end was fractured and the shaft bent during perforation.



(b) View of the microstructure of the penetrator shaft back from the impact end. The holes most likely resulted from oxide inclusions strung out along the extrusion axis and then pulled out during grinding and electropolishing.

MP-7893-70

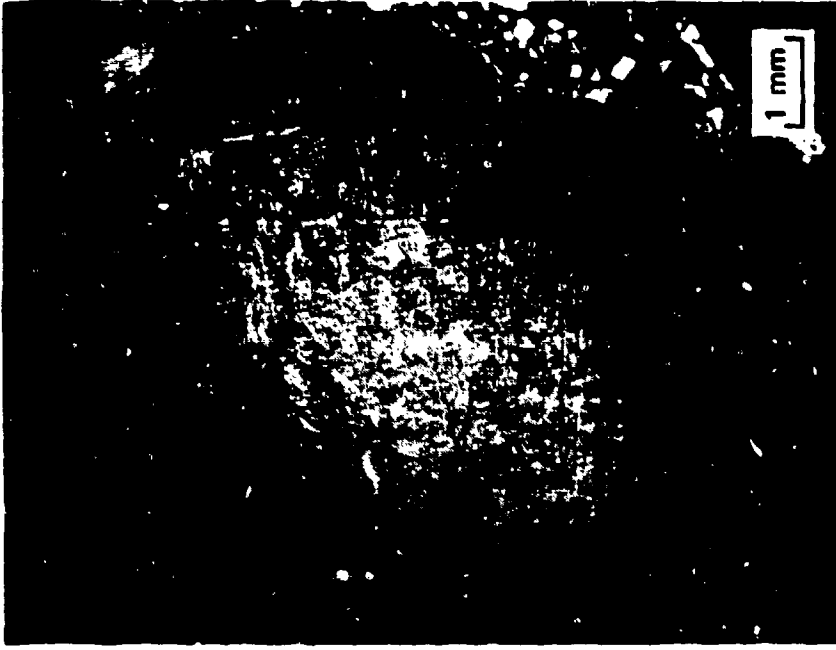
FIGURE 10 RECOVERED URANIUM-3/4 wt% TITANIUM AFTER PERFORATION OF SCALED TRIPLE ARMOR (First Plate: 0.24 cm; Second Plate: 0.68 cm; Third Plate: 1.26 cm)

The impact velocity was 985 m/sec and the residual velocity was 562 m/sec. The residual mass was 12.8 g.



(a) Overall View of Penetrator Fragment Embedded in Target

The target plate was cut in half, ground on 600 grit paper, and electropolished in a solution of 178 g CrO_3 dissolved in 100 cc distilled water and four parts glacial acetic acid. The voltage was 20 VDC, 0.8 A, held for 5-6 minutes.



(b) More Detailed View of Penetrator Fragment

The wavy lines in the fragment are prior γ grain boundaries. Note also the flat surface oriented perpendicular to the penetrator axis.

MP-7600-67

FIGURE 11 STEEL TARGET PLATE No. 4 IMPACTED AT AN OBLIQUE ANGLE BY A URANIUM-3/4 wt% TITANIUM ALLOY PENETRATOR

C. Material Characterization Experiments

1. Contained Fragmenting Cylinder (CFC) Experiments

The CFC experiments were developed in an earlier project¹⁸ to measure the parameters in our computational model for shear banding. The technique, described in detail in Reference 18, entails detonating explosive in a thick-walled tube of the material of interest. The tube is surrounded by concentric layers of plastic and steel respectively, so that the expansion of the inner tube can be halted at various stages of development by varying the thickness of the plastic layer. The explosive density can also be varied, and the strain histories can thereby be tailored by varying the explosive density and the plastic layer thickness. The strain histories throughout the specimen tube are calculated with our two-dimensional wave propagation code, TROTT.

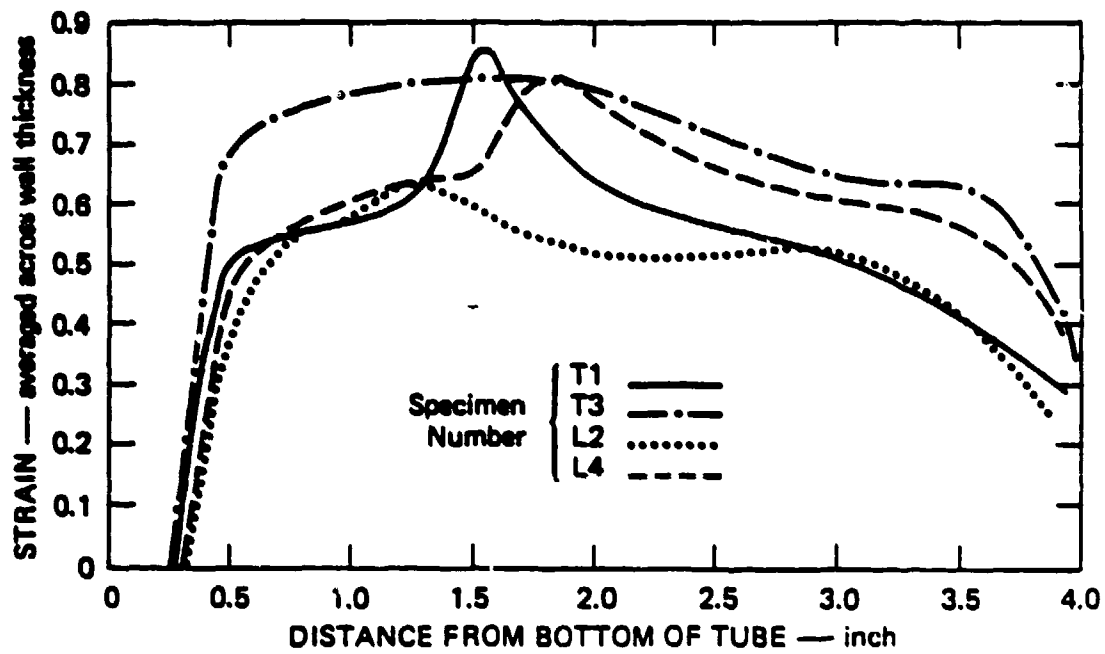
To date, four CFC experiments have been performed using RHA specimen tubes having a length of 3-3/4 inches, an I.D. of 1-1/8 inches, and a wall thickness of 1/4 inch. The experimental parameters and some qualitative results are shown in Table 3. The recovered specimen tubes were sliced in half along a plane containing the axis, and the final wall thickness was measured as a function of axial position. The equivalent plastic strain ($\bar{\epsilon}^P$) was calculated by the formula $\bar{\epsilon}^P = \sqrt{3} \epsilon_r \left(1 + \frac{\epsilon_z}{4\epsilon_r}\right)$, where ϵ_r (the radial plastic strain) equals the natural logarithm of the ratio of the final wall thickness to the original wall thickness and ϵ_z (axial plastic strain) equals the fractional increase in length of the specimen. Figure 12 shows the results for all four specimen tubes in terms of equivalent plastic strain versus axial position.

Metallographic examinations have been completed on the RHA specimen tubes L2 and L4, whose axes were parallel to the long transverse direction of the RHA slab. Figure 13 contains two views of one half of the specimen L4, showing large shear band damage extending almost the entire length of the tube, but concentrated in two specific circumferential regions, and lesser damage adjacent to these regions. A polished and etched section perpendicular to the axis of the tube

Table 3
EXPERIMENTAL PARAMETERS FOR DMA
CONTAINED FRAGMENTING CYLINDER EXPERIMENTS

Specimen Number	Orientation of Axis	PSTM Density	Lucite Buffer Thickness (cm)	Qualitative Results
L2	Long transverse	1.0	0.873	Extensive Mode 1 ^a shear banding concentrated in rolling direction.
L4	Long transverse	1.2	0.873	Extensive Mode 1 shear banding concentrated in rolling direction.
T1	Short transverse	1.2	0.873	No shear banding seen. Tensile cracking concentrated in specific axial region on outer surface.
T3	Short transverse	1.35	0.873	Incipient Mode 1 shear banding on inner surface over most of specimen tube. Tensile cracking on outer surface.

^a As defined in Reference 8.



MA-7893-45A

FIGURE 12 EQUIVALENT PLASTIC STRAIN DETERMINED FROM MEASUREMENTS OF RHA SPECIMEN TUBES RECOVERED FROM CFC EXPERIMENTS



MP-7893-43

FIGURE 13 TWO VIEWS OF HALF OF THE RHA SPECIMEN TUBE L4 RECOVERED FROM CFC EXPERIMENT

(Plane in Figure 14 is cut at a distance of 2-3/8" from bottom of specimen tube.)

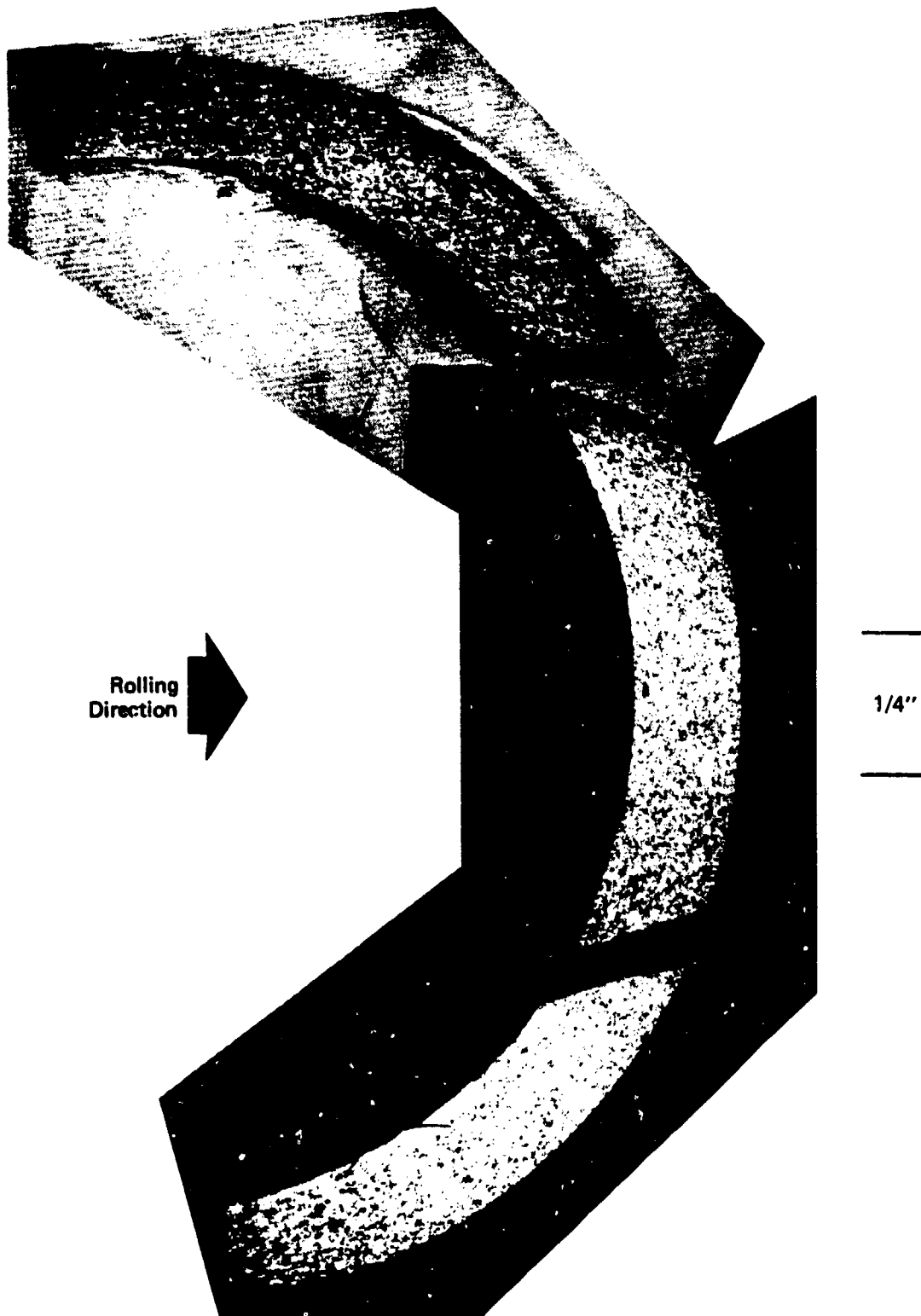
at a distance of 2-3/8 inches from the bottom end is shown in Figure 15. Except for a few small bands, all of the shear bands--from the incipient bands barely noticeable along the inside radius to the couple of large bands that have extended completely through the tube--have a direction that is approximately parallel (within about 15°) to the rolling direction. This anisotropy is caused by planes of shear weakness in the rolling direction due to the rolling process.

We then machined the specimen tubes labeled T1 and T3 with the tube axis in the short transverse direction, as shown in Figure 15. It is clear from Figure 15 that shear bands that cut across the rolling direction should be easier to produce in the short transverse specimens, because in these specimens the plane of weakness induced by rolling will be closer to the mode 2 orientation, as defined in Figure 16, and the tube expansion in the mode 2 orientation produces only about half the resolved shear strain produced in the mode 1 orientation.

Indeed, the recovered specimens labeled T1 and T3 in Table 3 showed a large number of mode 1 incipient bands distributed uniformly around the circumference; the bands appeared only after equivalent plastic strains greater than about 80%, as compared to a nucleation threshold strain of less than 50% for the bands in the rolling plane in the L specimens.

The following conclusions can therefore be drawn from work completed to date: (1) there is a significant anisotropy in the resistance of RHA to shear banding; (2) bands in planes parallel to the rolling plane nucleate at equivalent plastic strain ($\bar{\epsilon}^P$) less than 50%, whereas bands in planes perpendicular to the rolling plane nucleate ($\bar{\epsilon}^P$) \approx 80%; and (3) our computational shear-banding model may have to account for this anisotropy.

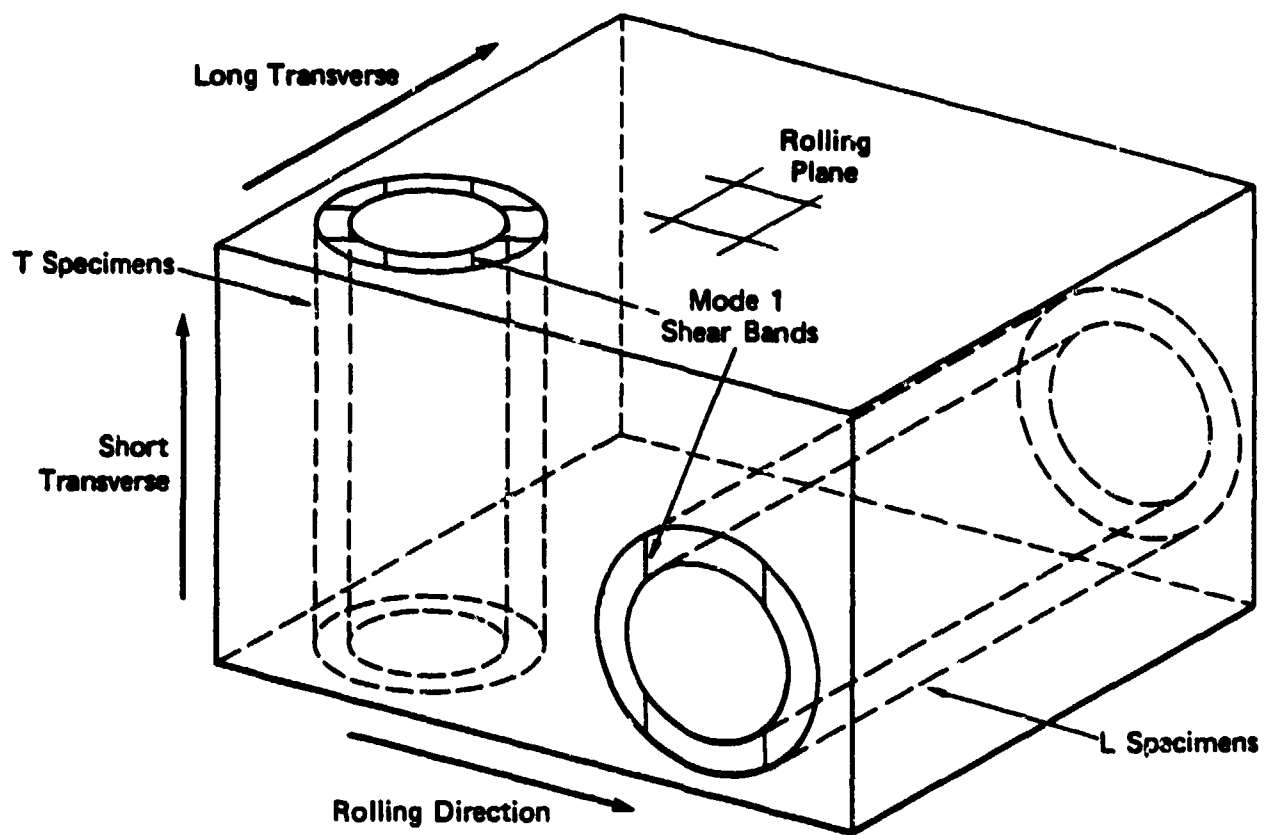
In armor penetration (specifically by a blunt-nosed projectile impacting at right angles) plugging is caused by growth of shear bands in planes perpendicular to the rolling plane. These bands can be activated in CFC specimens with axes parallel to the short transverse direction of the RHA slab (T-specimen). Incipient shear-band levels



MP-7893-44

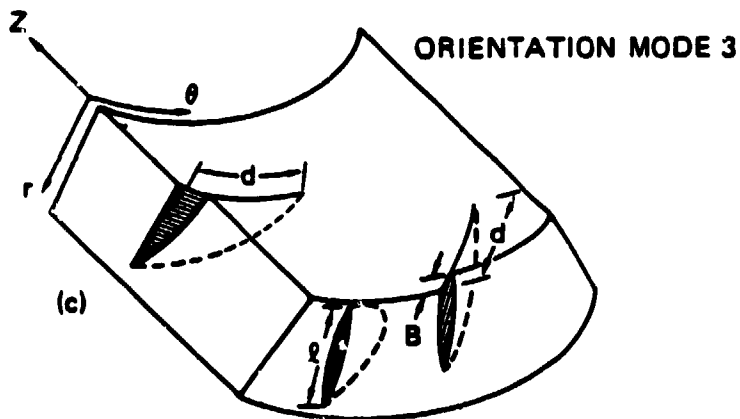
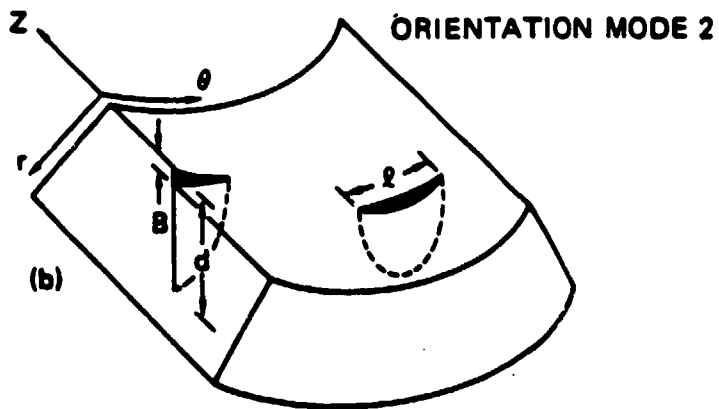
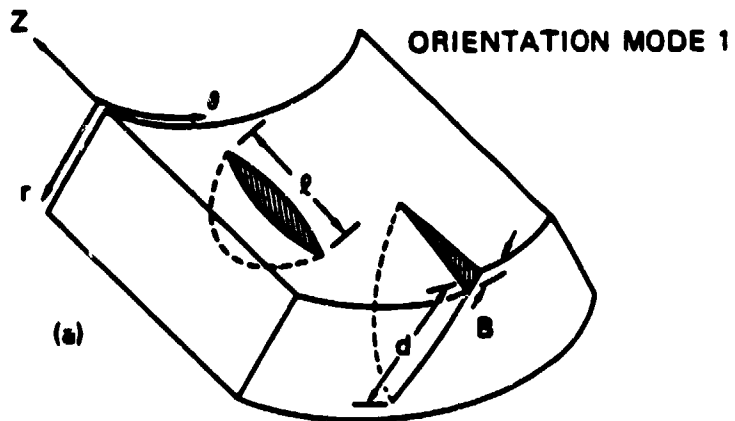
FIGURE 14 POLISHED AND ETCHED SECTION THROUGH RHA SPECIMEN TUBE L4,
SHOWING PREPONDERANCE OF SHEAR BANDING DAMAGE IN ROLLING
DIRECTION

(Plane is cut at a distance of 2-3/8" from bottom of specimen tube.)



MA-7893-47

FIGURE 15 CFC SPECIMENS MACHINED FROM RHA SLAB, SHOWING MODE 1 SHEAR BANDS IN PLANES PERPENDICULAR TO ROLLING PLANE



- | | |
|----------|--|
| l | – Length in Direction
Perpendicular to
Slip Motion |
| d | – Depth Along 45°
Slip Plane |
| B | – Shear Displacement
Along Slip Plane |
| Z | – Axial Direction |
| r | – Radial Direction |
| θ | – Circumferential
Direction |

FIGURE 16 GEOMETRY AND NOMENCLATURE FOR SHEAR BANDS IN CONTAINED-FRAGMENTING-CYLINDER EXPERIMENTS

MA-5084-21

have been achieved thus far; shots are now under way to produce higher damage levels.

Shear banding in planes parallel to the rolling plane may be important in other armor-penetrator geometries (e.g., oblique impact of hemispherical-nosed or ogival-nosed projectiles), particularly in the case of RHA, which is less resistant to shear banding in those planes. These bands can be activated in CFC specimens with axes parallel to the long transverse direction (L-specimen). If future phenomenology experiments show that these bands are important, additional CFC experiments will be performed with L-specimens to obtain incipient to moderate levels of damage (higher levels of damage have already been obtained).

2. Symmetric Taylor Tests

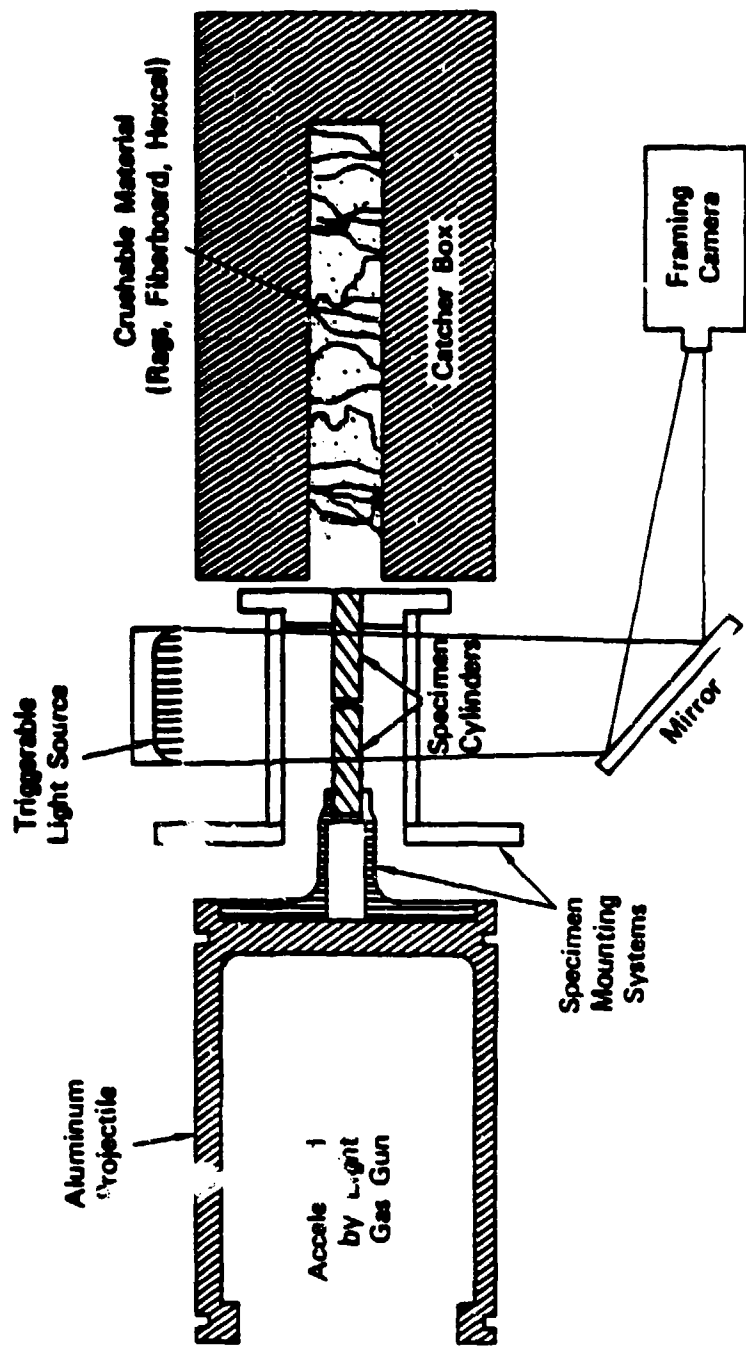
As will be discussed in Section III, the dynamic (adiabatic) stress-strain curve above yield is an important component in our computational damage models. The onset of shear banding is particularly sensitive to the dynamic work hardening and adiabatic thermal softening. In addition, ductile void growth and the size of the plastic zone (which governs the resistance of the penetrator rod and target plate to brittle fracture; see Eq. II-2) are strong functions of the dynamic yield function. We therefore need to obtain yield data at the rates of interest for RHA and DU (as well as for tungsten alloy and ESR steel later in the program).

The strain rates of interest range from 10^2 sec^{-1} to 10^5 sec^{-1} , a relatively inaccessible and largely unexplored region of measurement. The two experimental methods that appear to hold the most promise for exploring this strain rate region are the dynamic torsion test¹⁹ and a modification of the Taylor test.^{20,21}

The dynamic torsion test is currently being developed and adapted to measurements on armor and penetrator materials under contract with BRL by Minneapolis Honeywell Corporation.²² Therefore, in our work we have concentrated on a modified version of the Taylor test.²⁰

The classical Taylor test involves impacting a rod on a rigid surface. Our modified version entails the symmetric impact of two identical right circular cylinders, each about 3/8 inch in diameter and 1-1/2 inch long (these dimensions may be varied). Figure 17 shows a schematic drawing of the experiment. One of the cylinders is accelerated by a light gas gun to a velocity in the range of 0.5 to 1.0 km/sec, where it impacts a stationary cylinder. Both cylinders are supported by stiff, but weak fixtures, so that the supporting fixtures interface negligibly with the wave propagation and deformation resulting from the impact. Immediately following impact, a high-speed framing camera records a series of photographs at approximately 1,000,000 frames/sec to produce a record of the "mushrooming" plastic deformation at the interface of the two projectiles. Posttest recovery examination of projectiles, including metallographic examination of any internal shear banding or tensile failure, completes the data. The experiment is then computationally simulated in iterative calculations with a two-dimensional computer code. The dynamic yield surface parameters are varied until the experimental and computational "mushrooming" agree.

The symmetric Taylor test has two advantages over the classical Taylor test. The first is the elimination of possible computer simulation problems regarding the movement of the cylinder-target interface and any possible yielding or failure in the actually nonrigid target. The second advantage is the elimination of the uncertainty of whether the projectile sticks to or slides freely along the target interface, a problem that again leads to computational uncertainties. In the symmetric Taylor test, the interface between the two cylinders does not move axially in the center-of-mass coordinate system, and the two cylinders stick precisely together as their interface expands rapidly outward. We note that to attain the same impact conditions in the symmetric Taylor test must be approximately twice as high as that in the classical version. However, this is not a problem for the metals of interest in this program.



MA-6276-15A

FIGURE 17 SCHEMATIC DIAGRAM OF SYMMETRIC TAYLOR TEST

To date, we have performed two symmetric Taylor tests to test the experimental procedure. Figure 18 shows the framing camera records and the recovered specimens from a test with aluminum rods. The experimental parameters were chosen to closely simulate a classical Taylor test performed by Wilkins et al.²¹ on the same material. After the test the rods were recovered, sectioned, and examined to see if the mushrooming was due completely to homogeneous plastic flow, as desired, or whether heterogeneous failure mechanisms had been active. Figure 19 shows that, for this experiment, the permanent deformation was due entirely to homogeneous plastic flow, as expected from Wilkins's work.

In future work this technique will be applied to RHA and DU rods. In preparation for the analysis, Brian Scott of BRL plans to test our procedure for obtaining the dynamic yield function by running HEMP computer simulations of the above aluminum rod impact experiment and comparing the results with the framing camera data.

3. Smooth Round Bar Tension Tests

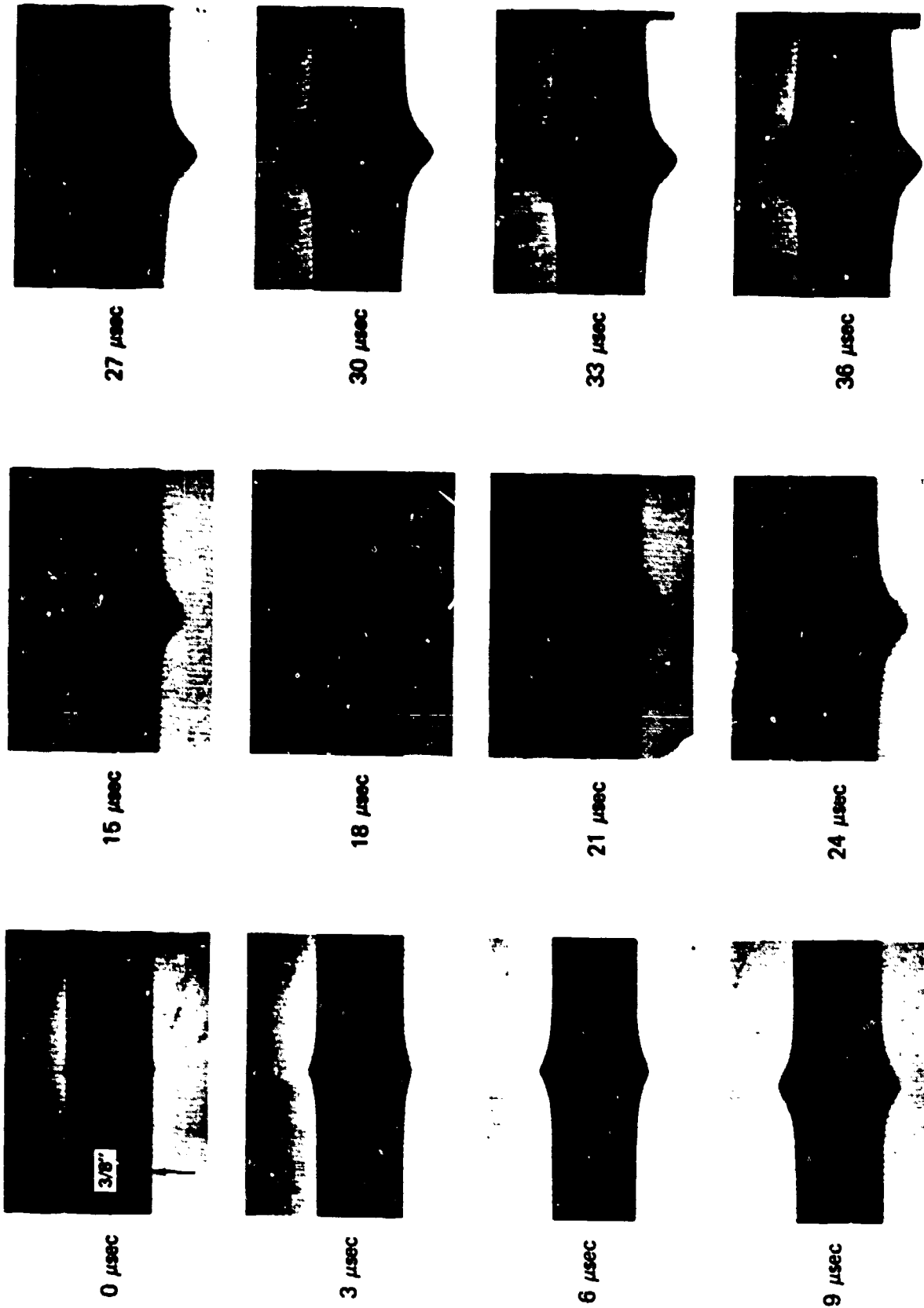
The smooth round bar tension tests on RHA material were discussed earlier in Section IIA in connection with the microstructural tensile failure mechanism, namely, anisotropic nucleation of voids at MnS inclusions, followed by growth and coalescence to cause fracture. These tests also give us the quasi-static yield function to use as a starting point for the iterative calculations of the symmetric Taylor tests for evaluation of the dynamic yield function.

Similar round bar tension tests of DU material may be performed in the future if available data are found to be ambiguous.

4. Plate Impact Tests

Plate impact tests designed to produce short-lived tensile pulses in the target material under conditions of uniaxial strain are useful for studying dynamic tensile failure phenomenology.²³

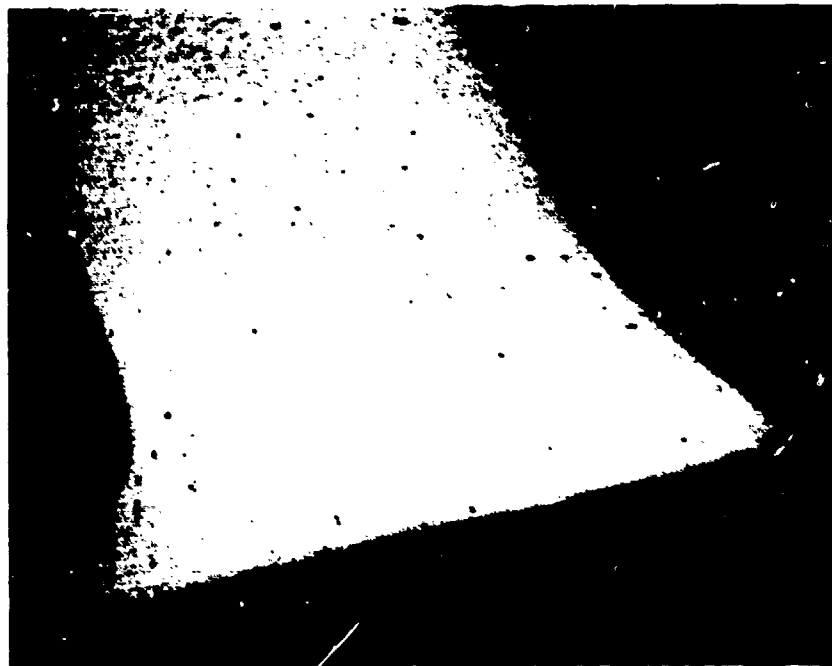
Dr. Gerald Moss has performed a series of such experiments at BRL with tungsten alloy²⁴ and RHA material,²⁵ and he is designing similar



MP-7893-64

FIGURE 18 FRAMING CAMERA RECORDS OF MUSHROOMING ALUMINUM RODS IN SYMMETRIC TAYLOR TEST

Times are after impact.



1 cm

MP-314542-126

FIGURE 19 PHOTOGRAPHS OF RECOVERED ALUMINUM ROD SHOWING THAT THE PERMANENT DEFORMATION WAS DUE ENTIRELY TO HOMOGENEOUS PLASTIC FLOW

experiments with DU to be performed if the phenomenology experiments reveal ductile void growth to be an important failure mechanism for the DU penetrators.

The results from these experiments will be analyzed to provide input to the NAG model for dynamic ductile void growth.

III ANALYSIS

A. Computational Model Adaptation

The computational material model used in the armor penetration simulations must have the potential to describe elastic-plastic deformation, quasi static and dynamic tensile fracture, and adiabatic shear banding. In the following paragraphs we describe these portions of the model.

1. Elastic-Plastic Model

The elastic-plastic model we are now using applies a von Mises yield function with linear work hardening. Nonlinear work-hardening rate-dependent models are available if needed. No new development of elastic-plastic models was undertaken during this program; instead, we have applied these models currently available in our wave propagation computer codes.

2. Ductile Fracture Model for Intermediate Strain Rates

During projectile penetration, fracture can occur at several positions along the penetrator axis and on the back surface of the target. In all cases the fracture probably occurs in 10 to 100 μ sec. For usual penetrator and target materials, the fracture occurs by a ductile mode and is initiated by the growth of voids, although brittle fracture may also occur. We have begun to develop a ductile fracture model that will permit detailed simulation of these damage processes. The model includes:

- Nucleation or activation of new voids either as a function of stress and time (as in DFRACT²⁶) or as a function of plastic strain (as in DFRACTS²⁷).
- Elastic void expansion and contraction, as outlined by Seaman et al.²⁸

- Void compaction under compression, as described by Seaman et al.²⁸
- A static fracture threshold as described by Gurson.²⁹

With these features, the model can simulate static and dynamic ductile fracture over the complete range of strain rates considered in this study.

The major effort was devoted to the static fracture threshold, which was the most difficult factor to incorporate. The threshold problem is discussed below, and an outline is presented of a technique for combining the four items listed above into a single model.

To resolve the threshold problem, we used a simplified form of Gurson's model²⁹. Gurson treated a sphere of rigid-plastic material containing a spherical void. As the tensile stress state was increased, regions of plastic deformation formed around the void. The void growth threshold was reached when the plastic zones had extended to the point that void expansion could occur without resistance by the remaining rigid material. Stress states from pure shear to uniform tension (hydrostatic) were examined. The threshold stress function was written as a yield curve ϕ , where

$$\phi = \frac{\bar{\sigma}^2}{Y^2} + 2f \cosh\left(\frac{3P}{2Y}\right) - 1 - f^2 = 0 \quad (\text{III-1})$$

where $\bar{\sigma}^2 = \frac{3}{2} \sigma'_{ij} \sigma'_{ij}$

$$= \frac{3}{2} \left(\sigma'^2_{xx} + \sigma'^2_{yy} + \sigma'^2_{zz} \right) + 3 \left(\sigma'^2_{yz} + \sigma'^2_{zx} + \sigma'^2_{xy} \right) \quad \text{in which}$$

$\sigma'_{ij}, \sigma'_{ij}$ = stress and deviator stress in the i direction on a plane normal to the j direction

Y = yield strength

f = void volume fraction

$$P = \frac{1}{3} \sigma_{ii} = \frac{1}{3} \left(\sigma_{xx} + \sigma_{yy} + \sigma_{zz} \right) = \text{average stress.}$$

Gurson also shows that a normality flow rule describes the stress-strain relations for the material in the yielding range. The normality rule is a condition between the stresses σ_{ij} (average values over the boundary of the sphere of material) on the yield curve and the average plastic strains ϵ_{ij}^P throughout the sphere.

$$\int d\sigma_{ij} d\epsilon_{ij}^P = 0 \quad (\text{III-2})$$

This normality flow rule is commonly used in some form in plasticity problems.

In our use of Gurson's model, we simplified the yield function to the ellipse as follows:

$$\frac{\bar{\sigma}^2}{Y^2(1-f)^2} + \frac{9 P^2}{4Y^2(\ln f)^2} = 1 \quad (\text{III-3})$$

This ellipse has the correct intercepts and normality properties at the intercepts.

The requirements of the normality rule for an isotropic material governed only by the invariants $\bar{\sigma}$ and P lead to a relation between the plastic strains. The ratio S of the stress invariant increments dP^P and $d\bar{\sigma}^P$ corresponding to these plastic strain increments is

$$S = \frac{d\bar{\sigma}^P}{dP^P} = \frac{\bar{\sigma}^N - \bar{\sigma}}{P^N - P} = \frac{G}{\sqrt{3} K} \frac{\partial \phi}{\partial \bar{\sigma}} \quad (\text{III-4})$$

where ϕ is the yield function, G and K are the shear and bulk moduli, respectively, $\bar{\sigma}^N$ and P^N are invariants computed from the total strain increments, and $\bar{\sigma}$ and P are computed from the elastic components of the strain increments. The usual normal to the yield function ϕ has the slope

$$S_c = \frac{\partial \phi}{\partial \bar{\sigma}} \quad (\text{III-5})$$

By comparing Eqs. (III-4) and (III-5), we see that the slope corresponding to the normality rule is proportional to the normal slope of the yield curve. With the normality rule for the plastic stress-strain relations, a solution procedure for stresses under incremental strain loading can be formulated.

The solution procedure for stress caused by any strain increment is developed by first assembling the conditions that must be met. These are reduced to a single implicit equation for pressure. The solution is then obtained by a regula falsi technique. The four conditions that must be satisfied simultaneously are:

- (1) The plastic strains in the strain interval must be normal to the mean point on the yield surface during the interval.
- (2) The stress point must be on the yield surface.
- (3) The void volume is determined by the pressure and internal energy in the solid material.
- (4) The yield stress is determined by the cumulative plastic strain.

These four requirements determine $\bar{\sigma}$, P , f , and Y . Below, each requirement is derived in analytical form and then combined to form a single equation for pressure P .

The normality condition outlined above leads to a relation between the plastic components of $\bar{\sigma}$ and P and the stress normals S_0 and S_1 at the initial and final states of the interval.

$$\frac{\Delta\bar{\sigma}^P}{\Delta P^P} = \frac{\bar{\sigma}^N - \bar{\sigma}}{P^N - P} = \frac{S_0 + S_1}{2} \quad (\text{III-6})$$

where $\Delta\bar{\sigma}^P$ and ΔP^P are plastic components of $\bar{\sigma}^N$ and P^N . Expressions for S_0 and S_1 are obtained from Eq. (III-4) and the function ϕ in Eq. (III-3)

$$S = \frac{G}{\sqrt{3} K} \frac{4\bar{\sigma}(\ln f)^2}{9P(1-f)^2} \quad (\text{III-7})$$

When Eq. (III-7) is inserted into Eq. (III-6) and that equation is solved for $\bar{\sigma}$, the result is

$$\bar{\sigma} = AP \left[\frac{1 + BP}{1 + CP} \right] \quad (\text{III-8})$$

where

$$A = \frac{9\sqrt{3}(1-f)^2 K_1 \bar{\sigma}^N}{2(\ln f)^2 G_1 P^N} - \left(\frac{\ln f_0}{\ln f} \right)^2 \left(\frac{1-f}{1-f_0} \right)^2 \frac{G_0 K_1}{G_1 K_0} \cdot \frac{\bar{\sigma}_0}{P_0}$$

$$\frac{1}{B} = \frac{9\sqrt{3} P_0 (1-f_0)^2 K_0 \bar{\sigma}_0^N}{2\bar{\sigma}_0 (\ln f_0)^2 G_0} - P^N$$

$$C = \frac{9\sqrt{3}(1-f)^2 K_1}{2(\ln f)^2 G_1 P^N} - \frac{1}{P^N}$$

Here it is noted that B is a known value, but A and C are functions of f, the void fraction.

The work-hardening relation used is the linear form

$$Y = Y_0 + Y_n \cdot \Delta \bar{\epsilon}^P \quad (\text{III-9})$$

where Y_n is a work-hardening modulus, and $\Delta \bar{\epsilon}^P$ is an increment of plastic strain.

The void volume V_v is computed for the current stress state by first determining the solid volume $V_s = V - V_v$. The solid volume is related to the solid pressure P_s by the Mie-Grüneisen relation

$$P_s = K_s \left(\frac{\rho_s}{\rho_0} - 1 \right) + \Gamma \rho_0 E \quad (\text{III-10})$$

where K_s is the bulk modulus of the solid material; ρ_s and ρ_0 are the solid and initial densities, respectively; Γ is Grüneisen's ratio; and

E is internal energy. According to Carroll and Holt³⁰, the average pressure P on the cross section is reduced from P_S by the ratio of gross to solid density

$$P = \frac{\rho}{\rho_S} P_S \quad (\text{III-11})$$

Solving Eqs. (III-10) and (III-11) for V_S = 1/ρ_S, we obtain

$$V_S = \frac{1 - PV\rho_o/K_S}{\rho_o - \Gamma\rho_o^2 E/K_S} \quad (\text{III-12})$$

The void fraction is then

$$f = \frac{V_v}{V} = 1 - \frac{V_S}{V} = 1 - \frac{\rho - P\rho_o/K_S}{\rho_o - \Gamma\rho_o^2 E/K_S} \quad (\text{III-13})$$

This expression for void fraction naturally accounts for elastic and thermal expansions of the void because both effects are present in the solid volume calculation.

The expression for pressure P can now be written by substituting $\bar{\sigma}$ from Eq. (III-8) into Eq. (III-3). The result is

$$P = \frac{\pm Y}{\sqrt{\frac{A^2(1 + BP)^2}{(1 - f)^2(1 + CP)^2} + \frac{9}{4(\ln f)^2}}} \quad (\text{III-14})$$

where Y and f are obtained from the associated Eqs. (III-9) and (III-13), and the value of P in the radical is from a previous estimate.

The solution procedure then has the following steps:

- (1) Estimate an initial pressure P_a.
- (2) Compute the void fraction f from Eq. (III-13).
- (3) Compute A, B, and C.

- (4) Compute pressure P from Eq. (III-14).
- (5) Reestimate P_a and return to step 2 if P and P_a are not sufficiently close.

If ongoing phenomenology experiments indicate quasi-static void growth to be an important damage mode, we will then incorporate this ductile fracture model into a computer subroutine during the next year.

3. Fracture Models for High Strain Rates

In previous work,²³ dynamic fracture models were developed that describe the nucleation, growth, and coalescence of statistical numbers of brittle cleavage cracks or ductile plastically growing voids. In this program we have not developed these models further, but will adapt them in their current form by calibrating them with the data obtained from the BRL plate impact requirements.

4. Adiabatic Shear Banding Model

As discussed above, the phenomenology experiments performed to date indicate that adiabatic shear banding is the single most important microstructural damage mechanism for long rod penetration because it governs both the erosion of the penetrator nose and the plugging of the target. Therefore, we have devoted a large effort to further developing and calibrating our previous shear band model.¹⁸ The previous shear band model subroutine, discussed in Reference 18, is named SHEAR2, whereas the new, upgraded subroutine is named SHEAR3.

The following changes were made to convert SHEAR2 to SHEAR3:

- The shear band size distributions were changed from a series of discrete points to an analytical form (see Reference 27 and Appendix A).
- The stress relaxation associated with damage was completely rederived (see Reference 4 and Appendix A).
- The nucleation and growth laws were generalized to allow more strain rate dependence (see Reference 11 and Section III-B).

- The number of special variables per cell required by the subroutine was reduced (see Reference 11 and Appendix A).
- The threshold conditions for initiation of shear band activity were derived from plastic instability theory and a simple formula was derived for predicting the critical strain for shear banding.

The above changes are described in some detail in Appendices A and B. Appendix A describes the SHEAR3 subroutine and Appendix B describes the derivation of the threshold conditions for onset of shear banding.

A key result discussed in Appendix B is the critical strain for onset of adiabatic shear banding, as given by a formula of the form

$$\bar{\epsilon}^P = \left(\frac{n E_m}{\rho \alpha \tau_0} \right)^{\frac{1}{n+1}}, \quad (\text{III-15})$$

where $\bar{\epsilon}^P$ is the critical equivalent plastic strain; and n is the hardening exponent in a hardening law of the form

$$\tau = \tau_0 (\bar{\epsilon}^P)^n, \quad (\text{III-16})$$

where τ is the effective shear yielding stress; E_m is the specific melt energy; ρ is the density; and α is a linear thermal softening coefficient from the relation

$$\tau = 1 - \frac{\alpha W}{E_m} \tau_0 (\bar{\epsilon}^P)^n, \quad (\text{III-17})$$

where W is the specific plastic strain energy density.

The Eq. (III-15) clearly shows the competitive effects of strain hardening and thermal softening, and expresses the criterion that the shear banding will begin as a plastic instability when the global thermal softening caused by adiabatic plastic deformation overwhelms the global work hardening. Appendix B also gives a formula for more complicated thermal softening behavior. Finally, Appendix B compares predicted critical strains for onset of shear banding for several metals with observations, and shows that the correct ranking is predicted.

B. Generation and Testing of Shear Banding Model Parameters

The material parameters for the shear banding model, SHEAR3, are generated at present almost entirely from contained fragmenting cylinder (CFC) data. In the current stage of the program, we have data bases for two materials, 4340 steel and RHA steel. CFC data for DU will be generated in future work. By far the most extensive data base is that for 4340 steel of three hardnesses; these data were generated by SRI in a previous program for AMMRC³¹. In the following paragraphs we describe the current state of analysis of the data for both 4340 and RHA steel.

1. Analysis of 4340 Data

Extensive shear banding data were available from six contained-fragmenting-cylinder experiments on 4340 steel hardened to R_c 40. We have taken several steps to use 4340 data to aid in the development and verification of the shear band model. In Reference 7 we made a first attempt to deduce initiation, nucleation, and growth descriptions for the shear bands. In that effort we assumed that the shear band nucleation and growth rates should correlate with strain rate histories that peaked about 20 μ sec. after detonation. However, later examination of our computational simulations showed that the deduced threshold strains of about 0.2 were not reached until later, when the strain rate was significantly lower. Therefore, we next reduced the shear band data to a form where nucleation and growth processes could be more clearly identified and quantified. The shear band model was then modified to account for these observed processes. The detonation process in TROTT³², the two-dimensional wave propagation code used for the fragmenting-round simulations, has also been modified to better represent the explosion in low-density PETN. To avoid tangling of the computational cells in the numerical representation of the explosive, an automatic rezoner has been written and debugged. The shear band data reduction, shear band model changes, and the detonation algorithm are described here. The rezone method will be described later after we have gained more experience in using it.

The 4340 data were obtained by counting and measuring the shear bands observed on the surfaces of six cylinders after contained-fragmenting-round experiments. The experimental configuration is shown in Figure 20. The buffer thickness and the density of the explosive were varied to provide a range of strain rates, peak strains, and levels of shear banding.

Following counting of the shear bands, the cumulative numbers were plotted in graphs like Figure 21. Then each distribution was fitted to the exponential relation

$$N_g = N_0 \exp(-R/R_1) \quad (\text{III-18})$$

where N_g is the cumulative number of bands/cm² with a radius greater than R

N_0 is the total number of bands/cm²

R_1 is a size parameter for the distribution.

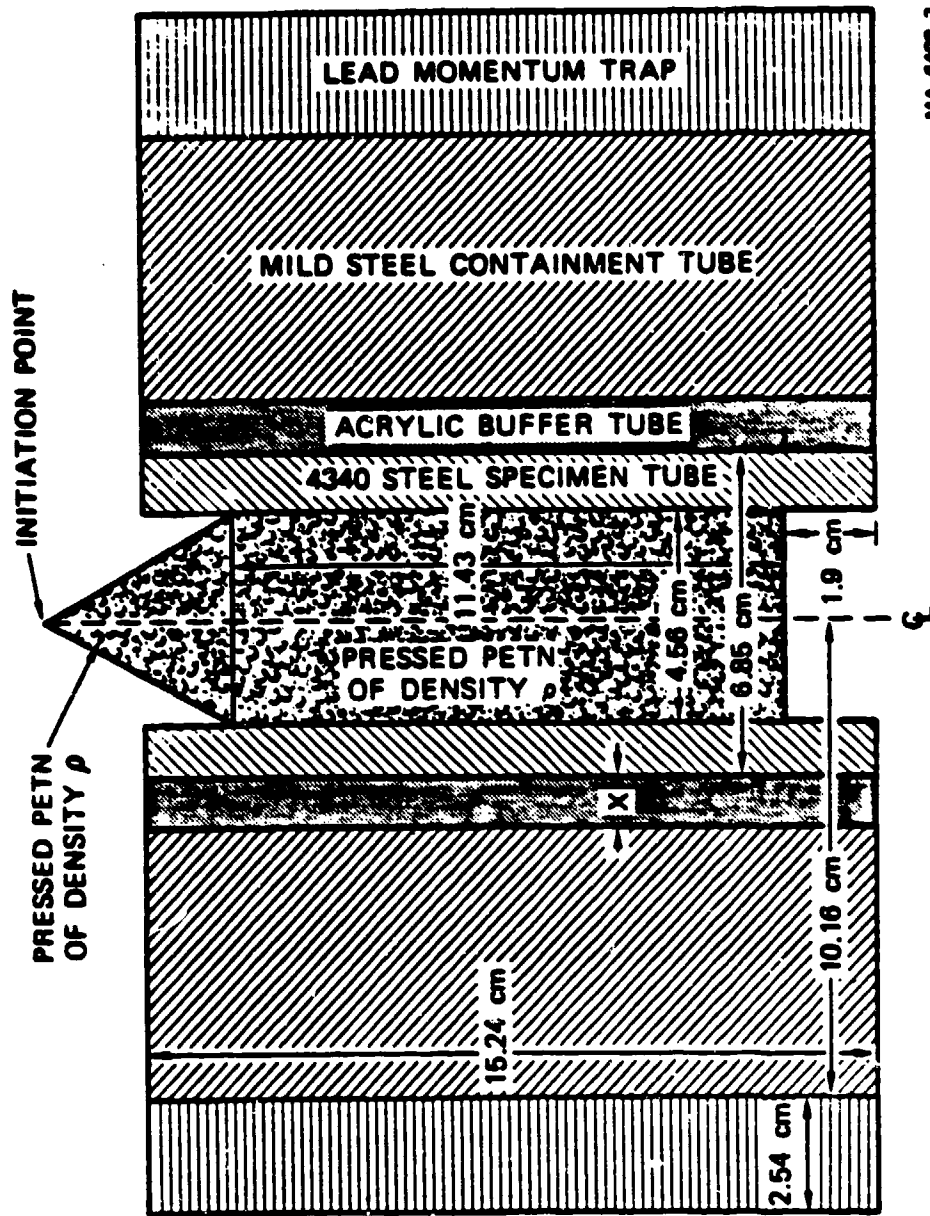
With the distributions reduced to two characterizing parameters, N_0 and R_1 , plots can be made to study the initiation, nucleation rate, and growth rate of the bands.

The initiation and nucleation rate of shear bands was examined by plotting N_0 as a function of plastic strain for all the cylinders, as shown in Figure 22. The plastic strain was obtained by measuring the thickness change in the cylinders or large fragments after the test. As derived in Reference 33, equivalent strain is

$$\bar{\epsilon}^P = \frac{2}{3} \epsilon_{1j}^P \epsilon_{1j}^P = \sqrt{\frac{2}{3} [(\epsilon_r^P)^2 + (\epsilon_\theta^P)^2 + (\epsilon_z^P)^2]} \quad (\text{III-19})$$

where ϵ_r , ϵ_θ , ϵ_z are strains in the radial, circumferential, and axial directions, respectively. For the calculations, we assume that the axial and volumetric plastic strains are zero, so that

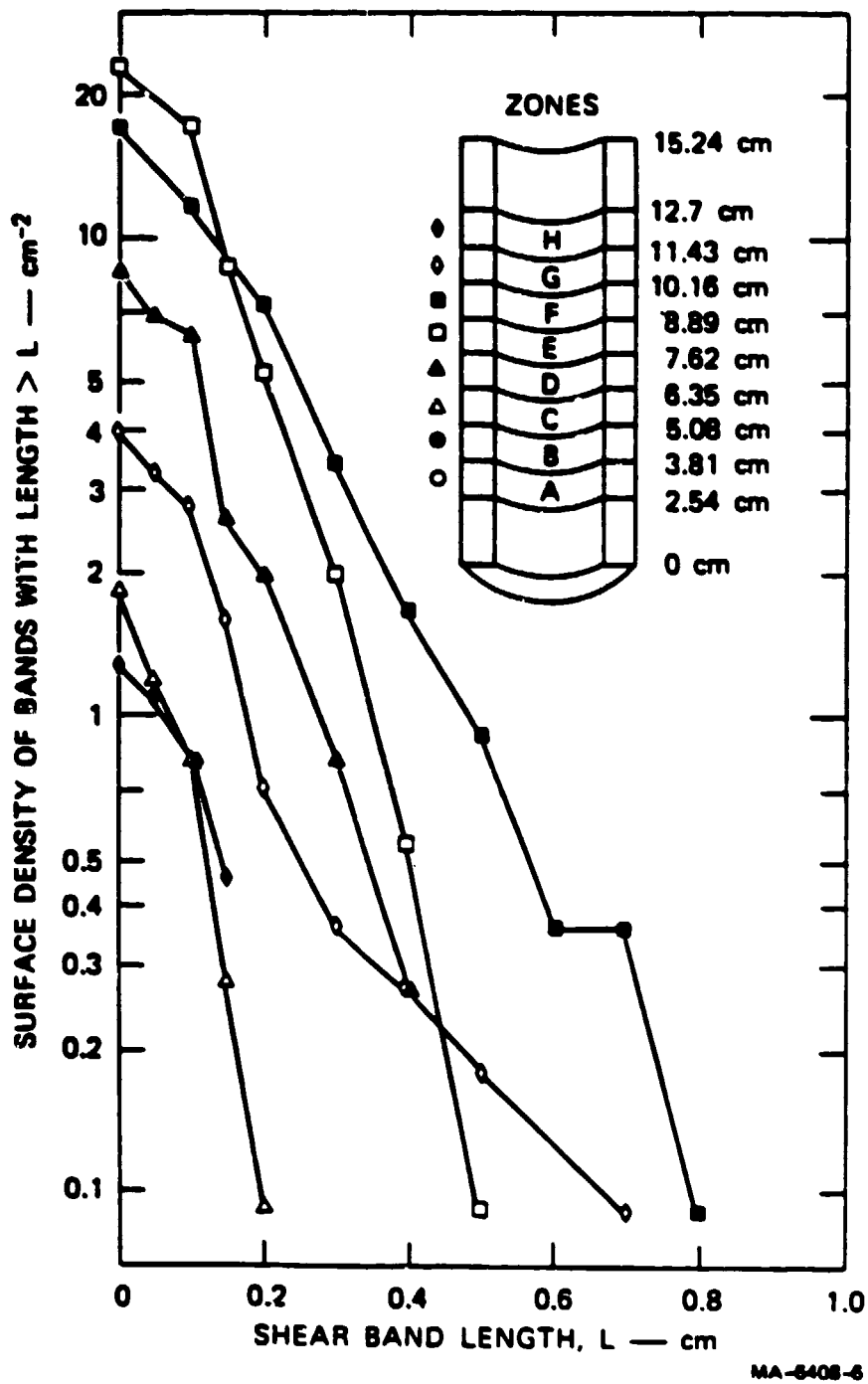
$$\epsilon_r^P = -\epsilon_\theta^P$$



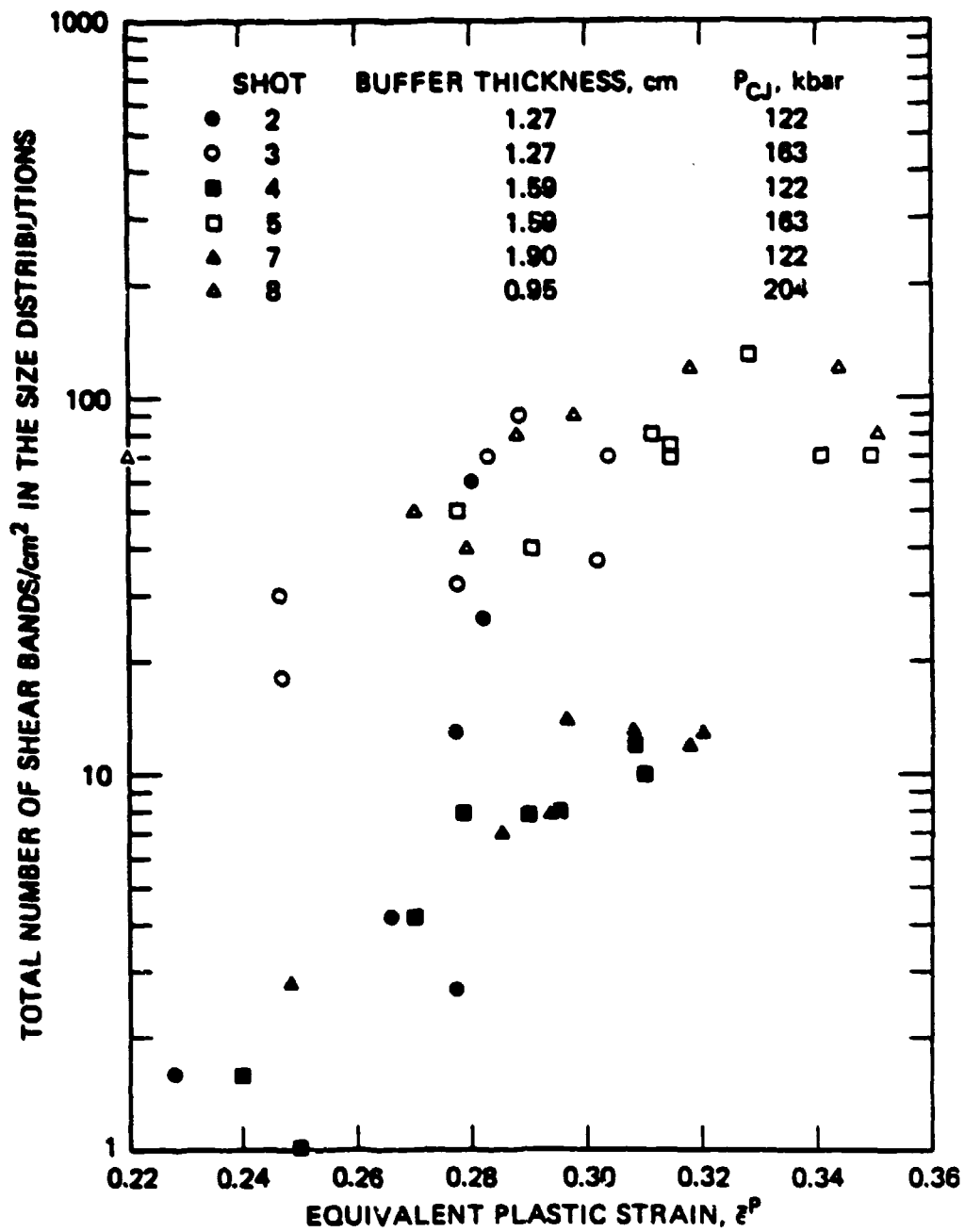
MA-6408-3

FIGURE 20 CROSS SECTION OF CONTAINED-FRAGMENTING-CYLINDER EXPERIMENTS

Buffer thickness X varies from 0.95 to 1.9 cm, PETN density ρ varies from 1.20 cm to 1.47 g/cm³.



**FIGURE 21 SHEAR BAND DISTRIBUTION FOR SHOT 2
IN 4340 STEEL, R_c 40**



MA-7893-61

FIGURE 22 MEASURED NUMBERS OF SHEAR BANDS/cm² VERSUS PLASTIC STRAIN BASED ON WALL THICKNESS MEASUREMENTS FOR SIX CONTAINED-FRAGMENTING-CYLINDER EXPERIMENTS IN 4340 STEEL, R_c 40

Then

$$\bar{\epsilon}^P = \sqrt{\frac{4}{3}} |\epsilon_r^P|$$

For a change in thickness from a_o to a_f , the average radial strain is

$$\epsilon_r = \int_{a_o}^{a_f} \frac{da}{a} = \ln\left(\frac{a_f}{a_o}\right) \quad (\text{III-20})$$

and

$$\bar{\epsilon}^P = \pm \sqrt{\frac{4}{3}} \ln\left(\frac{a_f}{a_o}\right) \quad (\text{III-21})$$

By its definition from the thickness change, $\bar{\epsilon}^P$ represents the plastic strain taken homogeneously by the material and not the strain that has been taken by the shear bands.

An alternative derivation of $\bar{\epsilon}^P$ can be made based on the circumferential strain

$$\epsilon_\theta = \int_{r_o}^{r_f} \frac{dr}{r} = \ln\left(\frac{r_f}{r_o}\right) \quad (\text{III-22})$$

where r_o and r_f are initial and final radii at some point in the cylinder. Let \bar{r} be the average radius of the cylinder. Then the average circumferential strain is

$$\epsilon_\theta = \ln\left(\frac{\bar{r}_f}{\bar{r}_o}\right) \quad (\text{III-23})$$

and

$$\bar{\epsilon}^P = \pm \sqrt{\frac{4}{3}} \ln \left(\frac{\bar{r}_f}{\bar{r}_o} \right) \quad (\text{III-24})$$

Because this strain is based on the motion of the external and internal surfaces, it should represent the total strain imposed by the explosive and not merely the strain taken homogeneously. Values of this second definition of $\bar{\epsilon}^P$ were calculated in a few cases and compared with the result obtained from Eq. (III-21). The radius-based strain always exceeded the thickness-based value by 5% or 10%. For the cylinders with such heavy damage that fragments are formed, the radius-based strain cannot be obtained reliably, so the imposed strain is not known. Therefore, the thickness-based strain was used in the plots as a rough measure of the imposed strain.

The cumulative numbers of shear bands in Figure 22 indicate an indication threshold in the vicinity of 22% plastic strain, in agreement with that predicted from the plastic instability theory discussed above as well as in Reference 7 and Appendix B. After the initiation threshold is exceeded, the shear bands nucleate gradually as a function of the increasing plastic strain. The numbers appear to fall into separate groups according to the explosive pressure P_{CJ} indicated in the figure. The higher pressures also induce a higher strain rate, so the nucleation rate may be a function of a power of the strain rate. The large numbers at low strains for the higher pressure tests may indicate that most of the imposed strain above 22% went into shear banding rather than into homogeneous plastic flow. Thus a nucleation process of the following form is indicated

$$\begin{aligned} \frac{dN}{dt} &= 0 & \bar{\epsilon}^P &< 0.22 & (\text{III-25}) \\ &= A_N \left(\frac{d\epsilon}{dt} \right)^n & \bar{\epsilon}^P &> 0.22 \end{aligned}$$

where A_N is a material constant related to yield strength and inclusion

counts. With $n = 3$ this expression for nucleation rate agrees with that used in our earlier work,^{18, 31} for which the corresponding expression for nucleation in a particular plane, where orientation is given by the subscripts ϕ, θ , is

$$\frac{dN_{\phi\theta}}{dt} = C_n F_n \left(\frac{1}{E_{cr}} \frac{dE^P}{dt} \right)^2 \cdot \frac{d\epsilon_{\phi\theta}^{ps}}{dt}$$

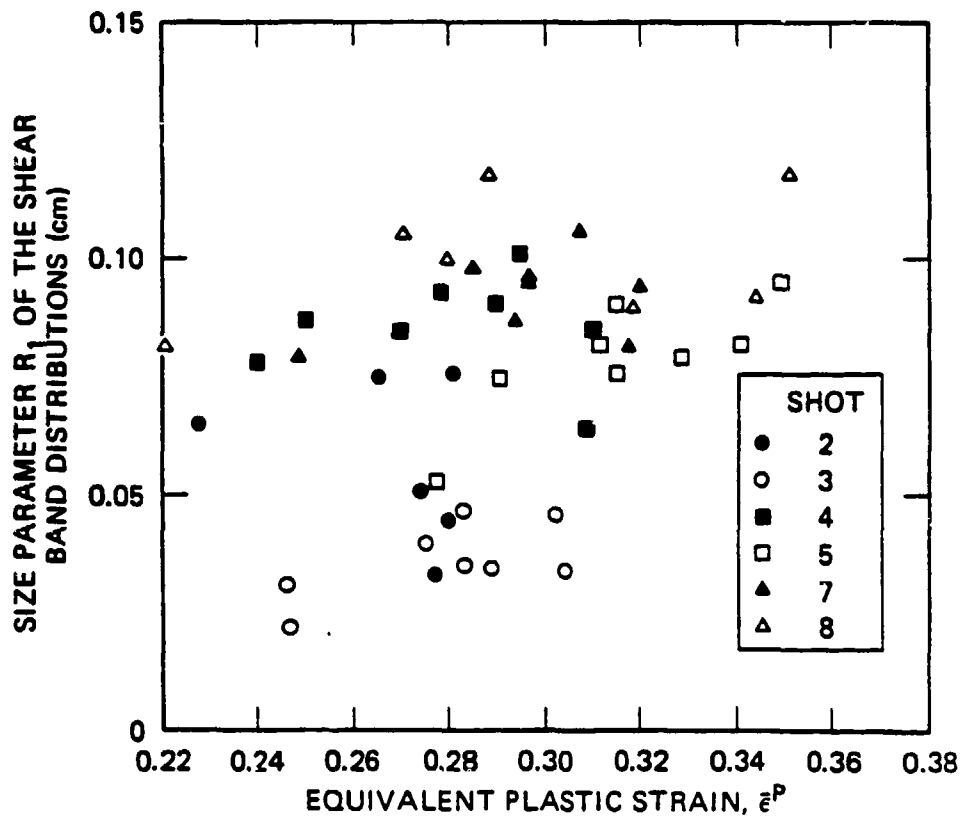
Here E_{cr} is a critical energy, taken to be the melt energy; dE^P/dt is the rate of increase of plastic strain energy; $N_{\phi\theta}$ is the number of shear bands per unit volume with an orientation given by the spherical coordinates ϕ and θ ; and $\epsilon_{\phi\theta}^{ps}$ is the plastic shear strain in the same direction. C_n is a coefficient with the units of time squared, and F_n is a factor representing the fraction of solid angle assigned to the $\phi\theta$ orientation. The factor dE^P/dt is proportional to the product of the shear strain rate and the yield strength; hence, the nucleation rate is proportional to the cube of the strain rate in SHEAR2, the earlier version of our shear banding model.

The shear band growth process is studied by plotting R_1 as a function of $\bar{\epsilon}^P$, as in Figure 23. For the 4340 data, this graph shows some grouping of R_1 values for individual shots, but no overall trends. The initiation size may be about $R_1 = 0.02$ cm. The total growth produces about a five-fold increase in the size. Without a clear indication from the data, a viscous growth law will be assumed

$$\frac{dR}{dt} = C_G \frac{d\epsilon}{dt} R \quad (III-26)$$

This growth law preserves the exponential form of the distribution with increasing strain.

The increase of damage with plastic strain can also be studied by plotting the total shear band area as a function of the strain. The



MA-7893-63A

FIGURE 23 SIZE PARAMETER R₁ FROM MEASURED SHEAR BAND SIZE DISTRIBUTIONS VERSUS PLASTIC STRAIN BASED ON WALL THICKNESS MEASUREMENTS FOR SIX CONTAINED-FRAGMENTING-CYLINDER EXPERIMENTS IN 4340 STEEL, R_c 40

total area, a measure of the damage, is

$$D = \int_0^{\infty} \pi R^2 dN = 2\pi N_0 R_1^2 \quad (\text{III-27})$$

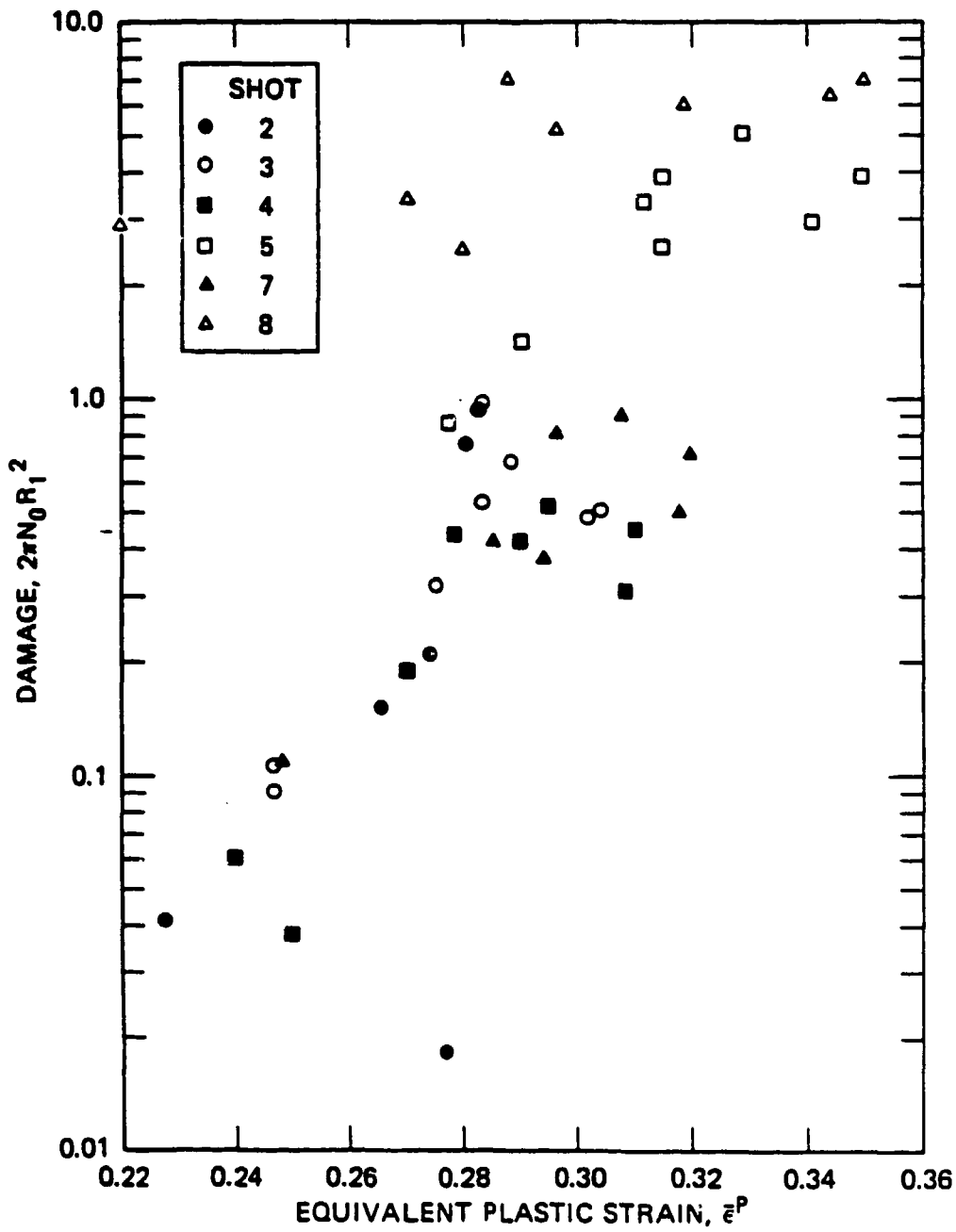
for the exponential distribution in Eq. (III-18). The damage D , plotted in Figure 24, shows a clear trend toward increasing damage with strain, and all the shots contribute to the same trend. The scatter at the higher damage level would probably be reduced by using the imposed strain instead of the homogeneous strain.

The plots in Figures 22, 23, and 24 represent the first steps toward obtaining nucleation and growth laws and determining the material constants for these laws. The next steps are to insert these laws into SHEAR 3 and perform simulations of the experiments using these constants. These simulations are under way.

2. Explosive Pressure Computation

In some recent simulations of 4340 steel fragmenting rounds for long times (~ 100 μsec), it was found that the test cylinder expanded beyond the dimensions observed in the experiments. The calculated pressure histories in these cases were found to have a larger impulse than that expected from polytropic gas expansion calculations. Therefore, the detonation process model was reexamined. From the analytical expression for pressure of a running one-dimensional detonation, we developed an improved computational procedure for simulating a running detonation. This improved model is described in the following paragraphs.

(a) Analysis of One-Dimensional Detonation. Behind the detonation front, the explosive products (a polytropic gas) may be treated by the method of characteristics. Motion along the $C+$ charac-



MA-7893-62A

FIGURE 24 MEASURED DAMAGE VERSUS PLASTIC STRAIN BASED ON WALL THICKNESS MEASUREMENTS FOR SIX CONTAINED-FRAGMENTING-CYLINDER EXPERIMENTS IN 4340 STEEL

teristic is governed by the following equation:

$$\frac{dx}{dt} = u + C = \left(\frac{\partial x}{\partial t}\right)_h + \left(\frac{\partial x}{\partial h}\right)_t \frac{dh}{dt} \quad (\text{III-28})$$

where x and t are position and time

u is particle velocity

C is sound speed

h is Lagrangian location

Also the particle velocity is defined as

$$u = \left(\frac{\partial x}{\partial t}\right)_h$$

and the specific volume v is

$$v = v_o \left(\frac{\partial x}{\partial h}\right)_t$$

where v_o is the initial specific volume.

Replacing the definitions of u and v in Eq. (III-28), we obtain

$$\frac{dh}{dt} = \frac{v_o C}{v} \quad (\text{III-29})$$

Because C and v are constant along the $C+$ characteristic in a simple wave, Eq. (III-29) can be integrated to give the following relation for the rarefaction fan:

$$h = \frac{v_o C t}{v} \quad (\text{III-30})$$

At the front of the detonation, these relations hold:

$$v = v_{cj} = \frac{v_o \gamma}{\gamma + 1} \quad (\text{III-31})$$

$$c_{cj} = \frac{\gamma D}{\gamma + 1} \quad (\text{III-32})$$

$$\frac{dh}{dt} = D \quad (\text{III-33})$$

where v_{cj} is the specific volume at the C-J condition

γ is the polytropic gas exponent

c_{cj} is the sound speed at the C-J condition

D is the detonation velocity.

Now divide Eq. (III-31) by Dt and replace v_o/D by v_{cj}/c_{cj} using Eqs. (III-31) and (III-32). Then

$$\frac{v_{cj}}{c_{cj}} \frac{c}{v} = \frac{h}{Dt} \quad (\text{III-34})$$

Two additional facts from the theory of polytropic gases are introduced

$$Pv^\gamma = P_{cj}v_{cj}^\gamma \quad (\text{III-35})$$

$$c^2 = \gamma P v \quad (\text{III-36})$$

Combining these two equations, we can obtain

$$\frac{c^2}{c_{cj}^2} = \left(\frac{v_{cj}}{v} \right)^{\gamma-1} \quad (\text{III-37})$$

With this result in Eq. (III-31), we have

$$\frac{v_{cj}}{v} \frac{c}{c_{cj}} = \left(\frac{v_{cj}}{v} \right)^{\frac{\gamma+1}{2}} = \frac{h}{Dt} \quad (\text{III-38})$$

Eq. (III-35) can also be used to relate the pressures to v/v_{cj} . Replacing volumes with pressures in Eq. (III-38) gives

$$P = P_{cj} \left(\frac{h}{Dt} \right)^{\frac{2\gamma}{\gamma+1}} \quad (\text{III-39})$$

Equation (III-39) provides the pressure at any point in the rarefaction fan behind the detonation front. For a particle initially at a location h , the detonation arrives at $t = h/D$. The pressure history for the particle is obtained by varying t from h/D on to larger times.

(b) Computational Detonation Procedure. For a Chapman-Jouguet detonation, the pressure should follow a linear pressure-volume path up to the C-J point and then expand down the polytropic gas pressure-volume path given by Eq. (III-35). In addition, the C-J point should be reached at the time the detonation wave reaches the location. An approximate procedure for meeting these requirements is outlined below.

In the finite difference calculations, the detonation wave is presumed to arrive when

$$t = \frac{X_o - X_D}{D} \quad (\text{III-40})$$

where X_o is the initial midpoint position of the cell

X_D is the detonation point.

Hence the detonation is forced along at detonation velocity through the cells.

For each cell the pressure is computed according to

$$P = (\gamma - 1)\rho E \quad (\text{III-41})$$

where ρ is density and E is internal energy.

As the density begins to increase ahead of the detonation front, the pressure should follow the linear path

$$P = P_{cj} \frac{(v - v_o)}{v_{cj} - v_o} = \frac{P_{cj}}{\rho} \frac{(\rho_o - \rho)}{(\rho_o v_{cj} - 1)} \quad (\text{III-42})$$

To obtain this pressure in the cell, the internal energy is prescribed by combining Eqs. (III-41) and (III-42)

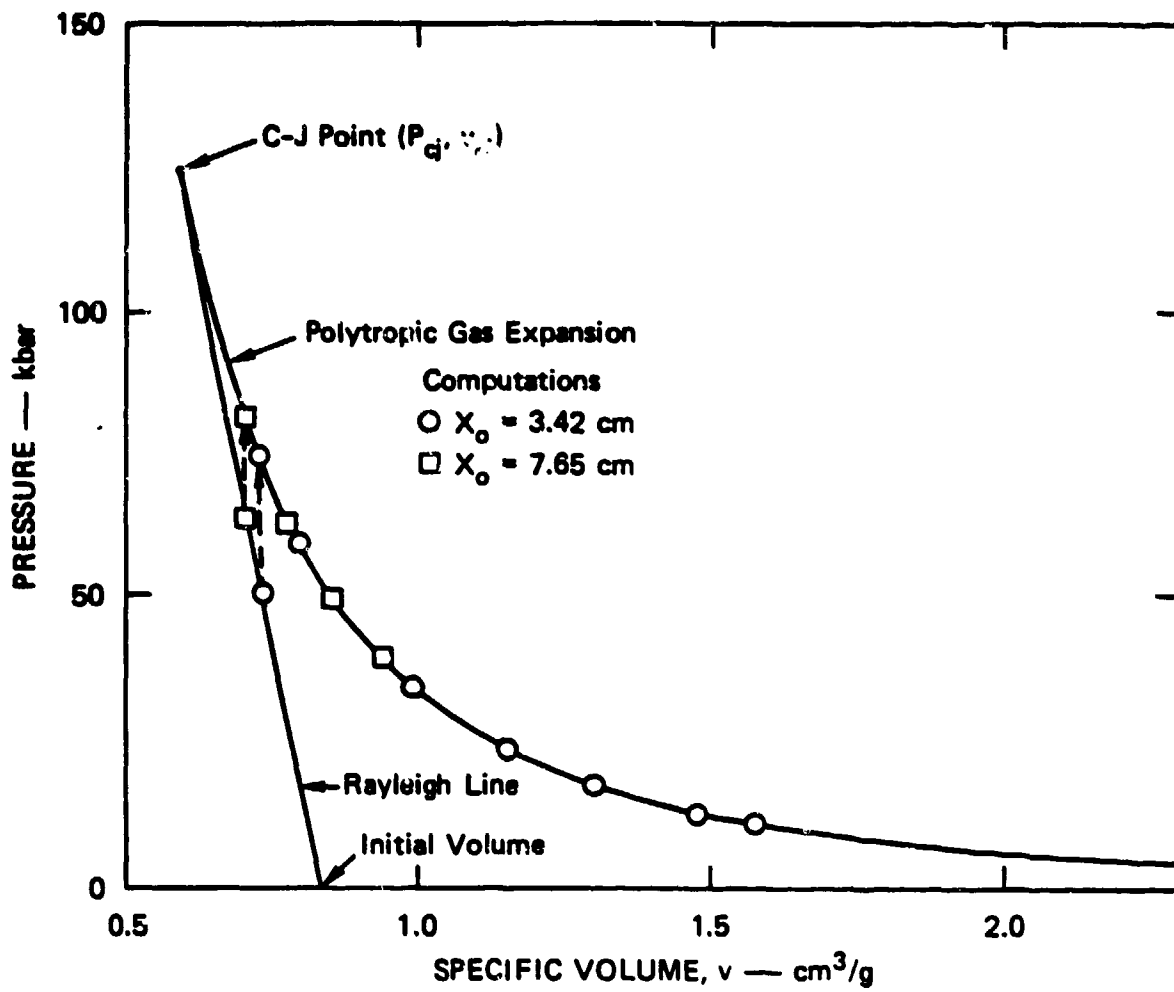
$$E = \frac{P}{(\gamma - 1)\rho} = \frac{P_{cj}(\rho_o - \rho)}{(\gamma - 1)\rho^2(\rho_o v_{cj} - 1)}$$

When the detonation front arrives [Eq. (III-40)], the internal energy is computed to put the pressure on the polytropic expansion curve according to Eq. (III-35)

$$E = \frac{P}{\rho(\gamma - 1)} = \frac{P_{cj}(\rho v_{cj})^\gamma}{\rho(\gamma - 1)} \quad (\text{III-44})$$

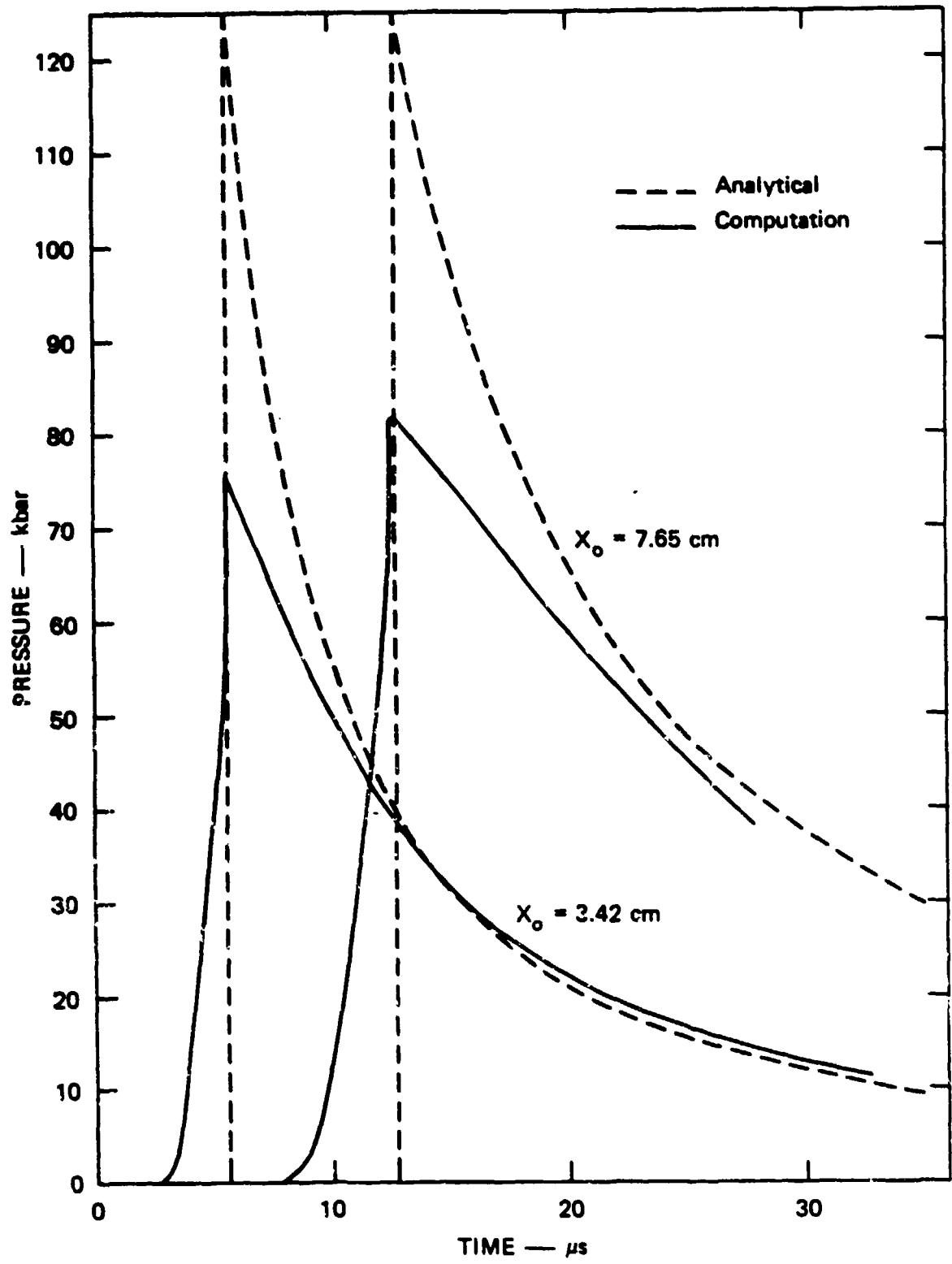
After the polytropic expansion curve is reached, the detonation process is no longer forced. The internal energy is changed according to the usual Pdv work relation and Eq. (III-41) is used to determine the pressure.

(c) Comparison of Analytical and Computational Detonation Procedures. Computations made with each of the foregoing detonation procedures were compared. Pressure-volume paths traversed by two cells (11th and 24th) in the finite difference computation are shown in Figure 25. The path is initially along the linear pressure-volume Rayleigh line. At the time of detonation, the pressure jumps up to the polytropic expansion line and then decays. Pressure histories generated at 3.42 cm (11 cells) and 7.65 cm (24 cells) into an explosive are shown in Figure 26. The analytic function shows an instantaneous pressure rise at detonation and a decay following Eq. (III-39). By contrast the finite-difference computations show a precursor, a jump in pressure



MA-7893-65

FIGURE 26 ANALYTICAL AND COMPUTATIONAL PRESSURE-VOLUME PATHS FOLLOWED IN A DETONATION PROCESS IN LOW DENSITY ($\rho = 1.2$ g/cc) PETN



MA-7893-66

FIGURE 26 COMPARISON OF ANALYTICAL AND COMPUTATIONAL PRESSURE HISTORIES IN LOW DENSITY ($\rho = 1.2$ g/cc) PETN

at the time of detonation to a pressure below P_{cj} , and a decay that approaches the analytical shape. The areas under the two curves (impulse) are approximately equal. Therefore, the finite-difference pressure history should be sufficiently accurate for determining longer time phenomena, but cannot represent the wave front accurately unless a much finer computational grid is used.

3. Analysis of RHA data

The shear band number and size data from the CFC experiments on RHA material described in Section II C have not yet been reduced, and additional CFC experiments on this material are under way. During the next year these data will be reduced and used to generate the shear banding parameters in the SHEAR3 subroutine.

C. Adaptation of HEMP code for Use with NAG Material Models

The HEMP wave propagation code will be used to simulate armor penetrations on this project. In these calculations much of the material behavior will be represented by the shear band model, SHEAR 3. Therefore, one of our tasks is to insert SHEAR 3 into HEMP and perform test calculations to verify that the insertion is correct. For the insertion, changes are required in HEMP, in SHEAR 3, and in the special material property data for SHEAR 3. In cooperation with John French of LLL, we have identified the changes needed.

The first and most serious change in HEMP is the increase in the number of variables per cell. SHEAR 3 requires 6 to 19 variables in addition to those normally stored for each cell.* Addition of more variables requires inserting a list of variables that correspond to the names used by SHEAR 3 and increasing the total number of variables, NV, allowed per cell in HEMP.

*The specific number depends on options selected by the user.

The CALL statement for SHEAR3 is inserted into the HEMP subroutine called VQP with all the other deviator stress and pressure calculations. VQP computes the strain, sound speed, and internal energy in addition to the stresses. Therefore, the second change required for the insertion of SHEAR 3 is to branch to the CALL statement after the strain calculations. Stresses will be computed in SHEAR 3 and statements will be added in VQP for special calculations of internal energy and sound speed that are consistent with the SHEAR 3 variables. The CALL statement to SHEAR 3 contains all the variables transferred between SHEAR 3 and VQP. Included are the stresses, strain increments, the variables describing shear band distributions on each plane, internal energy, yield strength, cell rotation, and a damage parameter used for triggering a slide line.

The third change is to provide for the special input of material properties required by SHEAR 3. Currently in the version of HEMP at BRL, the input deck is preprocessed by the subroutine PREHEMP, and a binary equivalent of this input deck is written. Therefore, to provide for input to SHEAR 3, we must modify the read statements in SHEAR 3 to accept this binary input. The data for SHEAR 3 will follow the normal HEMP input. The density, the shear modulus, and the bulk modulus will be included in the normal HEMP material input, and only special shear banding variables will be read by SHEAR 3.

The changes in SHEAR 3 required by the insertion also include rewriting the read statements for the material properties. To change SHEAR 3 from the dyn-sec-cm-g system of units to the Mbar- μ sec-cm-g system used in HEMP should require little recoding.

Finally, the special material property data for SHEAR 3 are being transformed to the HEMP system of units.

The above changes are currently under way. Furthermore, the changes required to insert other NAG material models such as BFRACT (dynamic brittle feature), DFRACT (dynamic ductile fracture), and DFRACTS (quasi-static ductile fracture) will be very similar to those required to insert SHEAR3. The SHEAR3 insertion is therefore being accomplished in a manner designed to make later insertion of the other subroutines as efficient as possible.

D. Computational Simulations

1. Background and Scope

The ultimate goal for this program is to be able to computationally simulate spaced armor penetration with long rods, and to be able to predict the fragment environment behind the last plate. To attain this goal will require combining adequate microstructural material failure models with state-of-the-art computer codes. It is therefore important early in the program to assess the feasibility of our approach.

The simplest possible case (but one rarely seen in practice with RHA) is normal impact with plugging of the target, such that the fragment environment behind the plate consists of a single or fragmented plug plus penetrator fragments. During this first year's effort we have performed computational simulations of this case^{9, 10} and have confirmed that it, at least, is amenable to the combined microstructural failure model/computational approach. In the following paragraphs we describe some of these calculations.

To calculate the plugging process, several factors must be modeled correctly. The first phase in the formation of the plug is the shear-band nucleation and growth. The second phase is the coalescence of the shear bands into a macroslip surface. Here it is necessary to model both the threshold conditions at which this coalescence takes place and the location of the coalesced surface. The third phase is the motion of the plug as it is pushed out of the target.

In these calculations the older SHEAR2 model was used to calculate the microdamage, since SHEAR3 was still under development.

2. Unzipping-Slide-Line Logic

The purpose of the unzipping slide line is to model the coalescence of microshear bands into a macroshear band or slide line. In the current calculations the slide line lies along a predetermined position but eventually the position of the slide line must also be determined by the microshear-band model.⁹ The strategy of the unzipping

process is to allow the microdamage to increase until a threshold level of damage is reached. When any of the computational cells around a nodal point lying on the slide line meet this criterion, the nodal point changes from a standard nodal point to a slide-line nodal point.

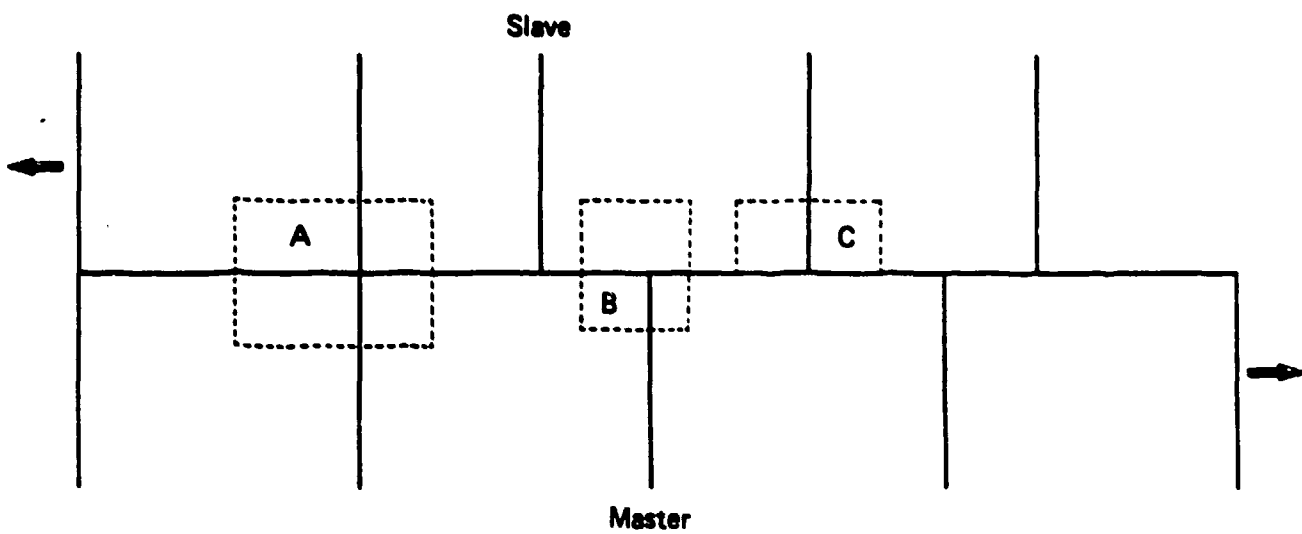
In a standard calculation, a nodal point that is not a boundary point is surrounded by four cells; A in Figure 27 is such a point. The stress in these four cells will contribute to the force acting on the nodal point. This force is then used to calculate the new accelerations, the new velocities, and the new coordinate positions.

A slide-line calculation treats nodal points differently from the standard calculation. Here we have two distinct ways of calculating the forces acting on a nodal point, depending on whether the nodal point is a master or slave.

A series of master nodal points will determine the position of the boundary, and the slave nodal points will slide along that boundary. For a master nodal point that is not a boundary point, the stresses of three cells will contribute to the force acting on the nodal point and hence determine its motion. On the other hand, the slave nodal point derives its motion from stresses in only the neighboring two cells; the position of the nodal point is then adjusted to slide along the master-defined slide line. In Figure 27, B represents a master nodal point and C represents a slave nodal point. Special consideration must be given if any of these points are either the first or last points of the slide line.

In a calculation in which the slide line is unzipped, a nodal point first must be treated as a regular nodal point--that is, as A in Figure 27. If any computed value in the neighboring cells, such as plastic strain or present shear-band damage, meets a threshold condition, the single nodal point then separates into two separate points and the forces are calculated as in B and C of Figure 27.

. At any time in the calculation, the slide line will consist of a combination of zipped and unzipped nodal points. As the calculation progresses, more nodal points are unzipped until a complete slide line is formed.



MA-7893-48

FIGURE 27 A SLIDE LINE THAT CONTAINS ZIPPED AND UNZIPPED NODAL POINTS
 The dotted rectangles represent the effective cell used for determining nodal forces.

3. Computational Setup

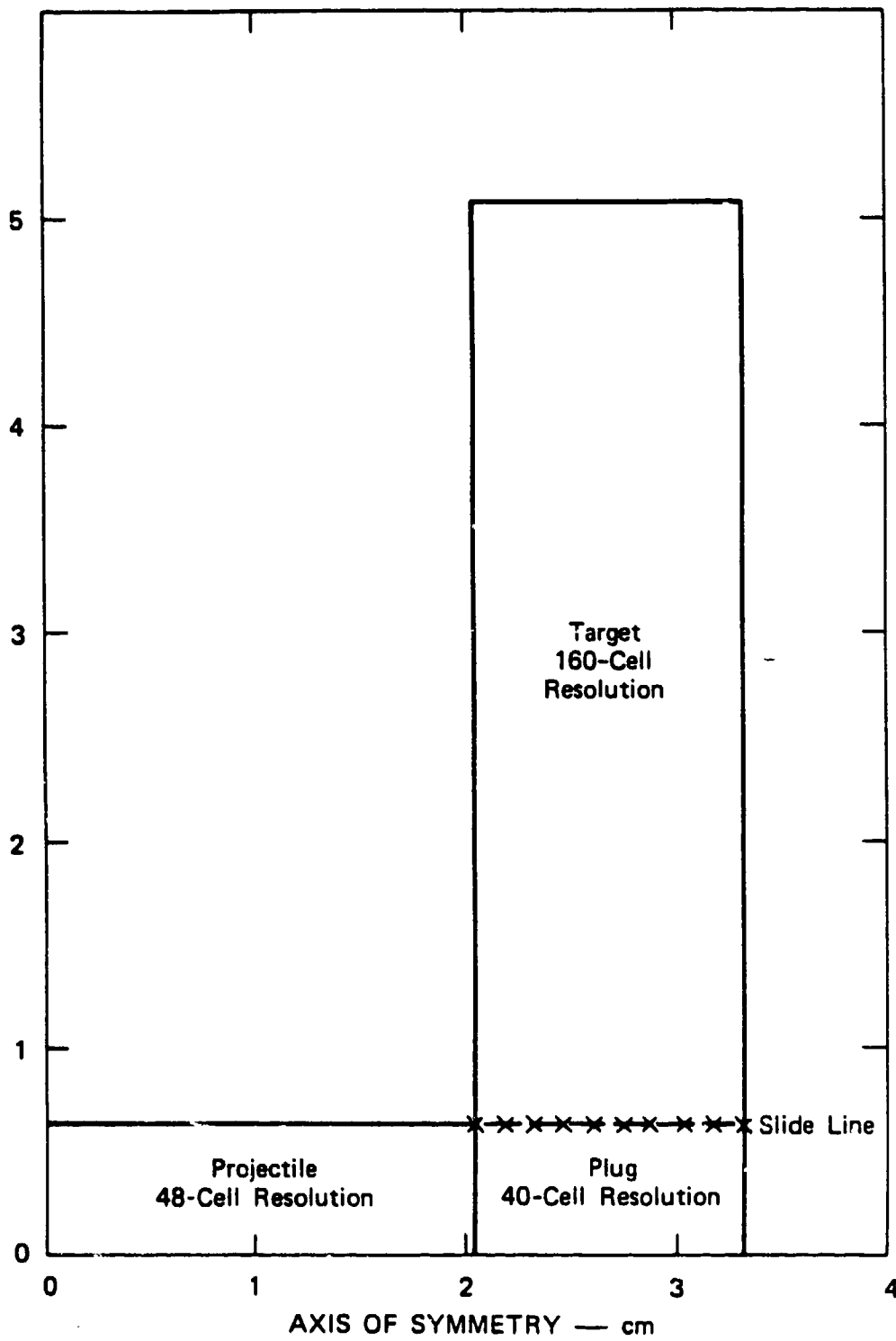
A series of computations were performed for a normal rod impact, with various treatments of the slide line. Figure 28 shows the computational layout for a 1.27-cm-thick 4340 steel target impacted by a 4340 steel rod 1.03 cm in diameter and 2.06 cm long. In all the calculations, the impact velocity was 750 m/sec, which experiments indicated was near the ballistic limit.

Figure 29 shows a cross section of the target from such an experiment (impact velocity = 790 m/sec). It is clear that the shear bands forming the plug occur near the rod edges at impact, thus making the assumed position of the incipient slide line shown in Figure 28 appropriate.

In these calculations, we computed shear strains in six orientations. Three of the orientations are for band planes normal to the following directions: (1) axial, (2) radial, and (3) circumferential. The other three orientations are for band planes that are at 45° between the following directions: (4) axial and radial, (5) axial and circumferential, and (6) circumferential and radial. Only the first, second, fourth, and fifth orientations were expected to be important in this case; therefore, we calculated the shear-band distributions only in these directions, but continued to calculate the directional plastic strain in all six orientations. In this calculation, band-size distributions are represented by a series of discrete size groups. (The model option with an analytical form for the size distribution was not used.) For each of the orientations, there are six size groups.

The purpose of these calculations was to examine the unzipping slide line logic. Since the SNAG parameters for 4340 steel are still being determined, we used instead the parameters previously determined for a high fragmentation steel.³³ For this material, the maximum band size at nucleation is 0.07 cm. The radii of the bands are initialized so that the ratio of successive intervals between radii is equal to 1.4. Hence, if the maximum radius is 0.07 cm, the next size radius group is 0.05 cm, and so on. The threshold equivalent plastic shear strain for shear band nucleation is 0.7.

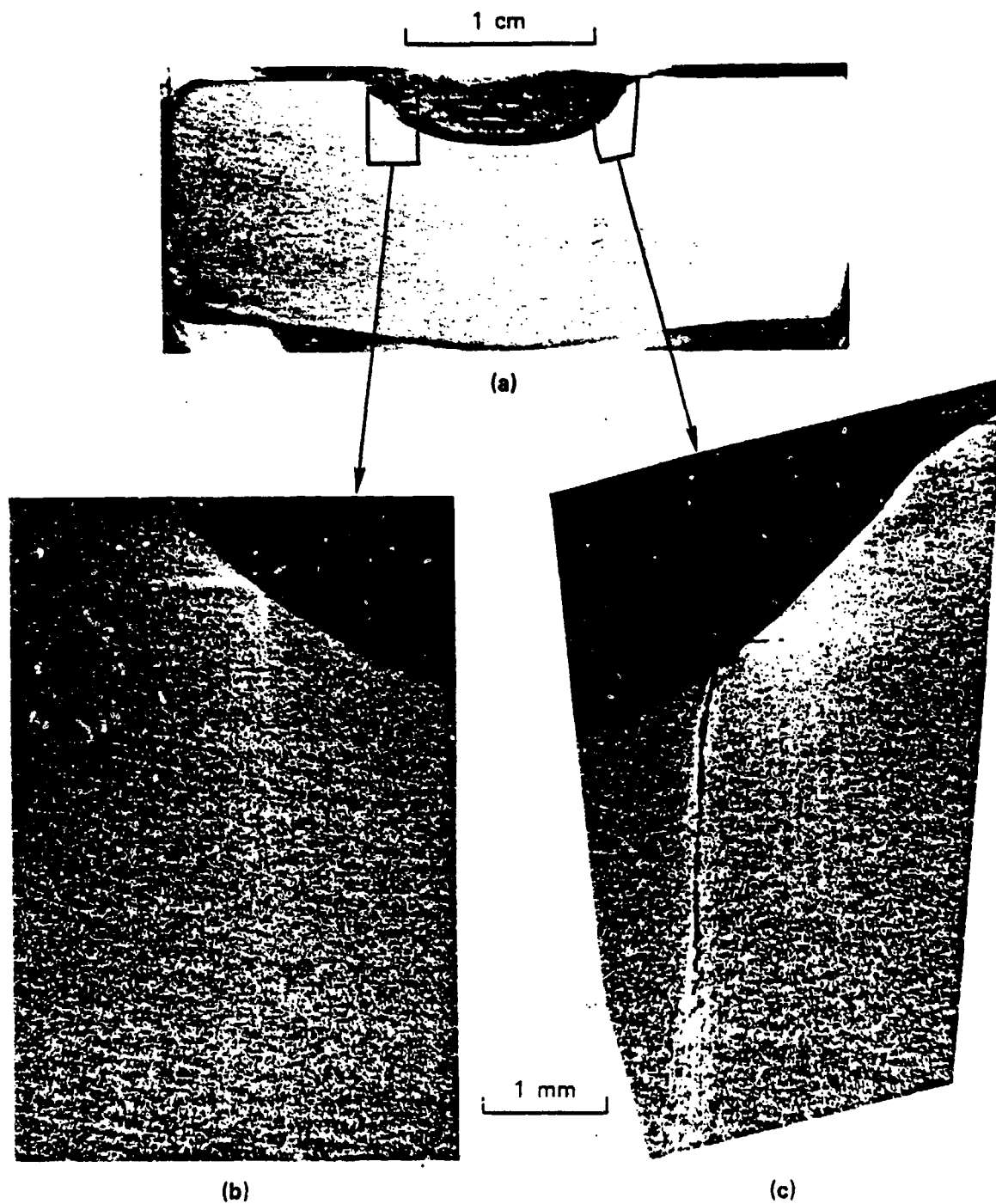
The values of all the parameters used are summarized in Table 4. In addition to the usual variables carried per cell, 63 additional variables were used.



MA-7893-33A

FIGURE 28 INITIAL CONDITIONS FOR CALCULATION OF A STEEL PROJECTILE OF VELOCITY 0.75 km/sec IMPACTING A STEEL TARGET

The slide line is defined by 10 nodal points and is unzipped during the calculation.



MP-6802-9

FIGURE 29 CROSS SECTION (a) THROUGH TARGET RECOVERED FROM SHOT 6802-4 (0.79 km/sec IMPACT VELOCITY) WITH DETAILS (b) AND (c) OF INCIPIENT SHEAR BANDS

Table 4

SHEAR2 MATERIAL PROPERTIES USED IN COMPUTATIONAL SIMULATIONS OF 4340 STEEL ROD IMPACTING NORMALLY A 4340 STEEL TARGET

Nucleation equivalent plastic threshold strain, $\bar{\epsilon}_{cr}^p$	0.17
Maximum band size at nucleation, R_{max}	0.07 cm
Ratio of successive intervals between band sizes	1.4
Nucleation size parameter, R_1 , from Eq. (III-18)	0.011 cm
Nucleation rate parameter, A_N , from Eq. (III-25)	$0.001 \text{ sec}^2 \text{ cm}^{-3}$
Growth rate parameter from Eq. (III-26), C_g	30
Ratio of band jog to band radius, b	0.07
Critical internal energy from Eq. (III-25'), E_{cr}	$7 \times 10^9 \text{ erg/g}$
Number of orientations used, NANG	6
Number of size groups assigned to each orientation.	
<u>Orientation</u>	<u>Number</u>
1	6
2	6
3	0
4	6
5	6
6	0

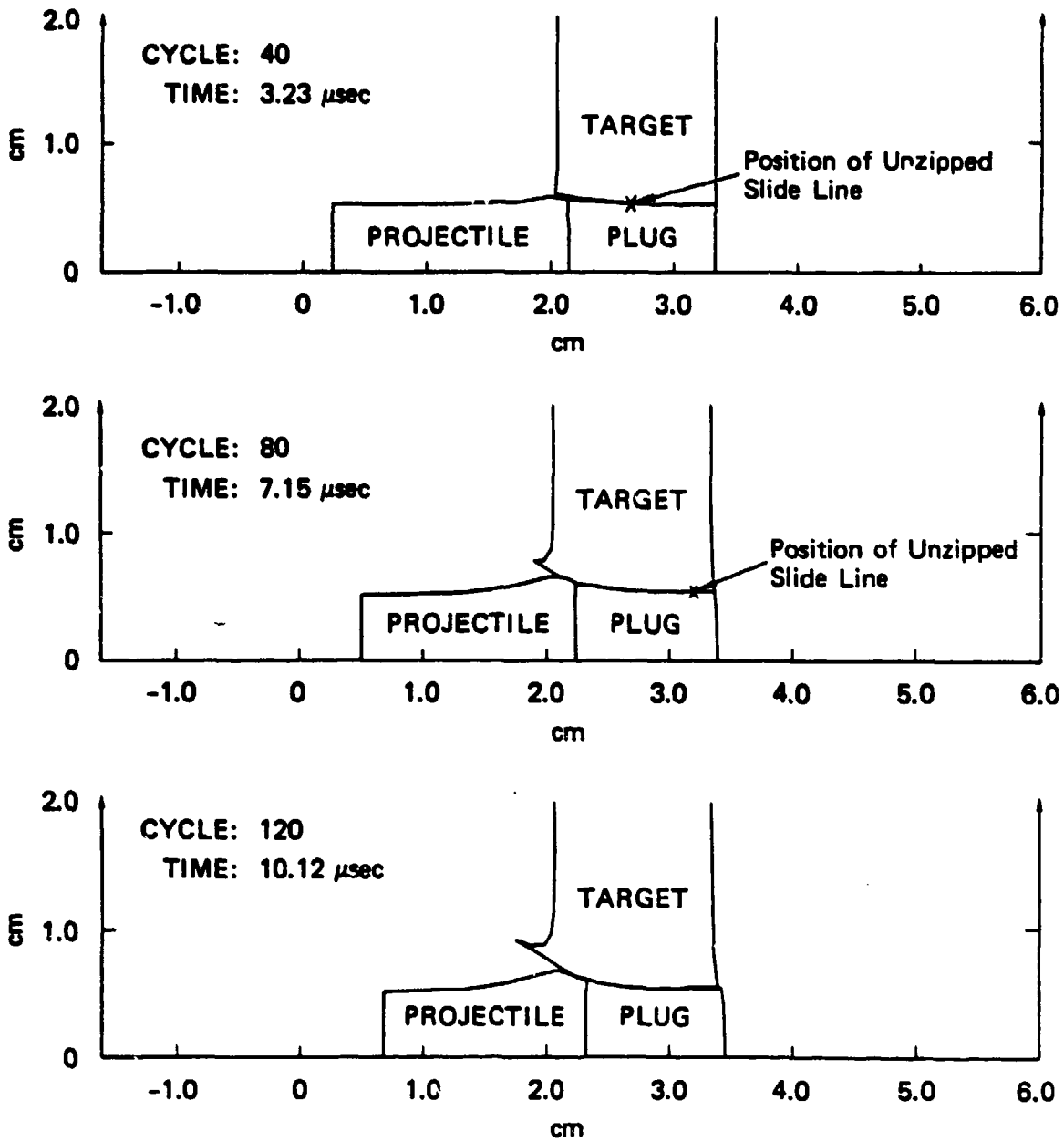
As shown in Figure 28, the slide line was placed in the target directly under the edge of the penetrator to form the boundary of the plug. Whether this slide line is unzipped as the calculation progresses depends on whether the specified threshold condition has been reached. In this calculation the slide line is defined by 10 nodal points.

To examine the unzipping slide line behavior, we used two threshold criteria for unzipping. The first criterion was a critical value of the equivalent plastic strain. By systematically varying this value, we produced various amounts of unzipping and tested the stability of the unzipping logic. These calculations are described in Reference 10. However, this unzipping criterion is unrealistic because it is not directly connected to the amount of microscopic shear band damage. Therefore, after the unzipping logic had been tested, a second criterion was used, namely a critical value of the damage parameter τ , where τ is the fraction of a material cell's strength that has been removed by shear banding. The results of some of these calculations are discussed in the following paragraphs.

4. Selected Computational Results

Two computations are described here. The first deals with an unzipping slide line for which the unzipping is governed by a critical plastic strain. The second calculation deals with a slide line that uses a damage parameter calculated from the shear-banding subroutine to trigger the unzipping process. The results of this calculation are compared with the results of the impact shown in Figure 29.

(a) Plastic Strain Criterion for Slide Line Activation. The results of a calculation in which a threshold plastic strain of 10% was used to trigger the unzipping of a slide line are shown in Figure 30. The process is shown in three successive stages of development. Here the slide line was defined by 10 nodal points; no nodal point slid until one of its neighboring cells reached the 10% critical plastic strain threshold. The unzipping of the slide line (complete formation of the plug) took about 10 μ sec or 120 computational cycles.



MA-7893-73

FIGURE 30 UNZIPPING SLIDE-LINE CALCULATION WITH THRESHOLD PLASTIC STRAIN OF 10%

This calculation was one of the series reported in Reference 10 to test the unzipping logic, and is reproduced here to show several features. First, when the penetrator overmatches the target, the projectile nose does not mushroom enough to impact the target face, and only one active slide line is required. Second, the macroshear band advances in a reasonable way through the target and releases the plug without computational difficulty. Third, the behind-the-armor fragment environment would be described completely by the unfragmented portion of the plug plus the shear band-produced fragmentation of the plug and penetrator nose.

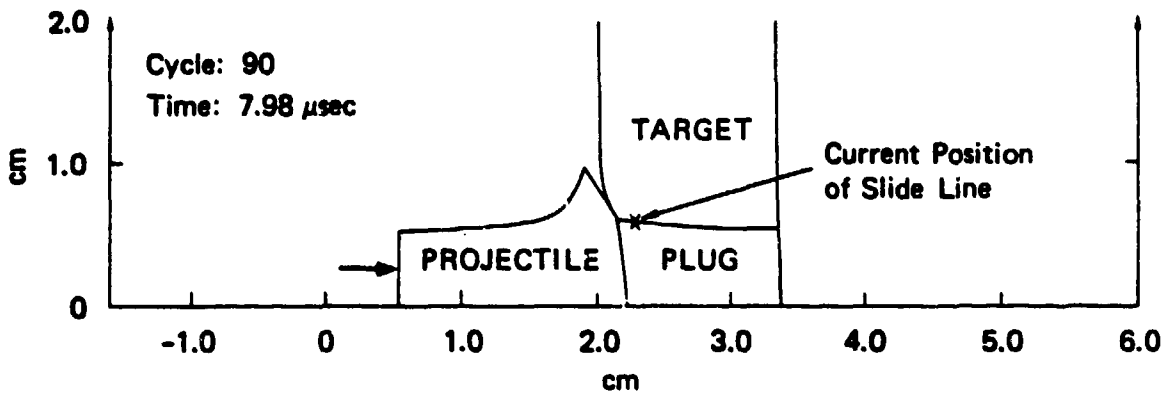
(b) Shear Band Damage Criterion for Slide Line Activation.

Following the above debugging calculations to examine the unzipping slide line behavior, we performed a simulation in which the unzipping criterion was a critical value of the parameter τ

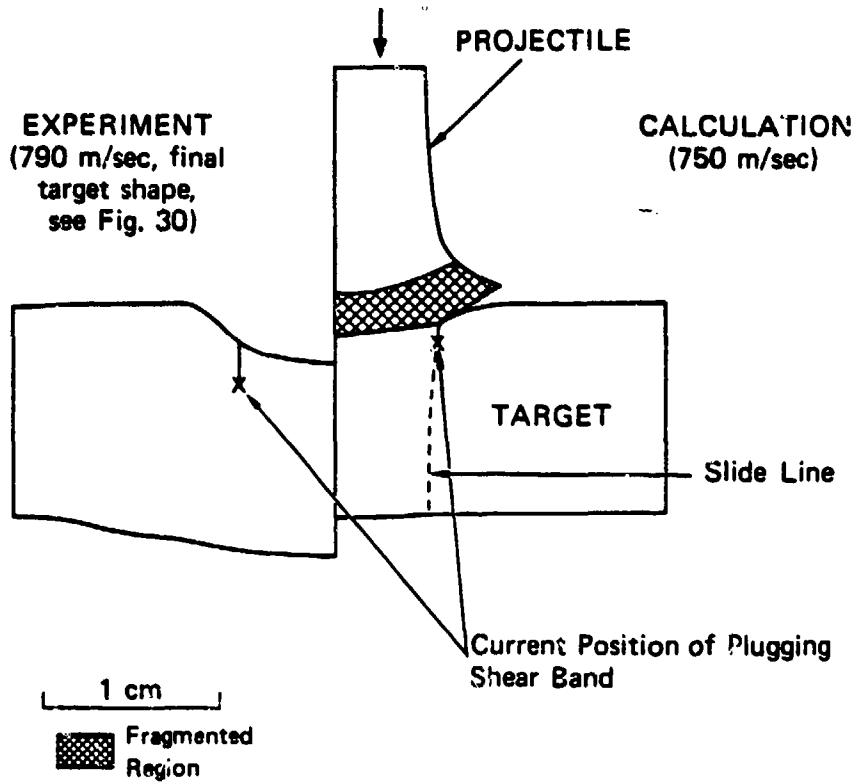
$$\tau = \frac{4}{3} \pi \sum_i N_i R_i^3,$$

which is related to the percentage of microscopic shear band damage in the cell. N is the number of bands per unit volume, R is the band radius, and the subscript i refers to the band size group. The critical value of τ chosen for the calculation was 2.0.* The resulting deformed grid at 7.98 μ sec after impact is shown in Figure 31(a). The calculation was stopped at 7.98 μ sec when the projectile bulge began to impact the target shoulder, thus necessitating a second slide line between the front of the target and the side of the projectile, as discussed above. At this time, approximately the front third of the rod was calculated to have been fragmented by shear banding, the rod still had 44% of its original momentum, and the velocities of the front and rear of the rod had dropped to 88 m/sec and 607 m/sec, respectively. The

*The selection of this value was an error that was undetected until after the calculation was performed. The desired value was 1, corresponding to complete local fragmentation due to shear banding. The effect of this larger value of τ will be to delay the unzipping somewhat.



(a) CALCULATION 7.98 μ sec AFTER IMPACT



(b) COMPARISON OF COMPUTED WITH OBSERVED PENETRATION BEHAVIOR

In the calculation the projectile still has 44% of its original momentum, but the front portion is fragmented by shear banding. The calculation was stopped because the shoulder of the projectile has struck the target face, thus requiring another slide line.

MP-7893-72

FIGURE 31 UNZIPPING SLIDE-LINE CALCULATION WITH THRESHOLD SHEAR BAND DAMAGE PARAMETER, $\tau = 2$, AND COMPARISON WITH EXPERIMENT

central deflection of the target is 0.22 cm and the protrusion at the back is 0.03 cm. The slide line has only been activated for a short distance into the target as shown. The diameter of the slide line surface has expanded from the original 1.03 cm to 1.28 cm.

These computational results were compared with the experimental results of Shot 6802-4 shown in Figure 29 to gain insight into the penetration process; the comparison is shown in Figure 31(b). The comparison can only be qualitative because the calculation was stopped before the projectile was completely fragmented or had come to rest, the shear band parameters were for a different steel than 4340, and an unrealistically large value of τ was inadvertently used. Nevertheless, we consider the comparison very promising. The shear banding and formation of a macro-band or plug appears to be occurring correctly in the calculation, and the front surface crater and rear surface bulge are developing as observed experimentally. The mushrooming of the rod nose and impact with the target face also seem to occur both computationally and experimentally at this impact velocity. The comparison shows that a double slide line is required to correctly represent the penetration in some cases, and will certainly be required in most oblique impact cases.

During the next year we plan to perform more such calculations using the SHEAR3 subroutine in place of SHEAR2; both 4340/4340 and DU/RHA normal impact experiments over a range of impact velocities will be simulated to test the model's ability to reproduce the main features of normal penetration and fragmentation. In addition, work will begin on simulation of oblique impacts.

IV CONCLUSIONS AND FUTURE PLANS

The key conclusion to date is that adiabatic shear banding is very probably the dominant mechanism for plugging and fragmentation of RHA and for erosion of the DU penetrator nose. Furthermore, the computational shear band model SHEAR3 should provide adequate modelling of this behavior. We will test these conclusions further during the next year by performing higher impact velocity phenomenology tests and additional computational simulations.

In the upcoming phenomenology experiments and computations, we will concentrate on the effects of impact obliquity and yaw, since most of the quantitative results to date concern only normal impacts.

Tensile failure by ductile void nucleation, growth, and coalescence is probably the second key failure mode, governing spall and petalling of the target and fracture of the rear portion of the DU rod. However, further phenomenology experiments are required to confirm this conclusion. NAG models have been developed and are ready for application to the phenomenology experiment results.

We conclude further that the program organization and milestones diagrammed in Figure 1 are still valid and feasible, and we shall continue to follow that approach during the next year.

Specific tasks for the second year of the contract were determined during a meeting at AMMRC in August 1979. Depleted uranium (DU), tungsten, and, possibly, electro-slag-remelted (ESR) steel are to be procured. Targets and penetrators from experiments performed at BRL and AMMRC are to be obtained and examined to determine the dominant fracture modes. Additional phenomenology experiments with DU rods and RHA targets will be conducted at SRI and at BRL with appropriate obliquity, velocity, and yaw to further define the fracture modes of both elements. Contained-fragmenting-cylinder tests and other fracture-characterizing

experiments will be conducted by SRI on RHA and DU. (Decisions concerning specific experiments will be based on the results of the phenomenology tests.) The improved shear-band model, SHEAR2, will be applied to the 4340 steel data, tested by simulation of a penetration experiment into a 4340 steel target, and then applied to the RHA and DU data to represent plugging and penetrator nose erosion. SHEAR3 will be implemented in the HEMP code and will be exercised with double slide lines. These planned tasks are discussed in more detail below.

A. Materials Selection and Phenomenology Experiments

BRL, AMRC, and SRI have jointly decided to study a uranium-3/4 wt% titanium alloy first. The uranium used is depleted uranium, ${}_{92}^{238}\text{U}$, the fissionable isotope having been removed.

During the past few months, a supply of the alloy was selected, the material was fabricated, and the necessary specimens were machined and shipped to SRI. The specimens were machined only from rods containing centerline porosity of less than 40 μm in diameter.

1. DU Rods Penetration Phenomenology and Characterization Experiments

Ten 4.7-g hemispherical-nosed rods, 0.125 inches in diameter and 1.250 inches long ($L/D = 10$), were machined from the bar stock. The SRI ballistic test facility will be used to fire these rods at previously characterized $R_c 22$ RHA targets at oblique angles to determine the failure phenomenology of U-3/4 wt% Ti alloy. In addition, 15 65-g hemispherical-nosed rods, 0.3023 inches in diameter and 3.023 inches long ($L/D = 10$), were machined from the same 1.4-inch-diameter bar stock. These rods will also be fired at oblique $R_c 22$ RHA targets, using our light gas gun, to study phenomena scalability. After the phenomenology experiments have determined what failure or deformation modes require quantitative characterization, these rods may also be used for DU characterization experiments.

Both the 4.7-g and the 65-g rods were machined from the bar stock in such a manner as to avoid measurable centerline porosity.

In addition to these phenomenology experiments to be performed at SRI, additional DU/RHA experiments will be performed at higher impact velocities at BRL under the direction of W. Gillich. The purpose of these tests will be to obtain behind-the-armor fragmentation data as well as phenomenology information.

2. DU Tubes for Confined-Fragmenting-Cylinder Experiments

If adiabatic shear banding is confirmed to be the dominant failure mechanism in U-3/4 wt% Ti during ballistic impact, a series of confined-fragmenting-cylinder experiments will be conducted to determine the necessary parameters for the SHEAR3 computational model. A total of 12 tubes, 1.280 inches outside diameter, 0.880 ± 0.0005 inch inside diameter, and 4.0 inches long, have been machined from the same 1.4-inch-diameter bar stock. These tubes were difficult to machine because of the nature of the alloy and the dimensional tolerances required.

All 12 tubes, all 15 65-g projectiles, and all 10 4.7-g projectiles have been received by SRI.

3. Tungsten Alloy Penetrators

Discussions are now under way with BRL and AMMRC personnel to arrange for SRI to receive, for metallographic examination, penetrator and rod fragments from a series of penetration experiments planned at BRL and AMMRC. These experiments will be discussed more thoroughly in future reports.

B. Material Characterization Experiments

1. Contained-Fragmenting-Cylinder (CFC) Experiments

During the next year several additional CFC experiments will be performed on RHA material, and experiments may be initiated with DU material. The SHEAR3 model, as modified by correlation with the 4340 steel data, will then be applied to both the RHA and DU data.

2. Symmetric Taylor Tests

Several symmetric Taylor tests on RHA and DU rods will be performed, and the data will be analyzed with the help of 2-D code calculations to determine the dynamic yield functions.

3. Smooth Bar Tensile Tests

We will initially attempt to obtain smooth bar tensile test data for DU from the literature. If such data are unavailable or ambiguous, we may perform several such tests at SRI.

4. Plate Impact Experiments

Plate impact experiments to obtain the NAG parameters for dynamic ductile void nucleation, growth, and coalescence in (composition) tungsten alloy have been previously performed by Gerald Moss at BRL, are currently under way at BRL for our baseline RHA material, and are planned during the upcoming year for DU material. The DU material is from the same batch described above for the rod and cylinder tests.

C. Computational Model Adaptation

1. SHEAR3

As discussed above, the SHEAR3 subroutine for adiabatic shear banding is currently being debugged and used to correlate the results of computational simulations with 4340 steel CFC data. No further development of SHEAR3 is foreseen during the next year; instead, we will concentrate on documentation and application of SHEAR3 to DU/RHA penetration problems.

2. DFRACT and DFRACST

DFRACT, the NAG subroutine for dynamic ductile void growth, will be used in its current form to correlate BRL's plate impact experimental data for Tungsten, RHA, and DU, so as to obtain the dynamic NAG material parameters for these materials. No additional code development of DFRACT is foreseen.

DFRACTS, the NAG subroutine for quasi-static ductile void growth, has yet to be inserted in wave propagation codes and debugged. These steps will be delayed until the phenomenology experiments have established the importance of this damage mode in armor petalling or penetrator fracture.

D. Generation and Testing of Model Parameters

As discussed above, microstructural failure data will be available during the next year for 4340 steel, RHA material, DU, and tungsten. These data will include results from quasi-static tensile tests, plate impact tests, CFC tests, and symmetric rod impact tests. These data will be correlated with computational simulations to generate and test model parameters for DFRAC, SHEAR3, and, possibly DFRACTS. During the next year we plan to complete this program for SHEAR3 using 4340 steel and RHA material, whereas the remaining work would be completed during the third year.

E. Adaption of HEMP Code for Use with NAG Material Models

During the next year the subroutine SHEAR3 will be inserted in HEMP, debugged, and run on penetration problems with double slide lines and, if necessary, rezoning. We will begin insertion of the subroutines DFRAC and, if necessary, DFRACTS. These insertions will be documented in cooperation with BRL and AMMRC personnel.

F. Computational Simulations

Successfully implementing SHEAR3 in HEMP and testing with double slide lines and rezoning will occupy a major portion of the second year's effort. The computational simulations involved in this effort will be of two types. In the first, computational simulations will be attempted of normal impacts against single RHA plates ranging from near the ballistic limit to cases where the target plate is significantly overmatched. We will compare the results to phenomenology experimental data, and study the ability of SHEAR3 to successfully predict penetrator and target fragmentation and the behind-the-armor fragment environment.

In the second computational simulation effort, we will begin simulating cases of varying impact obliquity and yaw. In these cases, the two-dimensional nature of the codes will restrict us to plate-on-plate simulation. Previous work at LLL³⁴ and BRL³⁵ has shown that the main features of oblique rod impact can be simulated with the plate-on-plate approximation.

REFERENCES

1. "Computational Model for Armor Penetration," SRI project for BRL and AMRC, Contract No. DAAK11-78-C-0115, Progress Report No. 1 (November 30, 1978).
2. Ibid, Progress Report No. 2 (January 29, 1979).
3. Ibid, Progress Report No. 3 (February 15, 1979).
4. Ibid, Progress Report No. 4 (March 15, 1979).
5. Ibid, Progress Report No. 5 (April 15, 1979).
6. Ibid, Progress Report No. 6 (May 15, 1979).
7. Ibid, Progress Report No. 7 (July 20, 1979).
8. Ibid, Progress Report No. 8 (July 30, 1979).
9. Ibid, Progress Report No. 9 (September 10, 1979).
10. Ibid, Progress Report No. 10 (October 15, 1979).
11. Ibid, Progress Report No. 11 (November 15, 1979).
12. R. F. Benck, "Quasi-Static Tensile Stress Strain Curves--II, Rolled Homogeneous Armor," BRL Memorandum Report No. 2703, USA Ballistics Research Laboratory, Aberdeen, MD (November 1976).
13. G. E. Hauver, "The Alpha-Phase Hugoniot of Rolled Homogeneous Armor," BRL Memorandum Report No. 2703, USA Ballistics Research Laboratory, Aberdeen, MD (August 1979).
14. C. J. Smithells, Metals Reference Book, Volume II, Third Edition (Butterworth, Inc., Washington, D.C. 1962), p. 706.
15. R. E. Reed-Hill, Physical Metallurgy Principles (Van Nostrand Reinhold Company, New York, 1964), pp. 459-460.
16. Leroy Hord, Lawrence Livermore Laboratory, private communication.
17. H. C. Rogers, "Adiabatic Shearing - A Review," Drexel University Report prepared for U.S. Army Res. Office (1974).

18. D. C. Erlich, L. Seaman, D. A. Shockey, and D. R. Curran, "Development and Application of a Computational Shear Band Model" SRI Final Report on Contract DAAD05-76-C-0762 for U.S. Army Ballistic Research Laboratory, Aberdeen, MD (May 1977).
19. U.S. Lindholm, in Proceeding of the Second International Conference on Mechanical Behavior of Materials, 16-20 August, 1976.
20. G. Taylor, "The Use of Flat-Ended Projectiles for Determining Dynamic Yield Stress," Proc. of Roy. Soc., 194A (September 1948).
21. M. L. Wilkins and M. W. Guinan, J. Appl. Phys. 44, 1200 (1973).
22. Contract DAAK11-79-D-0019.
23. L. Seaman, D. R. Curran, and D. A. Shockey, "Computational Models for Ductile and Brittle Fracture," J. Appl. Phys., 47, 11 (November 1976).
24. G. Moss and P. H. Netherwood, Jr. "Fracture of a Tungsten-Nickel-Iron Alloy with Stress Waves," Bulletin of American Physical Society, p. 1310, December 1976.
25. G. Moss, P. H. Netherwood, Jr., and L. Seaman, "Characterization of Dynamic Fracture of Rolled Homogeneous Armor," BRL Memorandum Report in preparation; G. Moss and L. Seaman, "Fracture of Rolled Homogeneous Armor," BRL Memorandum Report in press.
26. L. Seaman and D. A. Shockey, "Models for Ductile and Brittle Fracture for Two-Dimensional Wave Propagation Calculations," SRI International Final Report AMARC CTR 75-2 for Army Materials and Mechanics Research Center, Watertown, MA (February 1975).
27. D. A. Shockey, D. R. Curran, L. Seaman, and K. C. Dao, "Analysis of Small Fracture Mechanics Specimens and Construction of a Failure Model for Obtaining Valid Toughness Data from Charpy Tests," SRI International Report for Electric Power Research Institute, Palo Alto, CA (September 1977).
28. L. Seaman, R. E. Tokheim, and D. R. Curran, "Computational Representation of Constitutive Relations for Porous Material," SRI International Final Report for DNA, DNA 3412F (May 1974).
29. A. L. Gurson, "Continuum Theory of Ductile Rupture by Void Nucleation and Growth: Part I - Yield Criteria and Flow Rules for Porous Ductile Media," J. Engin. Mater. Tech., Trans. of ASME, January 1977, pp. 2-15.

30. M. M. Carroll and A. C. Holt, "Suggested Modification of the P- α Model for Porous Materials," J. Appl. Phys., 42, 759 (February 1972).
31. D. C. Erlich, D. R. Curran, and L. Seaman, "Further Development of Computational Shear Band Model," SRI Final Report, Contract No. DAAG46-77-C-0043, for U.S. Army Materials and Mechanics Research Center, Watertown, MA (May 1979).
32. L. Seaman and D. R. Curran, "TROT Computer Program for Two-Dimensional Stress Wave Propagation," SRI Final Report, Volume III, Contract No. DAAG11-77-C-0083, for U.S. Army Ballistics Research Laboratory, Aberdeen Proving Ground, MD (August 1978).
33. L. Seaman, D. A. Shockey, D. R. Curran, and R. E. Tokheim, "Development of a Shear Band Model for Fragmentation in Exploding Cylinders," SRI Final Report, Contract No. N001780-74-C-0450, for Naval Surface Weapons Center, Dahlgren, VA (August 1975).
34. D. M. Norris, Jr., W. H. McMaster, and M. L. Wilkins, "Long-Rod Projectiles Against Oblique Targets: Analysis and Design Recommendations," Lawrence Livermore Report No. UCRL-52057 (April 1976).
35. J. Zukas, Ballistic Research Laboratory, referred to as a "private communication" in Reference 34.
36. Karl Terzaghi, Theoretical Soil Mechanics (John Wiley and Sons, Inc., N.Y. 1943).
37. J. R. Rice, "The Localization of Plastic Deformation," in Theoretical and Application Mechanics, W. T. Koiter, Ed. (North-Holland Publishing Company 1976), pp. 207-220.
38. R. J. Clifton, "Adiabatic Shear," Draft of report for the National Research Committee on Material Response to Ultrahigh Loading Rates (1979).
39. H. C. Rogers, "Material Factors in Adiabatic Shearing and the Implication for Analyses," Drexel University, TTCP-P-TP1 (May 11, 1979).
40. The thermal softening data were taken from Aerospace Structural Metals Handbook, AFML-TR-68-115, Vol. 1, Mechanical Properties Data Center, Traverse City, MI (1972).
41. D. A. Shockey, R. D. Caligiuri, and R. L. Jones, "Evaluation of the Impact Characteristics of Ultrahigh Carbon Steel," SRI Final Report on Contract DNA001-78-C-0266 for DARPA, Arlington, VA (June 1979).

APPENDIX A

THE SHEAR3 SUBROUTINE FOR ADIABATIC SHEAR BANDING

1. Modifications to SHEAR2

The shear band model has been extensively modified since the documentation of SHEAR2.^{18,31} The shear band size distributions were changed from a series of discrete points to an analytical form (Ref. 2), and the stress relaxation associated with damage was completely rederived (Ref. 4). Additional modifications were made in recent months to incorporate the new nucleation and growth relations and to reduce the number of special variables per cell required by the subroutine. This reduction was accomplished by:

- Eliminating $NH3$, EN , and $PLEN$ (which represent an indicator, the total number of bands in all orientations in each cell, and the plastic work).
- Providing an option for storage of plastic strains in each orientation. The strains are not required for the calculation but are of great interest in assessing the relative potential for damage of each orientation. This option permits the user to avoid storing these strains.
- Reducing the shear band directions from 6 to 4 on planes: (1) normal to x or y , (2) at 45° between x and y , (3) at 45° between y and z , and (4) at 45° between x and z . This change actually does not reduce the information content from that in the six orientations previously used. With the current nucleation and growth process, the bands normal to x and to y are always identical, so one distribution can represent both orientations. There are no bands normal to the z direction (circumferential in axisymmetric problems) so that orientation is unneeded.
- Providing an option for user selection of shear band orientations. The user can choose to not activate any of the orientations.

With the present configuration of SHEAR3, the additional variables required beyond those for a standard elastic-plastic model are as follows:

TAU , the damage parameter, to be used for triggering slide lines
 EP , $\bar{\epsilon}^P$

ROT, the cell rotation

$\epsilon_{\phi\theta}$, the plastic strain in each orientation (0 to 4 variables)
three variables (N_0 , R_1 , and R_{max}) for each orientation activated.

The call statements for SHEAR3 are similar to those for SHEAR2. The first call is used to read in data and initialize the subroutine: this call is from LAYOUT in TROTT. Only the parameters NCALL and IN are required for this initializing call. The second call statement is in SWEEP of TROTT. This call is for the stress and damage calculations and requires all the call variables. Note that all data passes through the call statement: there are no COMMON variables. The call and associated statements in SWEEP are:

```
492      SXXW=SXX(LM)
        SYTW=SYT(LM)
        TKYW=TKY(LM)
        PW=P(LM)
        LS = 2
        IF (MOD(IN,INPRINT) .EQ. 0) LS = 3
        CALL SHEAR3(LS,5,MAT,K,J,SXXW,SYTW,TKYW,PW,COM(LM+20),
1  DW,D(LM),DT,EW,E(LM),COM(LM+21),EXXH,EYTH,
2  EKXH,F,YY(LM),TH(LM),-ALFA,ESC,COM(LM+22))
        IF (COM(LM+20) .GT. 0.) IH(LM)=3
        SZZW=-SXXW-SYTW
        TH(LM)=TH(LM)-ALFA
        GO TO 600
```

The first four statements bring the deviator stresses and pressure from the main arrays in preparation for the call. LS is set to 2 for normal stress calculations and to 3 for calculations and printing. Following the call, the indicator IH is set to 3 if shear banding has occurred: COM(LM + 20) is the main storage for $\tau = \text{TAU}$, a damage parameter. The rotation factor TH is incremented by ALFA, the differential rotation, which is positive clockwise in TROTT. TH is positive counter clockwise. The stresses and strains are positive in tension; the pressure is positive in compression. The variables in the call statement are listed in Table A-1.

SHEAR3 has been used with the dyn-cm-g-sec system of units exclusively. We have searched through the subroutine, hunting for constants that would require changes if different systems are used. For the Mbar-cm-g- μ sec

TABLE A-1

VARIABLES IN THE CALL TO SHEAR 3

Variable	Meaning
NCALL	Indicator for the type of calculations required in SHEAR 3 0,1 Read data for one material and initialize 2 Calculate only 3 Calculate and print 4 Print only
IN	Data input file number (usually 5)
M	Material number
K	Cell number in the K direction
J	Cell number in the J direction
SX	Deviator stress in the X direction (dyn/cm^2)
SY	Deviator stress in the Y direction (dyn/cm^2)
SZ	Deviator stress in the Z direction (dyn/cm^2)
SXY	Shear stress (dyn/cm^2)
P	Pressure calculated for the cell (dyn/cm^2)
TAU	Damage (ΣNR^3) in the cell calculated on the last cycle; ranges from 0 to 1 (See BFR(M,32))
DH	New incoming density (g/cm^3)
DOLD	Cell density determined on the last cycle (g/cm^3)
DTO	Time step (sec)
EH	Internal energy of the cell in the present cycle (erg/g)
EOLD	Energy of cell in previous cycle (erg/g)

TABLE A-1

(Continued)

Variable	Meaning
EP	Total effective plastic strain
EX	Strain increment in the X direction
EY	Strain increment in the Y direction
EZ	Strain increment in the Z direction
EXY	Tensor shear strain increment
F	Thermal softening factor; varies from 0 to 1
YHL	Yield value calculated on the last cycle [remains unchanged (1) if the yield has not been exceeded, or (2) if it has been exceeded and work hardening is zero] (dyn/cm ²)
ROT	Total angle of cell rotation as of the previous cycle
DROT	Additional angle of cell rotation since the last cycle
ESC	Equation of state variables [array (6,20) must be dimensioned in the calling routine; some of the elements of this array are not used in SHEAR 3]
ESC(M,1)	Original density (g/cc)
ESC(M,2)	Bulk modulus, C (dyn/cm ²)
ESC(M,3), ESC(M,4)	D and S in the pressure equation: $P = C\mu + D\mu^2 + S\mu^3, \text{ where } \mu = DH/ESC(M,1) - 1$
ESC(M,5)	Shear modulus (dyn/cm ²)
ESC(M,9)	" Gruneisen's ratio
CN	Array contains number of shear bands, band lengths, and plastic strains for each cell. The number of array elements required for each cell is

TABLE A-1

(Concluded)

Variable	Meaning
	$N_{CM} = 3\Sigma F_1 + B(F_1)$ <p>where $F_1 = 0$ if $FNUC_1 = 0$ $= 1$ if $FNUC_1 > 0$</p> <p>$B = 0$ for $BFR(M,31) = 0$ $= \Sigma F_1$ for $BFR(M,31) = 1$ $= 4$ for $BFR(M,31) = 2$</p>

system of HEMP, the 1.E+4 at about line 132 should be changed to 1.E-8. Also the internal energy must be transformed from erg/g to Mbar.

$$\rho_0 E_{TROTT} = E_{HEMP} \times 10^{12}$$

Like HEMP, EPIC uses the energy per unit volume definition for E. The input quantities are defined in Table A-2, with nominal values in the units used in TROTT.

For triggering a slide line based on the shear band damage level, the parameters BFR(M,32) and TAU are used. TAU is intended to vary from zero to approximately one, with values of 0.5 or larger being indicative of sufficient damage to cause full separation. The value of TAU can be associated with a particular direction of damage (shear band orientation) or with all damage: this choice is made through selection of BFR(M,32). For BFR(M,32) set to I, where I equals 1, 2, 3, or 4, the Ith shear band orientation is used. For a problem in which a missile were penetrating in the X-direction, BFR(M,32) could be set to 1 to associate TAU with bands in the plugging direction.

The total number of extra variables required per cell will depend on the number of shear band orientations used (governed by FNUC₁), the value of BFR(M,31), and the variables already present in the calling program. With CN in Table A-2, a formula is given for the array size of CN. Other variables that may not be available normally are TAU, EP, YHL, and ROT. F and DROT are computed just before the call and need not be stored.

2. Analytical Form for Shear Band Size Distributions

The storage requirements for the shear band subroutine, SHEAR2, were decreased by imposing an analytic form to the size distributions. The form chosen was the exponential one that fits the shear band data and is also like that used for ductile and brittle fracture. The number of bands per cubic cm with radii greater than R is

$$N_g = N_0 \exp(-R/R_1) \quad (A-1)$$

TABLE A-2

INPUT DATA FOR SHEAR 3

Variable	Nominal Values	Definition
BFR(M,22)	10 (nondim.)	C_G : growth coefficient in $dR/dt = C_G R dc/dt$
BFR(M,23)	5 per cm^3	A_N , nucleation coefficient
BFR(M,24)	0.002 cm	R_n , nucleation size parameter
BFR(M,25)	2 (nondim.)	n, exponent in nucleation rate equation
BFR(M,26)	0.2 (nondim.)	ϵ_n , nucleation threshold strain
BFR(M,27)	0.07 (nondim.)	b, shear distortion associated with a band
BFR(M,28)	0.01 cm	R_B , maximum band size at nucleation
LFR(M,29)	10.0 (nondim.)	V_{FR} , damage factor in $\tau = V_{FR} \cdot b \cdot 6\pi N_0 R_1^3$
BFR(M,30)	0.577 (nondim.)	Tan ϕ , where ϕ is the internal friction angle
BFR(M,31)	2 (nondim.)	Indicator for storage of plastic strains ϵ_i^P 0 no storage 1 store strains for $FNUC_1 \neq 0$ 2 store all strains
BFR(M,32)	1 (nondim.)	Designator for TAU. For $i = BFR(M,32)$, $TAU = \tau_z(i)$
FNUC	1.0 (nondim.)	Indicator array and weighting factor for orientations to be used

where N_0 is the total number/cm³, and R_1 is the size parameter of the distribution. The bands are presumed to be circular, with a radius R , and to be in a plane. As in the earlier version of SHEAR2, the bands are assumed to nucleate and grow in six discrete planes, thus representing approximately a complete angular distribution. This analytic size distribution in Eq. (A-1) replaces the representation by a series of size groups in each angular orientation. Each orientation direction is now represented by three numbers, N_0 , R_1 , and R_B , where R_B is a maximum size of the bands.

The following paragraphs describe the procedure used for nucleation of a new distribution, growth of an existing distribution, and combination of the nucleated and growing distribution to a single exponential in the form of Eq. (A-1).

Shear band nucleation is described by

$$\frac{dN_{\phi\theta}}{dt} = A_n \left(\frac{d\epsilon_{\phi\theta}^{PS}}{dt} \right)^n \quad (A-2)$$

where $N_{\phi\theta}$, $d\epsilon_{\phi\theta}^{PS}$ are number of bands and plastic shear strain in the $\phi\theta$ angular direction, and A_n and n are constants. A limit on the rate of nucleation is provided by requiring that the total distortion represented by the new bands not exceed the total imposed plastic shear strain. The shear strain associated with nucleation is

$$\Delta\epsilon^{PS} = \frac{\pi}{2} \int_{R=0}^{\infty} bR^3 dN \quad (A-3)$$

where $b = B/R$ is the maximum relative offset across the band and dN is the number nucleated with a radius R . By using Eq. (A-1) to obtain the derivative of N in terms of R , and integrating Eq. (A-3), we obtain

$$\Delta\epsilon^{PS} = 3\pi b \Delta N R_n^3 \quad (A-4)$$

where ΔN is the total number per cubic cm nucleated with a size distribution parameter $R_1 = R_n$. Eq. (A-4), is then an upper bound on the number nucleated in any time interval.

Growth of the shear bands is given by the viscous law from Reference 18.

$$\frac{dR_i}{dt} = C_G R_i \frac{d\epsilon_{\phi\theta}^{PS}}{dt} \quad (A-5)$$

where C_G is a growth coefficient. When this viscous growth process is applied to a size distribution as in Eq. (A-1), the entire distribution increases in size. The resulting distribution has the same exponential form, N_0 is unaffected, and the change in R_1 is obtained through the use of Eq. (A-5).

Two constraints are applied to the growth law to limit the maximum growth velocity to the sound speed and to require that the total distortion represented by the growth does not exceed the total imposed plastic shear strain. The maximum growth rate occurs at the maximum radius, according to the viscous growth law, and that radius is called R_B . Hence, the velocity limit implies that the maximum radius at the end of the interval, R_{B2} , is

$$R_{B2} \leq R_{B1} + V_m \Delta t \quad (A-6)$$

where V_m is the shear wave velocity. The increase in the radius parameter is limited by maintaining a constant ratio of R_B/R_1 . The distortion limit on growth is derived in the same manner as in Equations (A-3) and (A-4). The increase in plastic strain associated with the band growth on the $\phi\theta$ plane is

$$\Delta\epsilon_{\phi\theta}^{PS} = 3\pi b N_0 (R_{2\phi\theta}^3 - R_{1\phi\theta}^3) \quad (A-7)$$

where R_2 is the final size distribution parameter. Hence, based on the imposed distortion, this limit is

$$R_{2\phi\theta}^3 = R_{1\phi\theta}^3 + \frac{\Delta\epsilon_{\phi\theta}^{PS}}{3\pi b N_0} \quad (A-8)$$

Combining Equations (A-5), (A-6), and (A-8), we find the value of R_2 on the $\phi\theta$ plane to be

$$R_{2\phi\theta} = \text{MIN} \left[(R_{B\phi\theta} + v_m \Delta t) \frac{R_{1\phi\theta}}{R_{B\phi\theta}} , \right. \\ \left. R_{1\phi\theta} \exp(C_G \Delta \epsilon_{\phi\theta}^{PS}) , \right. \\ \left. \left(R_{1\phi\theta}^3 + \frac{\Delta \epsilon_{\phi\theta}^{PS}}{3\pi b N_{o\phi\theta}} \right)^{1/3} \right] \quad (A-9)$$

After calculating growth of the old size distribution and nucleation of a new distribution with size parameter R_n , we combine the two distributions to form a new distribution with the same form as Eq. (A-1). The combined distribution has the parameters N_3 and R_3 . The combination is made with two constraints:

- The new curve presents the size and number of the largest shear bands ($R = R_B$).
- The new curve represents the sum of the plastic strain of the nucleated and growing distributions.

The first requirement states that the number of bands at R_B is preserved; hence

$$N_{3B} = N_3 \exp(-R_B/R_3) \\ = N_o \exp(-R_B/R_2) + \Delta N \exp(-R_B/R_n) \quad (A-10)$$

The total plastic strain of the new distribution is

$$\epsilon^{PS} = 3\pi b N_3 R_3^3 \quad (A-11)$$

By eliminating N_3 from Eq. (A-11) with the aid of Eq. (A-10), we obtain an expression for R_3 .

$$\epsilon^{PS} = 3\pi b N_{3B} \exp(R_B/R_3) R_3^3 \quad (A-12)$$

where N_{3B} is known from Eq. (A-10). A simple algorithm for solving Eq. (A-12) was developed for the program. N_3 is then obtained from Eq. (A-11), and the final size distribution is fully specified.

The foregoing nucleation, growth, and combination procedures have been incorporated into a version of the shear band routine SHEAR2. We have made a series of calculations and are comparing them with results from the earlier version. The initial observations show that there are differences in the results of the two versions. These differences stem primarily from the approximation (in the new routine) involved in the recombination calculations above, and the summation approximation

$$\sum N_i R_i^3 \approx \int R^3 dN \quad (A-13)$$

implied in the original version. The sum taken over all the size groups is a poor estimate of the integral unless a large number of groups (at least 10) are used and are spaced along the function in an optimum manner.

3. Stress Relaxation Algorithm

The new SHEAR3 stress relaxation process caused by a combination of yielding and growth of shear band damage is derived here. This process is part of a complete computational description of the stress-strain relations for a material undergoing shear band damage. The basic assumptions of the model are presented first, followed by yield calculations for one or more slip planes. The possibility of a combination of shear and tensile damage is treated. In each case the relaxed stresses and plastic strains are obtained. Then steps are provided for implementing the stress relaxation algorithm into a shear band model.

a. Basic Assumptions

The major assumption of the stress relaxation process is that the shear strength of a partially shear banded material depends jointly on the amount of shear banding and the normal stress across the bands. Quantitatively, the shear strength is

$$S = \frac{l}{h} \sigma_n \tan \phi + \frac{h-l}{h} Y_s \quad (\text{A-14})$$

where l is the band length

h is the length of the material block in the band direction

σ_n is the normal stress across the band

ϕ is the friction angle

Y_s is the yield strength in shear (one-half the tensile yield strength).

The configuration of the band and stresses is shown in Figure A-1.

Note that the band reduces the shear stresses S_{12} and S_{21} equally but has no effect on the S_{23} stresses.

Equation (A-14) is extended to the shear band size distributions by introducing the damage density function τ_k , which represents the total area of shear bands per unit volume associated with the k -th plane. The material is fully shear banded for $\tau_k = 1$. Then Eq. (A-14) is assumed to take the form

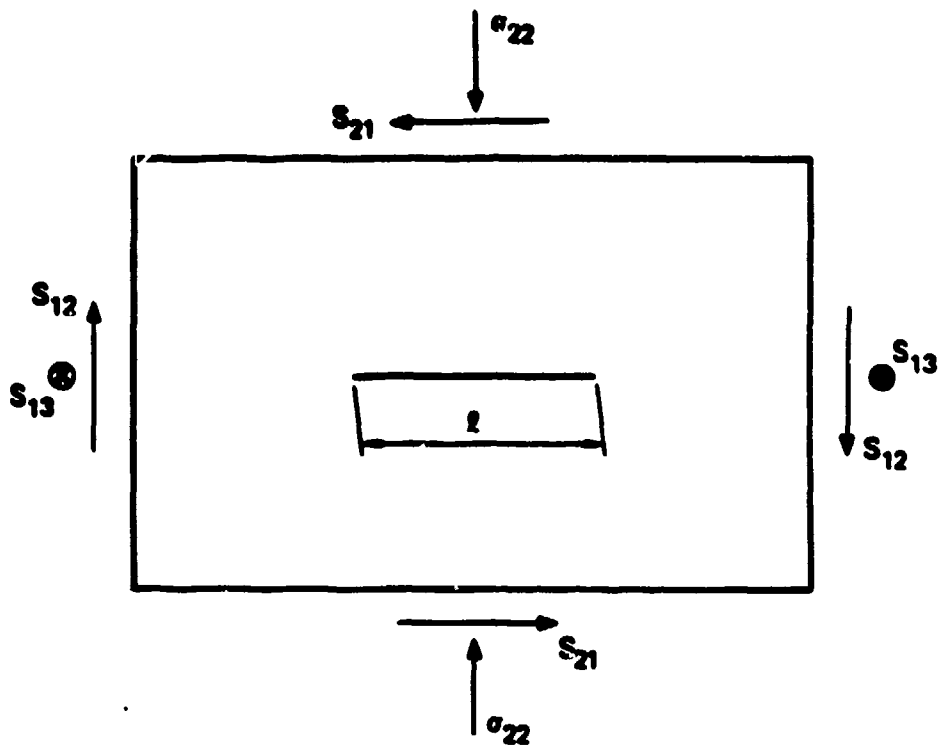
$$S_k = \tau_k \sigma_n \tan \phi + (1 - \tau_k) Y_s, \quad S_k \leq Y_s \quad (\text{A-15})$$

The shear strength is always positive and cannot exceed Y_s .

Central to the use of Eq. (A-15) are the assumptions that

- o The shear band damage can be allocated to planes of interest (such as the X-Y plane) instead of to specific directions (as in tensile fracture).
- o The yield process can be dealt with on specific planes (a Tresca yield approach), rather than by considering all stresses simultaneously, as in a Mises yield process.

Both these assumptions seem to fit the basic mechanisms mentioned earlier.



MA-7883-2A

FIGURE A-1 SHEAR (S) AND NORMAL (σ) STRESS ORIENTATION ON A BLOCK CONTAINING A SHEAR BAND

In the yield process it is further assumed that yielding does not affect the pressure while the material is under compression. Thus the pressure remains a function only of the density and internal energy and is not modified by yielding except by the heat generated.

These assumptions are the basis of the model derived here. With these assumptions, the model will provide for an anisotropy of strength so that on planes that are shear banded the shear strength may go to zero, but shear stresses on other planes will retain full strength. This stress reduction will allow shear bands to propagate through computational cells representing material under high shear.

b. Determination of the Damage

In the shear band model, damage in the form of shear bands is nucleated and grown on the specific planes shown in Figure A-2. The relative shear band area on one of these planes is determined from the shear band size distribution for that orientation

$$N_g = N_o \exp (-R/R_1) \quad (A-16)$$

where N_g is the number greater than R per unit volume

N_o is the total number per unit volume

R is the radius of a shear band, assumed to be circular and plane

R_1 is a shape parameter of the distribution.

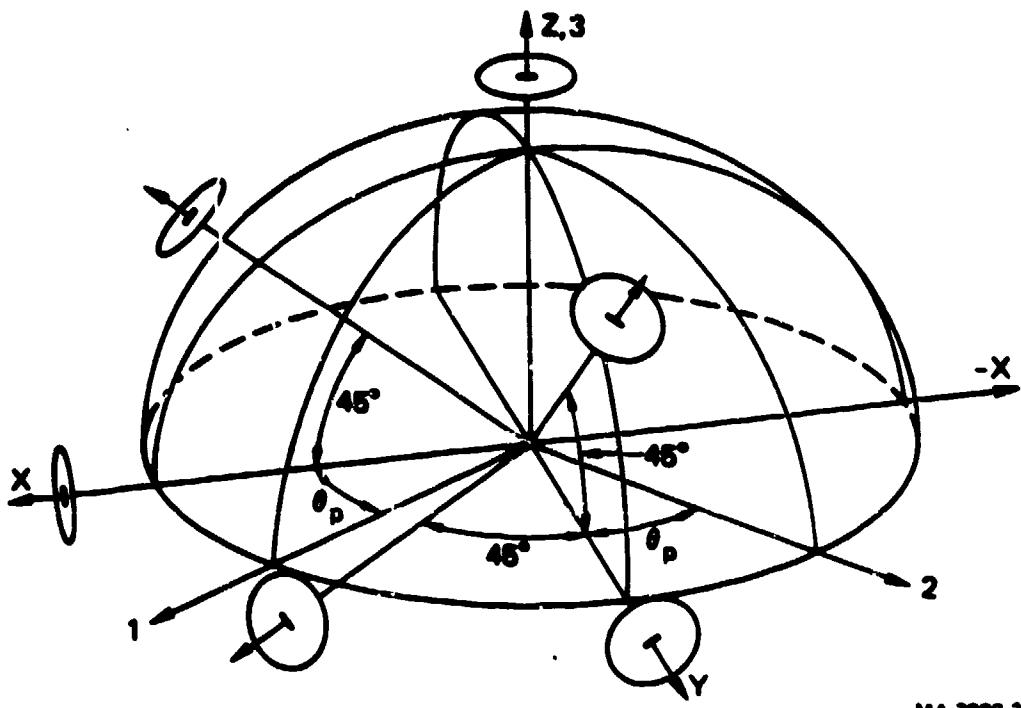
The area is then

$$A_p = \pi \int_{\infty}^0 R^2 dN = 2\pi N_o R_1^2 \quad (A-17)$$

where dN is the number per unit volume with a radius R . To nondimensionalize the damage factor and allow it to approach unity for full damage, a length factor c is introduced. The relative damage on the plane is then

$$\tau_p = cA_p = 2\pi c N_o R_1^2 \quad (A-18)$$

where τ_p is nondimensional.



MA-7893-3

FIGURE A-2 RELATIVE LOCATIONS OF THE X-Y DIRECTIONS, PRINCIPAL DIRECTIONS (NOT NECESSARILY IN ORDER), AND INITIAL ORIENTATION OF THE SHEAR BAND DAMAGE GROUPS

Once we have the damage factors τ_p for each shear band orientation plane, a composite damage factor is required on the planes of interest for the stress calculations. The contribution from each shear band orientation group to the composite factor is a function of the sine of the angle ψ between the normal to the plane of interest (i-j) and the normal to the p-th shear band orientation plane. Hence, for the i-j plane

$$\tau_{ij} = \sum_{p=1}^6 \tau_p \sin^2 \psi_{pij} \quad (A-19)$$

The sum runs over all four orientation groups used in the present shear band model (SHEAR3). With this definition of the composite damage, τ_{ij} for the X-Y plane receives the τ_p values for the X, Y, and X-Y directions with a weighting factor of 1.0 and for the XZ and YZ directions with a factor of 0.5. The shear bands normal to the Z direction do not contribute.

The planes of interest for evaluating the damage factors τ_{ij} are the planes of principal shear stress. For two-dimensional problems, one of these planes is always the X-Y plane because σ_z is always a principal stress. (Z is taken to be in the thickness direction for planar problems and in the circumferential direction for axisymmetric problems.) However, the other two planes can be at arbitrary angles θ and $90 + \theta$ for the X direction as shown in Figure A-2. The weighting factors $\sin^2 \psi_{pij}$ are derived from the rules for spherical triangles. The required weighting factors are given in Table 4-3. With these factors the strength on any principal plane can be evaluated with Eq. (A-15).

c. Yielding on a Single Plane

The yield process associated with Eq. (A-15) may be visualized with the aid of a Mohr diagram as in Figure A-3. The ordinate is the shear stress on a plane, and the abscissa is the normal stress. A circle represents all states of stress in any orientation on a plane. The center of the circle is at

$$\sigma^* = \frac{\sigma_1 + \sigma_2}{2} = \frac{\sigma_x + \sigma_y}{2} \quad (A-20)$$

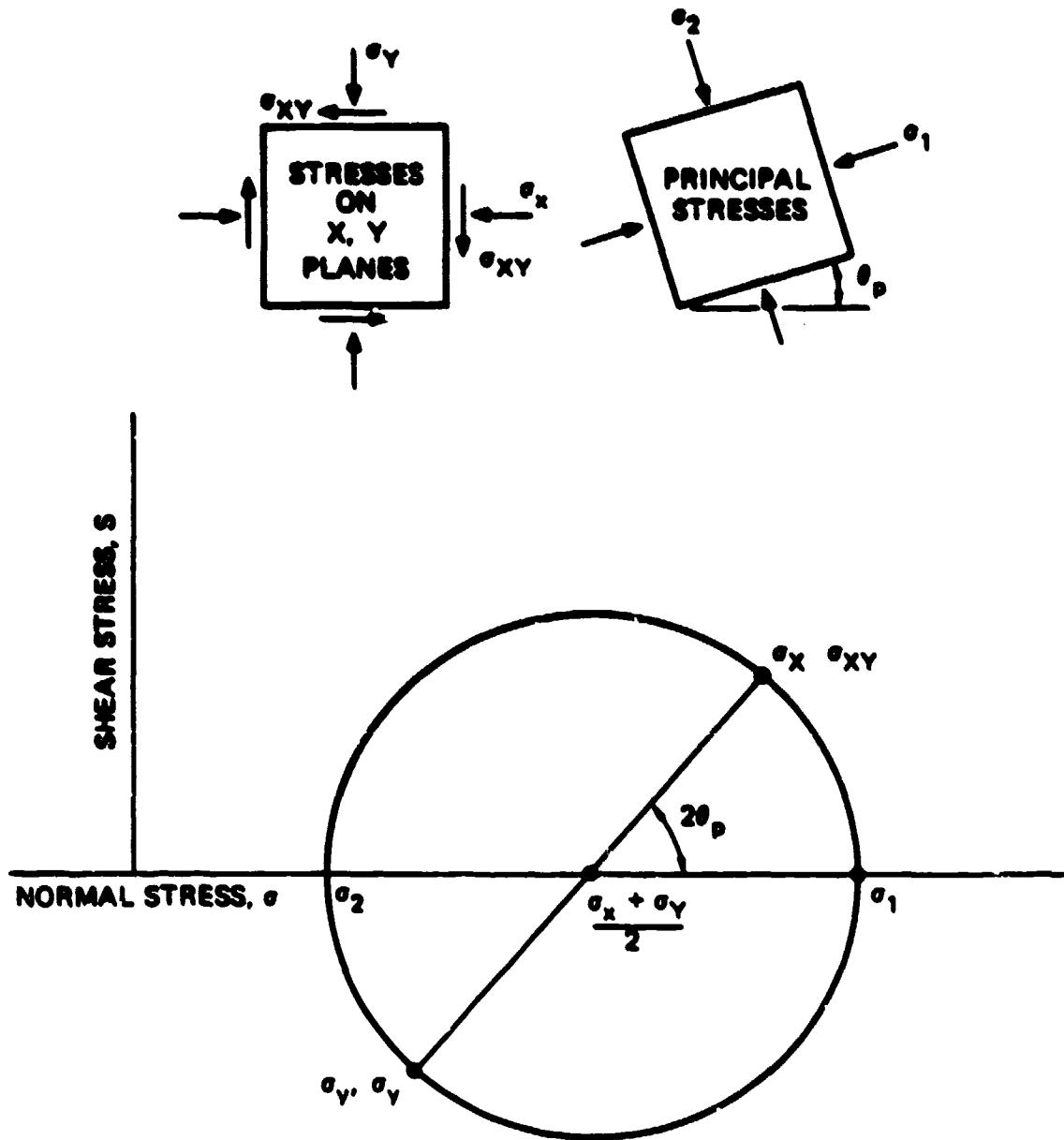
TABLE A-3

WEIGHTING FACTORS $\sin^2 \psi$ FOR RELATING DAMAGE
TO PRINCIPAL PLANES

Shear Band Orientation Group		$\sin^2 \psi$		
		1-Y Plane	1-Z Plane	2-Z Plane
1	X	1	$\cos^2 \theta$	$\sin^2 \theta$
1	Y	1	$\sin^2 \theta$	$\cos^2 \theta$
*	Z	0	1	1
2	XY	0	$1/2(1 + \sin 2\theta)$	$1/2(1 - \sin 2\theta)$
4	YZ	1/2	$1-1/2 \cos^2 \theta$	$1-1/2 \sin^2 \theta$
3	XZ	1/2	$1-1/2 \sin^2 \theta$	$1-1/2 \cos^2 \theta$

Note: θ is the angle to principal direction 1 in the X-Y plane, measured counter-clockwise from X toward the Y direction.

* No bands are currently provided in the Z direction because there is no shear on the plane.



MA-7883-4

FIGURE A-3 MOHR DIAGRAM FOR STRESSES. INSETS SHOW ORIENTATION OF STRESS AT A POINT

where σ_1 and σ_2 are principal stresses that determine the intercepts of the circle with the axis, and σ_x and σ_y are any two normal stresses on orthogonal planes. The small inset blocks in Figure A-3 show the orientation of stresses in the positive sign convention corresponding to points on the Mohr circle. A counterclockwise rotation of θ_p to the direction of principal stress is represented by a clockwise rotation of $2\theta_p$ on the Mohr diagram.

The yield limit is represented by a sloping line in the Mohr diagram up to a shear stress of Y_0 and a horizontal line for larger normal stress. The slope is similar to the usual Coulomb friction law

$$S = \sigma_n \tan \xi + C \quad (A-21)$$

where ξ is the angle of internal friction and C is the cohesion. Comparing Eqs. (A-21) and (A-15), it is seen that

$$\tan \xi = \tau_{ij} \tan \phi \quad (A-22)$$

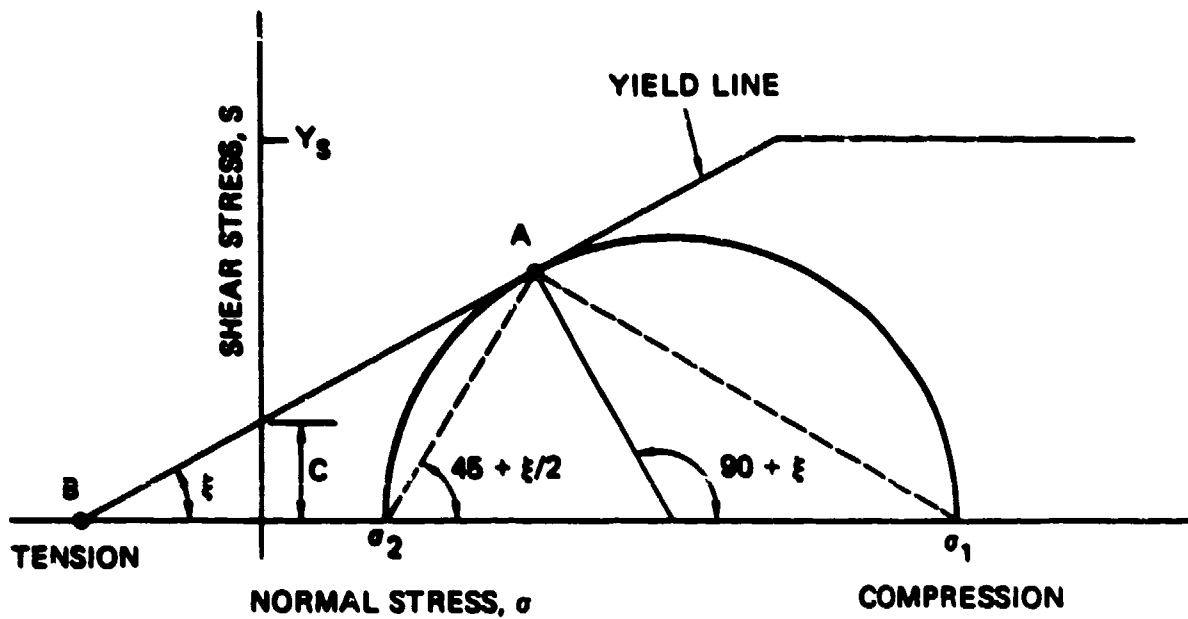
$$C = (1 - \tau_{ij}) Y_0 \quad (A-23)$$

In the sketch in Figure A-4 the Mohr circle is tangent to the yield limit line, so the material is yielding. Yield is actually occurring on a plane with a stress state defined at point A, at an angle of $45^\circ + \xi/2$ from the maximum principal stress.

From the foregoing yield process, the stress states at yielding can be fully determined. As shown in Terzaghi,³⁶ the principal stresses on the Mohr circle at yield are

$$\sigma_1 = 2C \sqrt{N_\xi} + \sigma_2 N_\xi \quad (A-24)$$

where $N_\xi = \tan^2(45^\circ + \xi/2) = (1 + \sin \xi)/(1 - \sin \xi)$ and N_ξ is called the flow value. In general then, for the three possible planes between the principal directions,



MA-7893-5

FIGURE A-4 MOHR CIRCLE FOR STRESS STATES WITH A YIELD LINE FOR YIELDING ON THE 1-2 PLANE

$$\sigma_i = 2(1 - \tau_{ij})Y_s \sqrt{N_{\xi ij}} + \sigma_j N_{\xi ij} \quad (A-25)$$

where τ_{ij} and $N_{\xi ij}$ are the damage factor and flow value of the ij plane and $\sigma_i > \sigma_j$.

For computational purposes, it is convenient to define a yield function g_{ij} that is zero at yield, negative for elastic behavior, and positive for inadmissible states beyond the yield limit:

$$g_{ij} = \max \left[\frac{\sigma_i - \sigma_j}{2} - (1 - \tau_{ij})Y_s \sqrt{N_{\xi ij}} - \sigma_j \frac{(N_{\xi ij} - 1)}{2}, \right. \\ \left. \frac{\sigma_i - \sigma_j}{2} - Y_s \right] \quad (A-26)$$

This definition of g includes the limit Y_s on the yield strength. The value of g represents the excess shear strength above the yield line.

Having defined the yield function g_{ij} , we can determine the post-yield stresses and plastic strains. Let the principal stresses computed by assuming all the strains are elastic be σ_i^N and the yield function based on these stresses be g_{ij}^N . The postyield stresses are σ_i , where

$$\sigma_i = \sigma_i^N + \Delta\sigma_i \quad (A-27)$$

On the ij plane, yield occurs without disturbing the third principal stress or the pressure. Therefore:

$$\sigma_i + \sigma_j = \sigma_i^N + \sigma_j^N \quad \text{and} \\ \Delta\sigma_i = -\Delta\sigma_j \quad (A-28)$$

Replacing σ_i and σ_j in Eq. (A-26) with σ_i^N , σ_j^N , and $\Delta\sigma_i$ from Eqs. (A-27) and (A-28), we obtain

$$\Delta\sigma_i = -\Delta\sigma_j = \frac{2}{N_{\xi ij} + 1} g_{ij}^N \quad (A-29)$$

This solution is also valid for the horizontal portion of the yield limit if $N_{\xi_{ij}}$ is set to 1.0 for that range. The plastic strains are computed from the change in deviator stress associated with the yielding

$$\Delta \epsilon_i^P = \frac{\sigma_i^N - \sigma_i'}{2G} \quad (A-30)$$

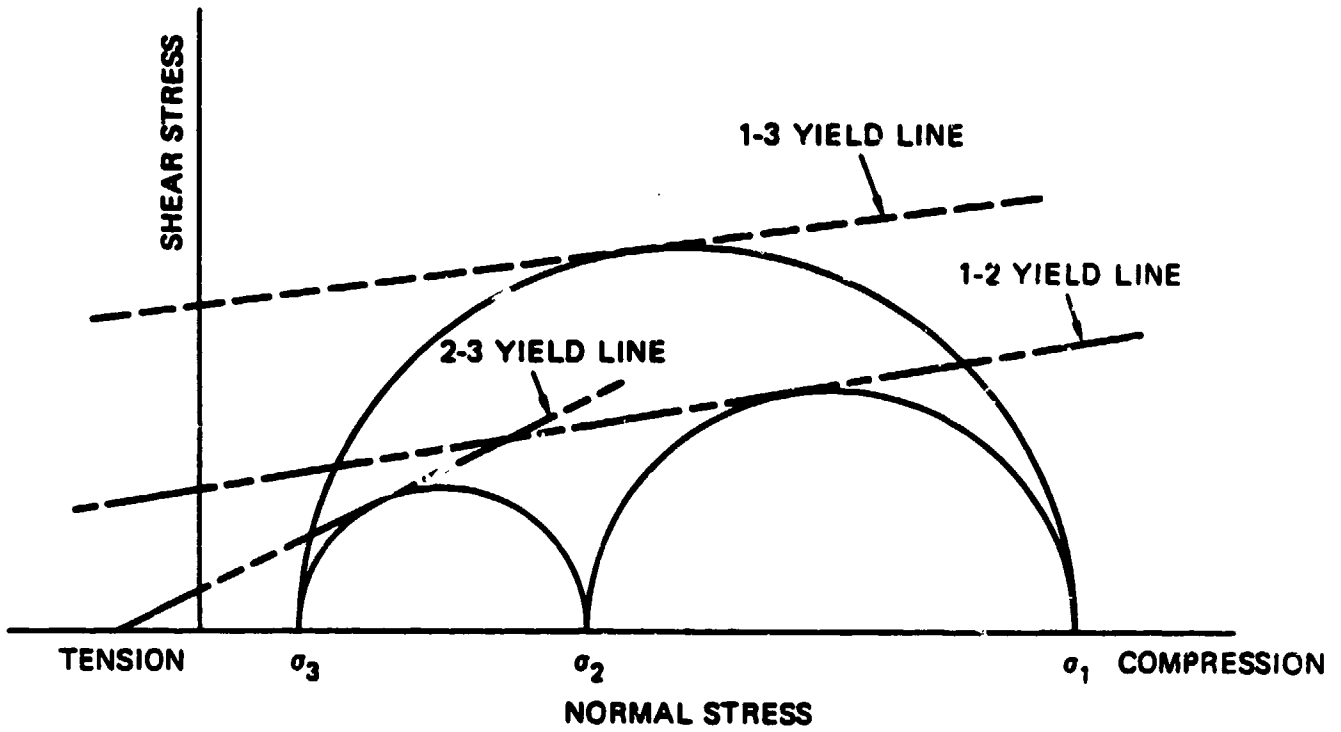
These plastic strain increments are consistent with a normality flow rule applied to deviator stresses only, not to total stresses as in the usual case. This special treatment of normality occurs because of the requirement that the pressure be unaffected by yielding.

The foregoing analysis gives a complete solution for stresses and plastic strains if yielding occurs on only one principal plane and tensile failure is not occurring.

d. Yield Calculation for Multiple Yield Lines

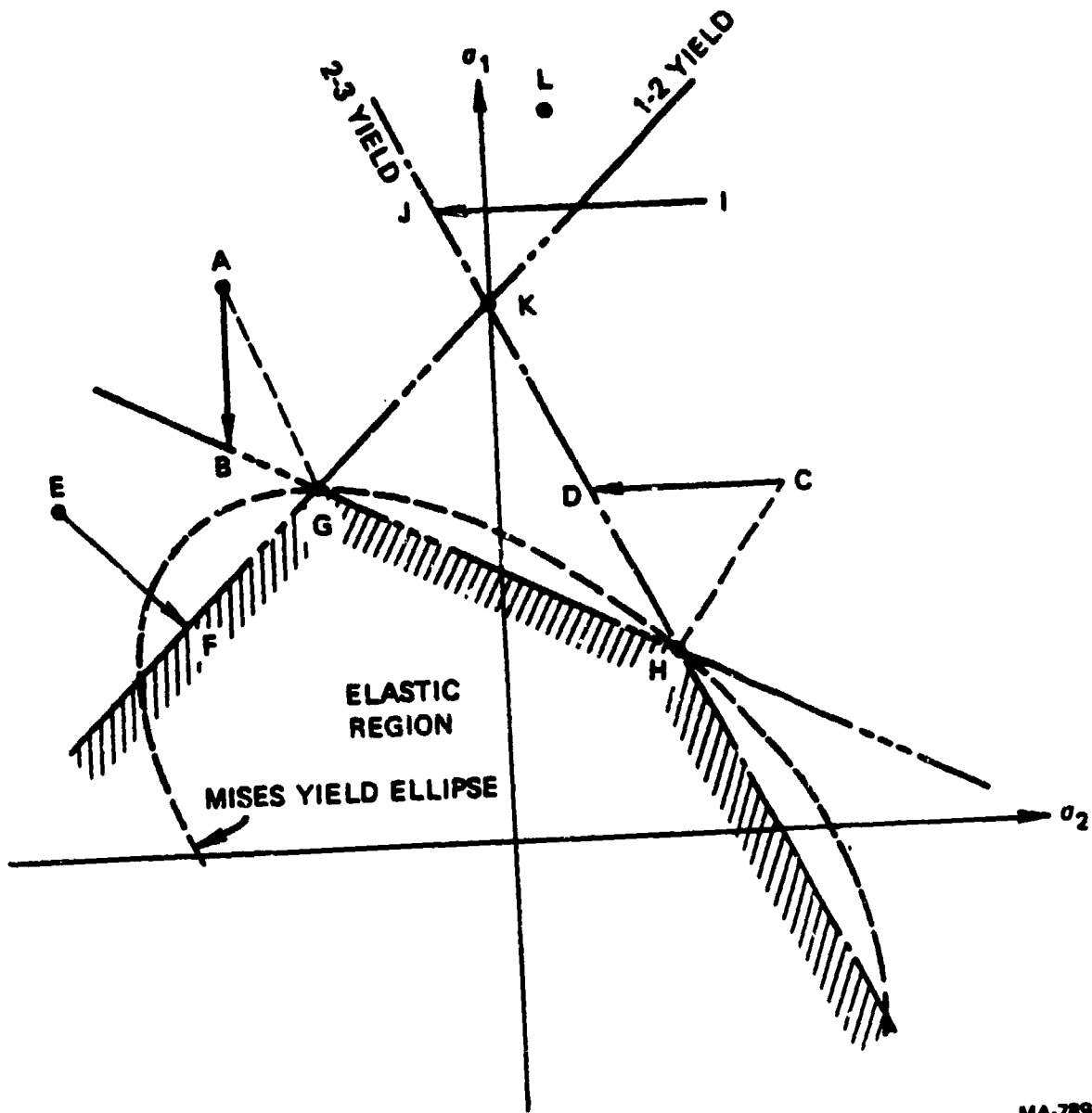
Yielding may occur simultaneously on the three planes associated with the principal stresses in pairs: 1-2, 1-3, 2-3. Such a possibility is illustrated by the Mohr circle and limit lines in Figure A-5. Each of the three circles is tangent to its own limit line. Note that the yield limits are not identical in all three planes as they would be for an isotropic material. Thus we permit the shear strength to reduce on a plane of damage, but to remain high on other planes.

Another sketch for viewing the multiple yield process is shown in Figure A-6. Because the pressure is held constant, yielded and unyielded principal stress states can be depicted completely in this plane for all three principal stresses. This sketch is made for the simple case in which $\tau_{ij} = 0$ for all planes. The Mises yield criterion is also shown for comparison. Three stress states A, C, and E are shown outside the yield limits: they represent σ_1^N , σ_2^N , and σ_3^N values. In accordance with Eq. (A-28) for the stress corrections for yielding, the stress points are moved onto the yield lines at B, D, and F. For example, AB is vertical because σ_2' is held constant during yield to the 1-3 line, but point B is also outside the 1-2 yield line, so B is not a valid solution. Instead, the solution is at G, at the point between the 1-2



MA-7893-6

FIGURE A-5 MOHR DIAGRAM ILLUSTRATING SIMULTANEOUS YIELD ON THREE PLANES



MA-7893-7

FIGURE A-6 DEVIATOR STRESS DIAGRAM ILLUSTRATING THREE YIELD LINES, THE MISES YIELD ELLIPSE, AND YIELD SOLUTIONS FOR SEVERAL STRESS STATES ($\xi = \tau = 0$)

and 1-3 yield lines. Clearly the stress reduction along the line AG can be resolved into components parallel to AB and EF so the stress reduction can be regarded as a combination of yielding on both the 1-2 and 1-3 lines. A similar combined result occurs for yielding at C. The line EF represents yielding on a single line. Yielding at I represents an inconveniently complex case. The single yield computation on the 2-3 line leads to a solution that is inadmissible because it shows yielding on the 1-2 line although I is on the elastic side of that line. For point I, the correct solution is at point H.

When multiple yield lines are involved, the solutions for yielding on a single line (Eq. A-29) are obtained first, and the resulting stresses are used to evaluate the g_{ij} values on the other yield lines. If the single solutions do not represent valid stress states (all $g_{ij} \leq 0$), then a solution is made for stress states at a joint between yield lines. The joint solution is obtained by eliminating σ_3' from the three g_{ij} equations using the definition

$$\sigma_1' + \sigma_2' + \sigma_3' = 0 \quad (\text{A-31})$$

Then the g_{ij} values are set to zero and solved simultaneously in pairs for σ_1' and σ_2' . The results for the 1-2, 1-3 joint are

$$\sigma_1' = \left\{ 2Y_s [(1 - \tau_{13}) \sqrt{N_{\xi 13} N_{\xi 12}} + (1 - \tau_{12}) \sqrt{N_{\xi 12} N_{\xi 13}}] + P(2N_{\xi 12} N_{\xi 13} - N_{\xi 12} - N_{\xi 13}) \right\} / (N_{\xi 12} + N_{\xi 13} + N_{\xi 12} N_{\xi 13}) \quad (\text{A-32})$$

and

$$\sigma_2' = \frac{\sigma_1'}{N_{\xi 12}} - \frac{2(1 - \tau_{12})Y_s}{\sqrt{N_{\xi 12}}} \quad (\text{A-33})$$

In each case the third principal stress is obtained from the definition of pressure

$$\sigma_3 = 3P - \sigma_2 - \sigma_1 \quad (\text{A-34})$$

For yielding at the 1-2, 2-3 point, the solution is

$$\sigma_1' = \left\{ 2Y_s [(1 - \tau_{23}) \sqrt{N_{\xi 23}} N_{\xi 12} + (1 - \tau_{12}) \sqrt{N_{\xi 12}} (1 + N_{\xi 23})] + P(2N_{\xi 12} N_{\xi 23} - N_{\xi 23} - 1) \right\} / (1 + N_{\xi 23} + N_{\xi 12} N_{\xi 23}) \quad (\text{A-35})$$

Again σ_2 and σ_3 are obtained from Eqs. (A-33) and (A-34). For yielding at the 1-3, 2-3 joint, the solution is

$$\sigma_1' = \left\{ 2Y_s [(1 - \tau_{13}) \sqrt{N_{\xi 13}} (1 + N_{\xi 23}) - (1 - \tau_{23}) \sqrt{N_{\xi 23}} N_{\xi 13}] + P(2N_{\xi 13} - N_{\xi 23} - 1) \right\} / (1 + N_{\xi 13} + N_{\xi 23}) \quad (\text{A-36})$$

$$\sigma_2 = -\sigma_1 \left(1 + \frac{1}{N_{\xi 13}}\right) + 2 \frac{(1 - \tau_{13}) Y_s}{N_{\xi 13}} + 3P \quad (\text{A-37})$$

and σ_3 is from Eq. (A-34). The stress solutions in Eqs. (A-32), (-33), (-35)-(-37) are predicated on the assumption that the sloping portion of each yield function is being used. However, the correct solution for the horizontal portion can be obtained by setting $N_{\xi ij} = 1$ and $\tau_{ij} = 0$ in these equations.

Following solution for stresses at a joint between two yield lines, the g_{ij} value for the third yield line is evaluated with the new stresses. This test avoids use of solutions at a joint such as point K in Figure A-6.

For a point such as L in Figure A-6, all three yield lines are exceeded. Therefore, three individual yield calculations are made and tested and then three joint solutions. The joint solutions at G and H

are equally satisfactory; therefore, an average of the stresses at these two points is taken as the solution.

The plastic strains for the joint solution are taken from Eq. (A-30).

a. Tensile Failure

Tensile failure may occur and alter the stresses in a manner different from that caused by the shear processes. Here we consider only a simplified tensile failure, not a complete analysis of the opening of the bands in tension.

As the stress state becomes more tensile, the Mohr circle (as in Figure A-4) moves to the left. The yield calculations will shrink the circle, causing σ_1 and σ_j to approach each other. Finally, when the center of the circle moves to the left of the intercept (B) of the yield line on the normal stress axis, the stress solution from Eq. (A-29) will give $\sigma_j > \sigma_1$. Such a state does not actually meet the yield requirements. Therefore, two adjustments are made:

- The stresses are set equal to the value at the intercept.
- The pressure is permitted to change.

The stresses at the intercept point are

$$\sigma_1 = \sigma_j = - (1 - \tau_{1j}) Y_s \cos \xi_{1j} \quad (\text{A-38})$$

This result is obtained from the geometry shown in Figure A-4. The third principal stress is unchanged.

For the multiple yield line solution, each stress involved in yielding is tested to make certain that it is greater (more compressive) than the intercept values. Each stress is involved in two yield lines and must therefore be compared with two intercept values.

The foregoing tensile process is intended to represent a combination of shear and tensile behavior. If only shear were considered, the sloping Coulomb friction line would be modified to become horizontal at $S = C$ in the tensile range. Then there would be no intercept on the

normal stress axis and no need for a special treatment. However, the tensile failure model outlined above was felt to better represent real material behavior.

f. Implementation in the Shear Band Model

Incorporation of the stress relaxation algorithm into the shear band model requires some coordination of orientations used. The stresses stored for the shear band model are oriented in the fixed, external X, Y, Z space. However, the damage orientations are fixed to the material and therefore may gradually rotate about the Z axis during a normal computation. The stress and damage quantities are brought together on the orientations of the principal stress directions. The principal stresses are at an angle θ_p (positive counterclockwise) from the X direction in the X-Y plane. The material has rotated through an angle ρ (also positive counterclockwise) from the original X-Y orientation. Initially, both the stresses and damage quantities are transformed to the principal stress coordinates through the rotations θ_p and $\theta_p - \rho$, respectively. Then the yield and plastic strain calculations above are undertaken. Plastic strains are then transformed to the material coordinate directions (through $-\theta_p + \rho$), and the stresses are rotated through $-\theta_p$ to the external X-Y system.

APPENDIX B

THRESHOLD INITIATION CRITERIA FOR ADIABATIC SHEAR BANDING

1. Constitutive Instability Theory

A common explanation for the initiation of adiabatic shear bands is that they are plastic instabilities that occur when the thermal softening overwhelms the work hardening, thus causing the effective hardening modulus to become negative. The theory of such instabilities has been recently summarized by Rice³⁷ and Clifton.³⁸ Another recent literature survey for shear banding phenomena was given by Rogers.³⁹ This instability approach, modified by dynamic loading effects, has been applied to our data, and is described below.

If we assume that the shear strength τ of an isotropic material is a function only of the equivalent plastic strain $\bar{\epsilon}^P$ and the temperature T , then

$$\tau = \hat{\tau}(\bar{\epsilon}^P, T)$$

As shown for 4340 steel ($R_c 40$) [B-7] in Figure B-1, this yield condition defines a surface, and any specified load path must lie on the surface. Two extreme paths are the isothermal hardening, and constant strain softening, paths shown in Figure B-1 as solid and dotted lines, respectively. An actual load path will usually lie between these extremes. An important special case is the adiabatic load path shown as the dashed curve in Figure B-1. If the plastic work is converted to heat, and the heat is not allowed to escape, then significant thermal softening can occur. Figure B-2 shows the projection of the estimated adiabatic heating path on the τ - $\bar{\epsilon}^P$ plane for three hardnesses of 4340 steel.⁴⁰ It is seen that the stress on an adiabatic load path begins to drop at strains in excess of about 20%.

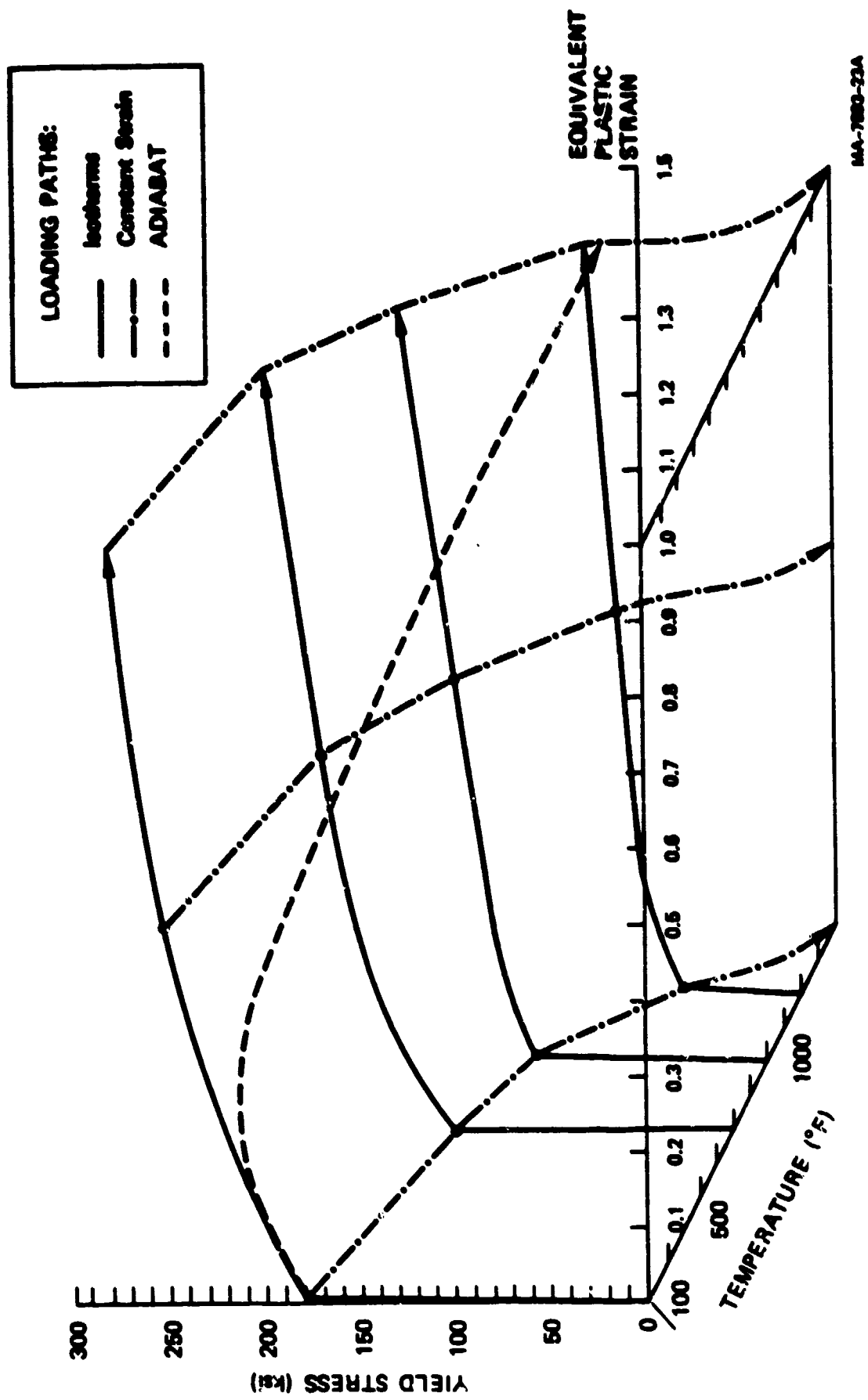
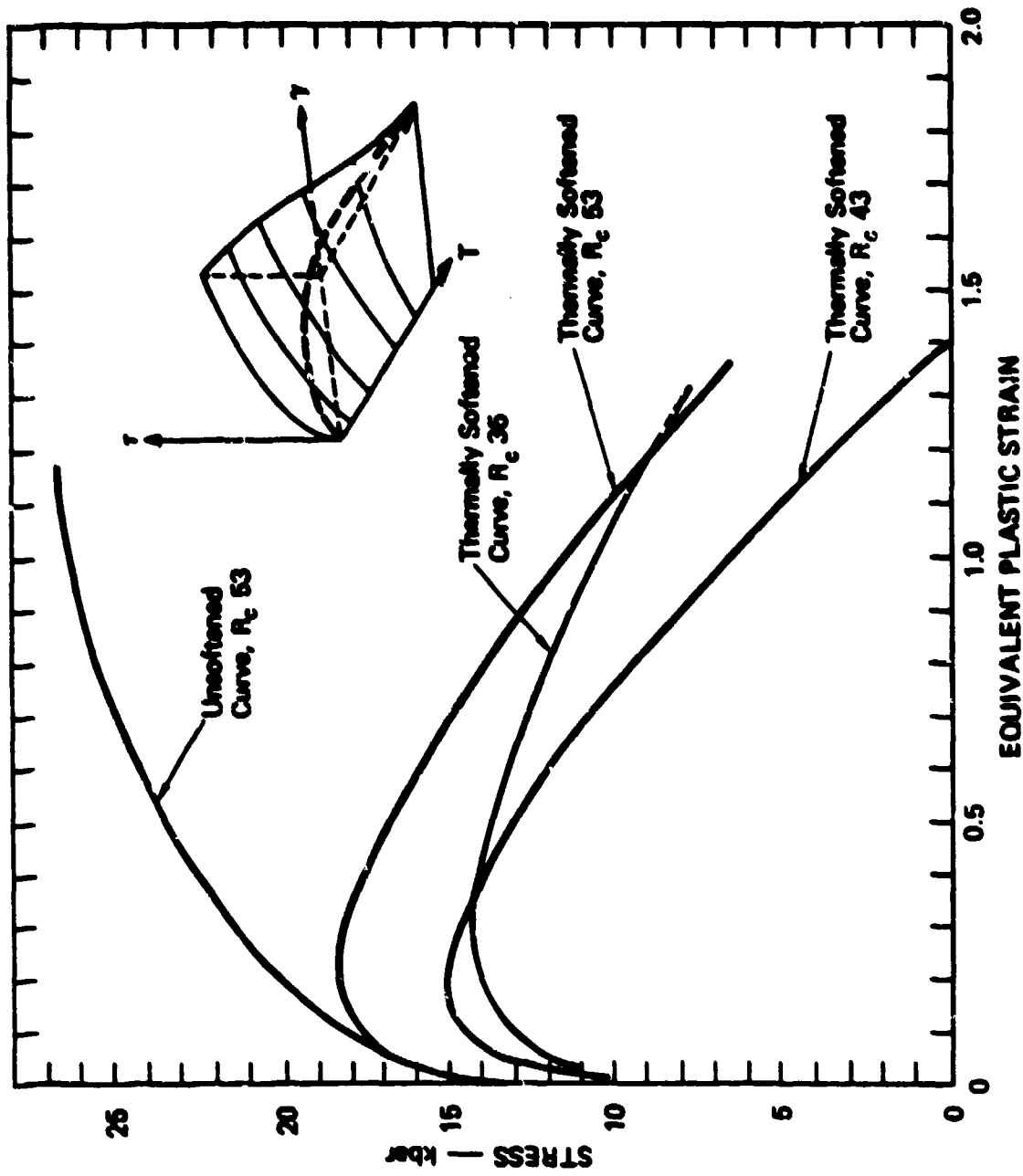


FIGURE B-1 STATIC TEMPERATURE-DEPENDENT YIELD SURFACE FOR 4340 STEEL, R_c 43



MA-7000-198

FIGURE B-2 STATIC ADIABATIC YIELD CURVES FOR 4340 STEEL

The mathematical conditions for constitutive instability are illustrated most simply by considering the one-dimensional case shown in Figure B-3. In this case a pure shear wave propagates in the direction of the Lagrangian coordinate h , carrying displacement u and velocity v normal to h . The equations describing the motion are

$$\epsilon^P = -\frac{1}{2} \frac{\partial u}{\partial h} \quad (B-1)$$

$$v = \frac{\partial u}{\partial t} \quad (B-2)$$

$$2 \frac{\partial \epsilon^P}{\partial t} = -\frac{\partial v}{\partial h} \quad (B-3)$$

$$\frac{\partial v}{\partial t} = -2 c^2 \frac{\partial \epsilon^P}{\partial h} \quad (B-4)$$

where $\rho c^2 = d\tau/d\epsilon^P$ and where we have assumed that the shear stress is a function only of the plastic strain ϵ^P . This will be the case whenever a particular load path is specified because the specification provides an independent relation between ϵ^P and T , and the T - dependence can be eliminated.

Combining (B-1), and (B-2), and (B-4) yields

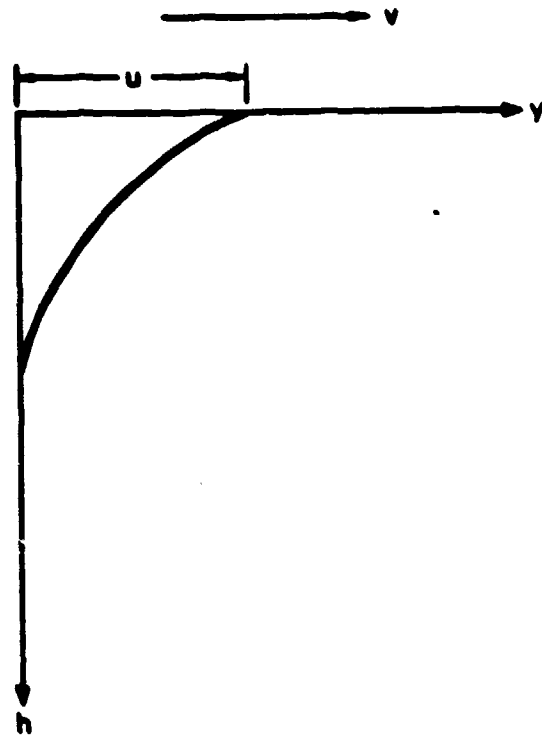
$$\left(\frac{\partial^2 u}{\partial t^2} \right)_h = \frac{c^2}{2} \left(\frac{\partial^2 u}{\partial h^2} \right)_t \quad (B-5)$$

We next linearize this nonlinear equation by considering a perturbation on a static state u_0 . That is,

$$u = u_0 + \delta, \quad c^2 = c^2(\gamma_0)$$

Then (B-5) becomes

$$\frac{\partial^2 \delta}{\partial t^2} = \frac{c^2}{2}(\gamma_0) \frac{\partial^2 \delta}{\partial h^2} \quad (B-6)$$



MA-7883-21A

FIGURE B-3 ONE-DIMENSIONAL SHEAR WAVE LOADING

which has solutions of the form

$$\delta = \text{Re} \exp \left[ik \left(h - \frac{Ct}{\sqrt{2}} \right) \right] \quad , \quad (\text{B-7})$$

where k is the wave number and $i = \sqrt{-1}$.

Thus, if C^2 is real and positive, the periodic disturbance is stable; but if C^2 is real and negative, divergent growth occurs and the smallest wavelengths are the most unstable.

In summary, shear bands will nucleate whenever $C^2 < 0$, where

$$C^2 = \frac{1}{\rho} \left(\frac{\partial \tau}{\partial \epsilon^P} \right)_h = \frac{1}{\rho} \left[\left(\frac{\partial \tau}{\partial \epsilon^P} \right)_T + \left(\frac{\partial \tau}{\partial T} \right) \left(\frac{dT}{d\epsilon^P} \right) \right] \quad (\text{B-8})$$

As shown in Figure B-2, nucleation will occur under adiabatic deformation in 4340 steel at strains of 20-30%, depending on the hardness. As we discussed in Section III-B, this result is in good agreement with the observed initiation strains in the cylinder experiments.

Relation (B-8) thus appears to be a good candidate for the desired threshold initiation criterion under adiabatic loading conditions. The remaining problem is to define the conditions under which the load can be considered to be suitably adiabatic.

Kinematic Localization. One way for adiabatic deformation to occur is for the loading rate to be high compared with both the heat flow rate and the rate at which plastic waves can carry away the strain. Let us first examine the plastic wave effect. For the one-dimensional situation of Figure B-3, the characteristic directions have velocities $\pm C$, and the characteristics carry constant values of $v \pm \int C d\epsilon^P$. When the disturbance travels into initially undisturbed material (a simple wave), then v and ϵ^P are constant along the forward facing characteristics, and

$$\frac{\partial v}{\partial t} + C \frac{\partial v}{\partial h} = 0 \quad (\text{B-9})$$

simple wave

$$\frac{\partial \epsilon^P}{\partial t} + C \frac{\partial \epsilon^P}{\partial h} = 0 \quad (\text{B-10})$$

Combination of (B-9) and (B-10) with (B-3) and (B-4) yields

$$\frac{\partial v}{\partial t} = 2C \frac{\partial \epsilon^P}{\partial t} \quad (\text{B-11})$$

$$\frac{\partial v}{\partial h} = 2C \frac{\partial \epsilon^P}{\partial h} \quad (\text{B-12})$$

$$\frac{\partial v}{\partial t} = -C \frac{\partial v}{\partial h} \quad (\text{B-13})$$

$$\frac{\partial \epsilon^P}{\partial t} = -C \frac{\partial \epsilon^P}{\partial h} \quad (\text{B-14})$$

Equations (B-3), (B-4), and (B-9) through (B-14) show that imposed high accelerations and corresponding velocity gradients cause high strain rates and strain gradients; that is, rapid changes in particle velocity will cause rapid changes in plastic strain. The effect of rapid mechanical loading is most clearly seen from Eq. (B-4), rewritten as

$$\left(-\frac{\partial \epsilon^P}{\partial h} \right) = \frac{1}{2C^2} \frac{\partial v}{\partial t} \quad (\text{B-4}')$$

To produce a given strain gradient, we must have a given value of $\frac{1}{2C^2} \frac{\partial v}{\partial t}$. If the hardening modulus is high, corresponding to a large C^2 , then a correspondingly large acceleration $\partial v/\partial t$ is required to cause this "kinematic localization," or "plastic wave trapping."

If the hardening modulus is low, as when the material approaches the instability point, then only a small acceleration is required to maintain a given $\partial \epsilon^P/\partial h$ or $\dot{\epsilon}^P$.

A necessary condition for wave trapping is that the flow is divergent; that is, lines of constant strain must diverge. The flow is always divergent for a simple wave if the material is such that

$$\frac{d^2 \tau}{d\epsilon^P{}^2} < 0$$

because then large strains travel slower than small strains. For non-simple waves the divergence conditions may not always be met for such materials because the initial particle velocity and strain fields may be convergent.

In a slanted impact experiment, where the target is initially at rest, the simple wave conditions apply for the shear wave, and Eq. (B-12) can be integrated across the shear wave to yield

$$\Delta v \approx 2C\Delta\epsilon^P \quad (B-12')$$

Because $\Delta\epsilon_{cr}^P \approx 0.2$ for 4340 steel, a tangential impact velocity of about $0.4 C$ will be required to kinematically localize the critical strain at the impact surface. Of course, C is a function of ϵ^P and (12') should actually be written as

$$\Delta v = 2 \int_0^{0.2} C(\epsilon^P) d\epsilon^P \quad (B-12'')$$

Nonetheless, it is clear that a high hardening modulus (large C) material will require a higher impact velocity to cause localization, whereas a low hardening modulus material will more easily cause thermal failure at the interface.

Adiabatic Heating. The second dynamic factor that determines if deformation is adiabatic is that the material must be heated significantly faster than it cools. To determine the critical strain rate required to maintain adiabatic heating, we must compare the rate at which heat flows out of a plastically deforming region with the rate of heating caused by the plastic work. To simplify the analysis as much as possible, we use Seaman's definition³³ of a pseudovelocity of heat flow,

$$\frac{dh}{dt} = \frac{\beta k}{h} \quad (B-15)$$

where h is now the width of a hot zone, β is a function of the ratio of temperatures inside and outside the hot zone (Seaman takes $\beta = 10$ as a representative value), and k is now the thermal diffusivity (about $0.15 \text{ cm}^2/\text{s}$ for steel). Note that the heat velocity is slower for larger values of h .

The rate of cooling is thus caused by the heat being distributed over an ever-increasing volume of material. That is,

$$\frac{\dot{Q}}{Q} = -\frac{\dot{h}}{h} = -\frac{\beta k}{h^2} \quad (\text{B-16})$$

cooling

where Q is the specific heat energy. The rate of heat increase is thus the rate of increase caused by the plastic work minus the rate of cooling, or

$$\dot{Q} = \frac{\tau}{\rho} \dot{\epsilon}^P - \frac{\beta k}{h^2} Q \quad (\text{B-17})$$

This equation can be compared to the usual heat flow equation:

$$\dot{Q} = \frac{\tau}{\rho} \dot{\epsilon}^P + k \frac{\partial^2 Q}{\partial h^2} \quad (\text{B-18})$$

Therefore, to allow approximate adiabatic conditions, we require that the first term on the r.h.s. of (B-17) or (B-18) greatly exceed the second in magnitude. Somewhat arbitrarily, we specify that:

$$\dot{\epsilon}^P > \frac{10\beta k Q}{(\tau/\rho)h^2} \quad (\text{B-19})$$

That is, we require that the heating rate be ten times the cooling rate.

Equation (B-16) shows that the relative rate of cooling is higher for smaller widths h of the hot zone, corresponding to a larger negative value of $\partial^2 Q/\partial h^2$ in the heat flow equation (B-18).

To specify the required strain rate, we must therefore specify the value of Q/h^2 that we wish to maintain. For 4340 steel, appreciable softening has occurred at $T/T_m = 0.5$, or for a heat energy of

$$Q \approx 3.5 \times 10^9 \text{ erg/g} .$$

For the contained-fragmenting-cylinder experiments, significant strain gradients occur over distances of about 0.1-0.5 cm. Relation (B-19) then gives

$$\dot{\epsilon}^P > 10^2 \text{ s}^{-1} - 10^4 \text{ sec}^{-1} \quad (\text{B-20})$$

where

$$\begin{aligned} \beta &= 10 \\ k &= 0.15 \text{ cm}^2/\text{sec} \\ Q &= 3.5 \times 10^9 \text{ ergs/g} \\ \tau &= 14 \text{ kbar} \\ \rho &= 7.85 \text{ g/cm}^3 \end{aligned}$$

For oblique impact experiments, where an extremely thin layer near the impact interface is loaded by the shear wave via plastic wave trapping, widths on the order of the grain size of the material may be differentially heated. If the width is assumed to be 100 μm , then relation (B-15) gives

$$\dot{\epsilon}^P > \sim 10^5 \text{ sec}^{-1} \quad (\text{B-20}')$$

Thus, Relation (B-20') can be combined with (B-4') to determine the impact acceleration required to attain adiabatic loading condition in an oblique impact experiment.

2. Development of a Simplified Formula to Calculate the Critical Strain Required for Shear Band Initiation

In numerical computations the code could simply check continuously if inequality (B-8) is satisfied to determine if the threshold condition for adiabatic shear banding has been met. In practice, it is more

enlightening to use a critical strain value that has been determined beforehand, because we are then able to see clearly the role of the material properties of work hardening and thermal softening in determining the material resistance to shear banding. In the following paragraphs we derive simple formulae for estimating this critical strain, and compare the predictions of the formulae to experimental data.

Analysis. We first assume that the yield strength (the effective stress* at yield) for most ductile materials can be expressed as:

$$\tau = H(\bar{\epsilon}^P) F\left(\frac{T}{T_m}\right) \quad (B-21)$$

where $\bar{\epsilon}^P$ is the equivalent plastic strain,[†] H is a strain hardening function, F is a thermal softening function, T is the absolute temperature, and T_m is the absolute melting temperature. For materials that harden primarily by dislocation-dislocation interactions, H can be described by a power law of the form:

$$H(\bar{\epsilon}^P) = \tau_0 \bar{\epsilon}^{pn} \quad (B-22)$$

where n is the strain hardening exponent and τ_0 is a constant.

We assume that, under quasi-adiabatic dynamic loading conditions, all the plastic work is converted into heat. Thus, the thermal softening function F can be expressed as:

$$F\left(\frac{T}{T_m}\right) = F\left(\frac{W}{E_m}\right) \quad (B-23)$$

*The effective stress is defined as $\sqrt{\frac{3}{2} \sigma'_{ij} \sigma'_{ij}}$, where σ'_{ij} is the ij component of deviator stress tensor.

†The equivalent plastic strain is defined as $\int \sqrt{\frac{2}{3} d\epsilon^P_{ij} d\epsilon^P_{ij}}$, where ϵ^P_{ij} is the ij component of the plastic strain increment.

where W is the specific energy of plastic deformation and E_m is the specific internal energy at incipient melt. Experimental data has shown that the thermal softening behavior of many materials can be fitted either by a parabolic expression:

$$F\left(\frac{W}{E_m}\right) = \left(1 - \frac{\alpha W}{E_m}\right)^{1/2} \quad (\text{B-24})$$

or by a linear expression:

$$F\left(\frac{W}{E_m}\right) = \left(1 - \frac{\alpha' W}{E_m}\right) \quad (\text{B-25})$$

where α and α' are constants. The approach is the same whether a parabolic or linear thermal softening function is chosen; hence, only the formula using a parabolic thermal softening function will be developed here. Combining Eqs. (B-22) and (B-24) gives an expression for the yield strength:

$$\tau = \tau_o \bar{\epsilon}^{pn} \left(1 - \frac{\alpha W}{E_m}\right)^{1/2} \quad (\text{B-26})$$

The next step is to determine how the thermal softening function depends on $\bar{\epsilon}^p$ so that τ can be expressed as a function of $\bar{\epsilon}^p$ alone. The increment in the specific energy of plastic deformation, dW , is given by:

$$dW = \frac{\tau}{\rho} d\bar{\epsilon}^p = \frac{\tau_o}{\rho} \bar{\epsilon}^{pn} \left(1 - \frac{\alpha W}{E_m}\right)^{1/2} d\bar{\epsilon}^p \quad (\text{B-27})$$

where ρ is the density of the material. Rewriting Eq. (B-27) gives:

$$\frac{dW}{\left(1 - \frac{\alpha W}{E_m}\right)^{1/2}} = \frac{\tau_o \bar{\epsilon}^{pn}}{\rho} d\bar{\epsilon}^p \quad (\text{B-28})$$

Integration of the left-hand side of Equation (B-28) between the limits of 0 and W , and integration of the right-hand side between the limits of 0 and γ gives:

$$\left(1 - \frac{\alpha W}{E_n}\right)^{1/2} = 1 - \frac{\alpha \tau_o \bar{\epsilon}^p{}^{n+1}}{2\rho E_m (n+1)} \quad (B-29)$$

Combining Eqs. (B-29) and (B-26) yields an expansion for τ in terms of $\bar{\epsilon}^p$ alone:

$$\tau = \tau_o \bar{\epsilon}^p{}^n - \frac{\alpha \tau_o \bar{\epsilon}^{2-p(2n+1)}}{2\rho E_m (n+1)} \quad (B-30)$$

Equation (B-30) describes the effective stress at a given point in the material in terms of the equivalent plastic strain at that point under quasi-adiabatic dynamic loading conditions. Equation (B-30) also describes the macroscopic dynamic stress-strain behavior of the material as long as the deformation remains homogeneous. However, once the macroscopic thermal softening behavior overwhelms the macroscopic strain hardening behavior (that is, when $\frac{d\tau}{d\bar{\epsilon}^p} < 0$), a constitutive instability is triggered and the deformation becomes localized.

In other words, we assume that shear banding initiates when the conditions for constitutive instability are reached. As discussed in Section III-B, the number of points in the material at which shear bands actually do nucleate is governed by a separate nucleation function, and the relative growth of the nucleated shear bands is governed by a separate growth function. In any event, shear banding initiates when:

$$\frac{d\tau}{d\bar{\epsilon}^p} = n\tau_o \bar{\epsilon}^p{}^{n-1} - \frac{\alpha(2n+1)\tau_o \bar{\epsilon}^{2-p}{}^{2n}}{(n+1)2\rho E_m} = 0 \quad (B-31)$$

The critical strain required for the initiation of shear banding under quasi-adiabatic dynamic loading conditions is therefore given by:

$$\bar{\epsilon}_{cr}^p = \left[\frac{2\rho E_m n(n+1)}{\alpha \tau_o (2n+1)} \right]^{\frac{1}{n+1}} \quad (B-32)$$

If a linear thermal softening function, Equation (B-25), is used, $\bar{\epsilon}_{cr}^P$ is given by:

$$\bar{\epsilon}_{cr}^P = \left[\frac{n\rho E}{\alpha \tau_0} \right]^{\frac{1}{n+1}} \quad (B-33)$$

The competing effects of thermal softening coefficient, yield strength, and strain hardening coefficient are evident: increasing n increases $\bar{\epsilon}_{cr}^P$, whereas increasing τ_0 and α decrease $\bar{\epsilon}_{cr}^P$.

Application. We have used Eq. (B-32) to predict the critical strain required for shear band initiation in five different steels. The results are summarized in Table B-1. The specific internal energy at incipient melt was taken to be the enthalpy of the material at the temperature in which the material's strength has gone essentially to zero. This turned out to be about the same for each material. The sources from which the various values of τ_0 , n , and α were extracted for each material are indicated at the bottom of the table. The materials in the table are listed according to their predicted resistance to shear band initiation during ballistic impact by blunt-nosed projectiles, with R_c 40 4340 steel being the least resistant. Note from the last column in the table that Equation (B-32) predicts that R_c 40 4340 steel will initiate shear banding at a relatively low value of equivalent plastic strain (~19%). On the other hand, Equation (B-32) predicts that mild steel will initiate shear banding only at a very high value of equivalent plastic strain (~138%).

The ranking of the relative resistance to shear banding predicted by Equation (B-32) for the materials listed in Table B-1 agrees with experimental observations. Erlich et. al.³¹ observed that R_c 40 4340 steel shear bands substantially at equivalent plastic strains less than 40%. Erlich et. al. also observed that R_c 22 RHA does not shear-band until equivalent plastic strains greater than about 80% have been reached (except along planes of weakness parallel to the rolling direction). Finally, Shockey et. al.⁴¹ observed that low-carbon steel does not shear-band even after extensive plastic deformation under ballistic

Table B-1

**CRITICAL STRAINS FOR SHEAR BAND INITIATION
IN VARIOUS MATERIALS AS CALCULATED FROM EQUATION (B-12)**

Material	τ_0 , dyne/cm ²	n	a	E_m , ergs/g	$\bar{\epsilon}_{cr}^p$
4340, R _c 40	$2.70 \times 10^{10(1)}$	0.15 ⁽¹⁾	3.23 ⁽¹⁾	$6.14 \times 10^9(7)$	0.19
4340, R _c 35	$2.50 \times 10^{10(1)}$	0.15 ⁽¹⁾	2.25 ⁽¹⁾	$6.14 \times 10^9(7)$	0.28
HMA, R _c 22	$1.38 \times 10^{10(2)}$	0.19 ⁽²⁾	2.25 ⁽³⁾	$6.14 \times 10^9(7)$	0.56
Hadfield steel	$2.28 \times 10^{10(4)}$	0.59 ⁽⁴⁾	1.59 ⁽⁴⁾	$6.14 \times 10^9(7)$	1.09
Low carbon steel	$1.08 \times 10^{10(5)}$	0.28 ⁽⁵⁾	1.70 ⁽⁶⁾	$6.14 \times 10^9(7)$	1.15

Note: The numbers in parentheses refer to the following references only:

1. The Aerospace Structural Metals Handbook, AFRL-TR-68-115, Vol. 1. Mechanical Properties Data Center, Traverse City, MI (1972).
2. R. D. Caligiuri, R. Burbach, L. Seaman, and D. C. Erlich, "Computational Model for Armor Penetration," Progress Report No. 8 for Contract DAAK11-78-C-0115, submitted to the Ballistics Research Laboratory, Aberdeen, MD, and the Army Materials and Mechanics Research Center, Watertown, MA (July 1979).
3. Best estimate from available data.
4. Metals Handbook, 7th Edition (American Society for Metals, Cleveland, Ohio, 1948), pp. 526-534.
5. R. M. Brick and A. Phillips, Structure and Properties of Alloys (McGraw-Hill Book Co., Inc., New York, 1949), p. 16.
6. Metals for Supersonic Aircraft and Missiles, Proc. of Conf. on Heat Tolerant Metals for Aerodynamic Applications, Jan. 28-29, 1959, University of New Mexico, Albuquerque, New Mexico (American Society for Metals, Cleveland, Ohio 1958), p. 25.
7. Metals Handbook, 8th Edition, Vol. 1 (American Society for Metals, Metals Park, Ohio 1961), p. 1208.

impact conditions. It thus appears that Equation (B-32) can be used to correctly rank material as to their relative resistance to shear band formation and to roughly estimate the critical strain required for shear band initiation. It should be noted that these experimental "critical" strains represent only the strain at which large shear bands were first observed, and not the critical strain at which shear banding really initiated. If the actual critical strains could be pinpointed more closely experimentally, the critical strains predicted by Equation (B-32) might better match experimental data.

Conclusions. A formula, Equation (B-32), has been developed for quickly ranking materials as to their resistance to shear banding during ballistic impact and for estimating the critical strain required for shear band initiation. Development of this formula required two key assumptions. First, during quasi-adiabatic dynamic loading, all the energy of plastic deformation is converted into heat. Second, shear banding initiates in a material when its thermal softening response to quasi-adiabatic dynamic loading overwhelms its work-hardening response to the same loading conditions. This formula was used to rank five different steels as to their relative resistance to shear banding under ballistic impact by a blunt-nosed projectile. This relative ranking agreed with experimental observations. The estimated values of the critical strain required for initiating shear banding in each material also roughly agreed with available experimental data. It thus appears that this formula has promise for armor design.

DISTRIBUTION LIST

<u>No. of Copies</u>	<u>Organization</u>	<u>No. of Copies</u>	<u>Organization</u>
12	Administrator Defense Technical Info Center ATTN: DTIC-DDA Cameron Station Alexandria, VA 22304-6145	1	Director US Army Air Mobility Research and Development Laboratory Ames Research Center Moffett Field, CA 94035
1	HQDA (DAMA-ART-M) Washington, DC 20310	1	Commander US Army Communications - Electronics Command ATTN: AMSEL-ED Fort Monmouth, NJ 07703
1	Commander US Army Materiel Command ATTN: AMCDRA-ST 5001 Eisenhower Avenue Alexandria, VA 22333-0001	1	Commander ERADCOM Technical Library ATTN: DELSD-L (Reports Section) Fort Monmouth, NJ 07703-5301
1	Commander Armament R&D Center US Army AMCCOM ATTN: SMCAR-TSS Dover, NJ 07801	1	Commander US Army Missile Command Research, Development and Engineering Center ATTN: AMSMI-RD Redstone Arsenal, AL 35898
1	Commander Armament R&D Center US Army AMCCOM ATTN: SMCAR-TDC Dover, NJ 07801	1	Director US Army Missile & Space Intelligence Center ATTN: AIAMS-YDL Redstone Arsenal, AL 35898-5500
1	Commander US Army Material Technology Laboratory ATTN: John Mescall Watertown, MA 02172	1	Commander US Army Tank-Automotive Command ATTN: AMSTA-TSL Warren, MI 48397-5000
1	Director Benet Weapons Laboratory Armament R&D Center US Army AMCCOM ATTN: SMCAR-LCB-TL Watervliet, NY 12189	3	Director US Army TRADOC Systems Analysis Activity ATTN: ATAA-SL White Sands Missile Range, NM 8002
1	Commander US Army Armament, Munitions and Chemical Command ATTN: SMCAR-ESP-L Rock Island, IL 61299	1	Commandant US Army Infantry School ATTN: ATSH-CD-CSO-OR Fort Benning, GA 31905
1	Commander US Army Aviation Research and Development Command ATTN: AMSAV-E 4300 Goodfellow Blvd St. Louis, MO 63120		

DISTRIBUTION LIST

<u>No. of Copies</u>	<u>Organization</u>	<u>No. of Copies</u>	<u>Organization</u>
1	Commander US Army Development & and Employment Agency ATTN: MODE-TED-SAB Fort Lewis, WA 98433	10	Central Intelligence Agency Office of Central Reference Dissemination Branch Room GE-47 HQS Washington, DC 20502
1	AFWL/SUL Kirtland AFB, FL 87117		<u>Aberdeen Proving Ground</u>
1	AFATL/DLODL Eglin AFB, FL 32542-5000		Dir, USAMSAA ATTN: AMXSY-D AMXSY-MP (H. Cohen)
1	AFATL (Joe Foster) Eglin AFB, FL 32452-5000		Cdr, USATECOM ATTN: AMSTE-TO-F
2	US Army Research Office ATTN: George Mayer Robert Singleton P. O. Box 12211 Research Triangle Park, NC 27709		Cdr, CRDC, AMCCOM ATTN: SMCCR-RSP-A SMCCR-MU SMCCR-SPS-IL
2	Naval Surface Weapons Center ATTN: William H. Holt Willis Mock, Jr. Dahlgren, VA 22448		
1	Naval Research Laboratory ATTN: Rick Mako Washington, DC 20375		

USER EVALUATION SHEET/CHANGE OF ADDRESS

This Laboratory undertakes a continuing effort to improve the quality of the reports it publishes. Your comments/answers to the items/questions below will aid us in our efforts.

1. BRL Report Number _____ Date of Report _____

2. Date Report Received _____

3. Does this report satisfy a need? (Comment on purpose, related project, or other area of interest for which the report will be used.) _____

4. How specifically, is the report being used? (Information source, design data, procedure, source of ideas, etc.) _____

5. Has the information in this report led to any quantitative savings as far as man-hours or dollars saved, operating costs avoided or efficiencies achieved, etc? If so, please elaborate. _____

6. General Comments. What do you think should be changed to improve future reports? (Indicate changes to organization, technical content, format, etc.) _____

CURRENT ADDRESS

Name

Organization

Address

City, State, Zip

7. If indicating a Change of Address or Address Correction, please provide the New or Correct Address in Block 6 above and the Old or Incorrect address below.

OLD ADDRESS

Name

Organization

Address

City, State, Zip

(Remove this sheet, fold as indicated, staple or tape closed, and mail.)